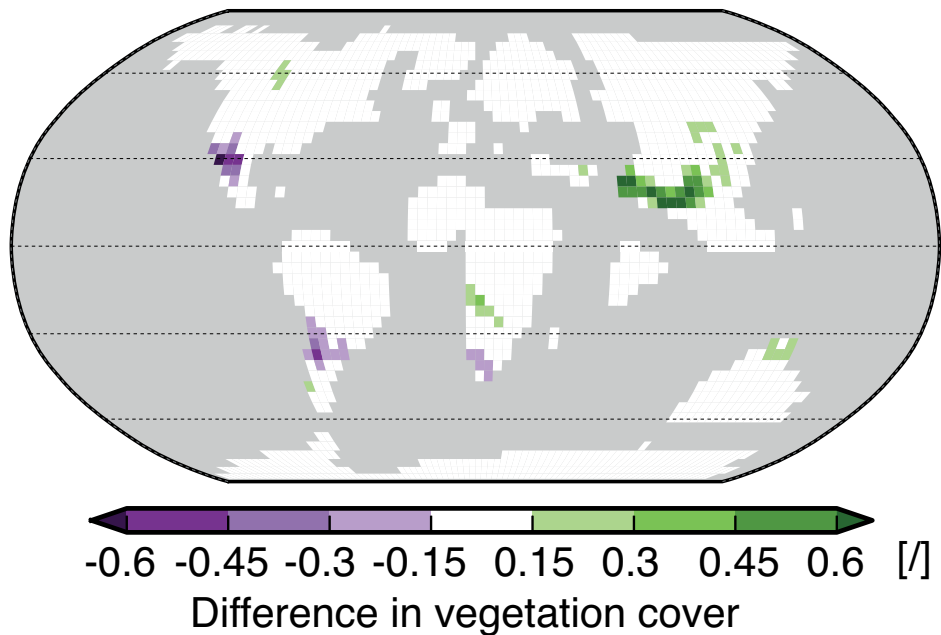




Vegetation-Atmosphere Interactions in the Early Eocene Climate



Ulrike Port

Hamburg 2014

Hinweis

Die Berichte zur Erdsystemforschung werden vom Max-Planck-Institut für Meteorologie in Hamburg in unregelmäßiger Abfolge herausgegeben.

Sie enthalten wissenschaftliche und technische Beiträge, inklusive Dissertationen.

Die Beiträge geben nicht notwendigerweise die Auffassung des Instituts wieder.

Die "Berichte zur Erdsystemforschung" führen die vorherigen Reihen "Reports" und "Examensarbeiten" weiter.

Anschrift / Address

Max-Planck-Institut für Meteorologie
Bundesstrasse 53
20146 Hamburg
Deutschland

Tel./Phone: +49 (0)40 4 11 73 - 0
Fax: +49 (0)40 4 11 73 - 298

name.surname@mpimet.mpg.de
www.mpimet.mpg.de

Notice

The Reports on Earth System Science are published by the Max Planck Institute for Meteorology in Hamburg. They appear in irregular intervals.

They contain scientific and technical contributions, including Ph. D. theses.

The Reports do not necessarily reflect the opinion of the Institute.

The "Reports on Earth System Science" continue the former "Reports" and "Examensarbeiten" of the Max Planck Institute.

Layout

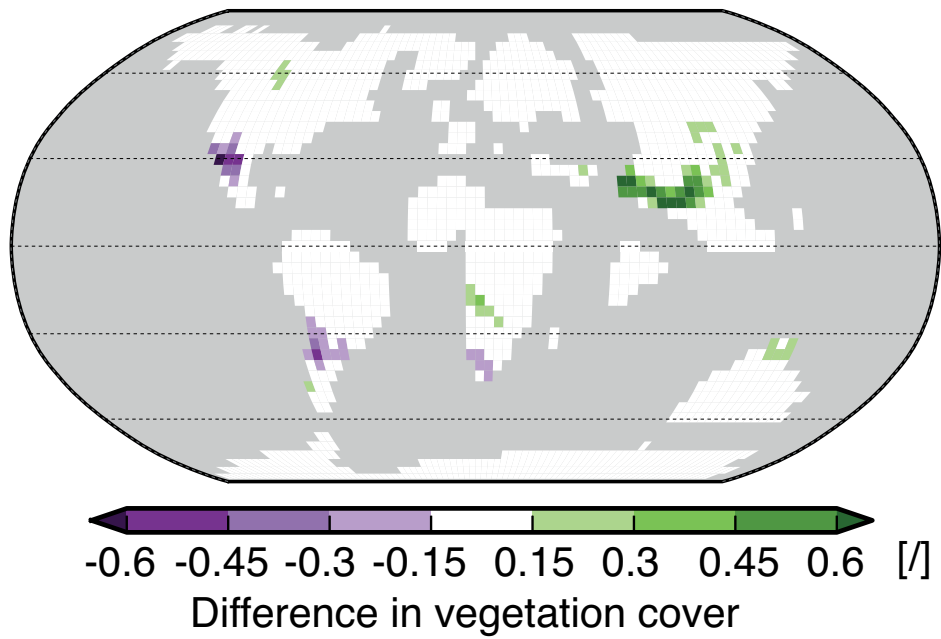
Bettina Diallo and Norbert P. Noreiks
Communication

Copyright

Photos below: ©MPI-M
Photos on the back from left to right:
Christian Klepp, Jochem Marotzke,
Christian Klepp, Clotilde Dubois,
Christian Klepp, Katsumasa Tanaka



Vegetation-Atmosphere Interactions in the Early Eocene Climate



Ulrike Port

Hamburg 2014

Ulrike Port

Max-Planck-Institut für Meteorologie
Bundesstrasse 53
20146 Hamburg

Als Dissertation angenommen
vom Fachbereich Geowissenschaften der Universität Hamburg

auf Grund der Gutachten von
Prof. Dr. Martin Claussen
und
Dr. Victor Brovkin

Hamburg, den 26.11. 2014
Professor Dr. Christian Betzler
Leiter des Departments Geowissenschaften

Abstract

During the early Eocene (about 54 to 52 Million years ago), climate was much warmer than today. This thesis reveals that vegetation affected the early Eocene climate differently than the pre-industrial climate. Using the Max Planck Institute for Meteorology Earth System Model, the same two simulations are performed for the early Eocene climate and the pre-industrial climate. All continents are either covered with a dense forest or with bare soil. The assumed soil albedo is similar to vegetation albedo.

The comparison of the forest world with the desert world provides the radiative forcing by forest and the strength of the resulting climate feedbacks. In both climates, forest induces a negative radiative forcing of a similar strength by increasing the cloud cover. The resulting cooling, however, differs for both climates because climate feedbacks differ. In the pre-industrial climate, the lapse-rate/water-vapour feedback intensifies the cooling by forest on a global scale. The ice-albedo feedback amplifies the cooling in the high latitudes. In the early Eocene climate, the lapse-rate/water-vapour feedback is stronger than in the pre-industrial climate and the ice-albedo feedback is weak. Hence, forest cools the global early Eocene climate stronger but polar amplification less pronounced.

The same study was performed with soils that have a much higher albedo than vegetation. In this case, the radiative forcing by forest is positive because forest reduces surface albedo. Like for the dark soil case, the radiative forcing is of similar strength in both climates. The resulting warming, however, differs in both climates because climate feedbacks are specific in each climate.

Starting from the forest world and from the desert world, the simulations continue and the vegetation cover establishes together with climate. For the two initial vegetation covers, two different vegetation-atmosphere states evolve. In the pre-industrial climate, the positive feedback between vegetation and precipitation leads to a smaller Sahara desert when the simulation starts from the forest world instead of the desert world. In the early Eocene climate, the same feedback causes a smaller desert in Central Asia when the simulation starts from a forest world. Moreover, vegetation in Central Asia enhances the Asian Monsoon in the early Eocene climate. Hence, two global circulation patterns establish with a small Asian desert and with a large Asian desert. With two global circulation patterns, two globally different states of the early Eocene climate coexist.

The results imply that vegetation affects the early Eocene climate differently than the pre-industrial climate because the atmospheric state, the vegetation cover, and the distribution of continents are specific for both climates. Besides for the early Eocene climate, this finding is likely valid for other past and future climates. Hence, the influence of vegetation on climate and the stability of the vegetation-atmosphere system are presumably unique in each geological period.

Zusammenfassung

Während des frühen Eozäns (vor ca. 54 bis 52 Millionen Jahren) war das Klima bedeutend wärmer als heute. Diese Arbeit zeigt, dass Vegetation das Klima des frühen Eozäns anders beeinflusst als das vorindustrielle Klima. Mit dem Erdsystemmodell des Max-Planck-Institutes für Meteorologie werden je zwei Simulationen für das Klima des frühen Eozäns und für das vorindustrielle Klima durchgeführt. Entweder dichter Wald oder nackter Boden bedeckt alle Kontinente. Die angenommene Bodenalbedo ist ähnlich der Vegetationsalbedo.

Der Vergleich der Waldwelt mit der Wüstenwelt liefert den Strahlungsantrieb von Wald und die resultierenden Klima-Rückkopplungen. Wald verursacht einen negativen Strahlungsantrieb durch eine Zunahme der Wolkenbedeckung. Im Klima des frühen Eozäns ist der Strahlungsantrieb ähnlich stark wie im vorindustriellen Klima. Die resultierende Abkühlung jedoch unterscheidet sich in beiden Klimazuständen, weil die Klima-Rückkopplungen verschieden stark ausgeprägt sind. Im vorindustriellen Klima verstärkt die Wasserdampf-Rückkopplung die Abkühlung durch Wald auf einer globalen Skala. Die Eis-Albedo-Rückkopplung verstärkt die Abkühlung in den hohen Breiten. Im Klima des frühen Eozäns ist die Wasserdampf-Rückkopplung ausgeprägter und die Eis-Albedo-Rückkopplung schwächer als im vorindustriellen Klima. Daher kühlt Wald das globale Klima stärker im frühen Eozän. Die polare Verstärkung jedoch ist schwach. Die gleiche Studie wurde mit einem Boden durchgeführt, dessen Albedo höher ist als die Albedo von Vegetation. In diesem Fall ist der Strahlungsantrieb von Wald positiv, weil Wald die Oberflächenalbedo reduziert. Wie im Fall des dunklen Bodens ist der Strahlungsantrieb in beiden Klimazuständen ähnlich stark. Jedoch unterscheidet sich die resultierende Erwärmung in beiden Klimazuständen, weil Klima-Rückkopplungen spezifisch sind für das jeweilige Klima.

Ausgehend von der Wald- und der Wüstenwelt laufen die Simulationen weiter und die Vegetationsbedeckung entwickelt sich entsprechend des jeweiligen Klimas. In Abhängigkeit von der Vegetationsbedeckung am Anfang der Simulation entwickeln sich unterschiedliche Vegetations-Atmosphären-Zustände. Im vorindustriellen Klima führt die positive Rückkopplung zwischen Vegetation und Niederschlag zu einer kleineren Wüste Sahara, wenn die Simulation von einer Waldwelt ausgeht anstatt von einer Wüstenwelt. Im Klima des frühen Eozäns verursacht dieselbe Rückkopplung eine kleinere Wüste in Zentralasien, wenn die Simulation von einer Waldwelt startet. Außerdem verstärkt die Vegetation in Zentralasien den asiatischen Monsun im Klima des frühen Eozäns. Daher entwickeln sich zwei globale Zirkulationsmuster mit einer kleinen asiatischen Wüste und einer großen asiatischen Wüste. Die zwei globalen Zirkulationsmuster führen zu zwei global unterschiedlichen Klimazuständen im frühen Eozän.

Diese Ergebnisse deuten darauf hin, dass Vegetation das Klima des frühen Eozäns anders beeinflusst als das vorindustrielle Klima. Die Gründe dafür sind das spezifische Klima des frühen Eozäns, die Vegetationsbedeckung und die Verteilung der Kontinente. Wahrscheinlich gilt dieses Ergebnis auch für andere Klimazustände der Vergangenheit und der Zukunft. Daher ist der Einfluss von Vegetation auf das Klima und die Stabilität des Vegetations-Atmosphären-Systems vermutlich einzigartig in jeder geologischen Epoche.

Contents

Abstract	i
Zusammenfassung	iii
1 Introduction	1
1.1 Early Eocene: warm climate, ice-free poles, and green continents . . .	2
1.2 Key questions	4
2 Modelling the Early Eocene Climate	9
2.1 Introduction	9
2.2 MPI-ESM	10
2.3 Model set-up for the early Eocene	12
2.4 Results: The early Eocene climate	14
2.4.1 Comparison to temperature reconstructions	14
2.4.2 Comparison to the pre-industrial climate	16
2.5 Conclusion	19
3 Radiative Forcing by Forest and Subsequent Feedbacks	21
3.1 Introduction	21
3.2 Model and experiments	22
3.3 Methods	23
3.3.1 Radiative forcing and climate feedbacks	23
3.3.2 Decomposition of the radiation balance	25
3.4 Results	27
3.4.1 Afforestation of a bright desert world	28
3.4.2 Afforestation of a dark desert world	32
3.5 Conclusion	34
4 The Stability of the Vegetation-Atmosphere System in the Early Eocene Climate	37
4.1 Introduction	37
4.1.1 Positive climate-vegetation feedbacks in present-day climate . .	39
4.2 Experiment	41
4.3 Results and Discussion	42
4.3.1 Dark soil: hydrological feedbacks cause multiple vegetation-atmosphere states	43
4.3.2 Bright soil: albedo feedbacks stabilise the vegetation-atmosphere system	51
4.4 Summary and Conclusion	60

5	Simulating Early Eocene Plant Species	61
5.1	Introduction	61
5.2	Method	62
5.3	Results	65
5.4	Ideas for improvement	67
5.5	Conclusion	69
6	Summary and Conclusion	71
	Acknowledgements	vii
	Acronyms	ix
	List of Figures	xv
	List of Tables	xviii
	References	xxv

Chapter 1

Introduction

On geological time scales, warm climates dominated the last 570 Million years (Frakes 1979). During the major time of this period, climate was warmer than today and permanent ice sheets and sea ice were absent. Warm climates are fascinating because they are characterised by different states of the atmosphere, the ocean, and the terrestrial biosphere than today (Barron 1987; Sloan et al. 1995; Wolfe 1985). In the context of present warming, warm climates of the past attract further attention (Jansen et al. 2007). The prevalence of warm climates in the past, the difference to the present climate, and the future climate change motivate research on warm climates. The research aims to understand the nature, the causes, and the processes of warm climates. In this thesis, I use a climate model to study the role of vegetation in warm climates. My test bed is the early Eocene climate—one of the warmest climates in the last 65 Million years.

For present-day climate, the impact of vegetation on climate and the synergy effect with other components of the climate system are fairly well understood. I assume, however, that vegetation affects a warm climate differently than the present-day climate. The most illustrative example is the influence of today's forest with temperature the high latitudes. Boreal forest masks the snow cover with its branches, twigs, and stems (Lorantý et al. 2014) and, hence, reduces the surface albedo. By lowering the surface albedo, boreal forest tends to warm the high latitudes (Bonan 1992, 2008; Betts and Ball 1997). The warming includes the Arctic Ocean and triggers the amplifying sea-ice albedo feedback (Brovkin et al. 1999, 2009; Claussen et al. 2001; Fraedrich et al. 2005). Considering a warm climate, the snow cover is much smaller than in present-day climate. Likely, the snow masking effect of boreal forest is weak. This example, motivates me to investigate the influence of vegetation on the early Eocene climate. In order to identify differences to present-day climate, I compare the impact of vegetation on the early Eocene climate with the impact of vegetation on the pre-industrial climate (Chapter 3).

The interaction of vegetation and the atmosphere is suggested to lead to non-linearities and multiple stable states in the vegetation-atmosphere system. For instance, vegetation is suggested to enhance precipitation in the Sahel. In turn, precipitation maintains the plant growth. Based on this interdependence of vegetation and precipitation two stable states are suggested to exist in the Sahel (Claussen 1998; Brovkin et al. 1998; Wang and Eltahir 2000; Zeng and Neelin 2000; Zeng et al. 2004): An arid state with sparse vegetation and weak precipitation as well as a humid state with abundant vegetation and moderate precipitation. In a warm climate, the vegetation cover and the

atmospheric state differ from today. Hence, climate and vegetation likely interact differently. I evaluate the interaction of vegetation with the early Eocene climate. Further, I investigate whether the vegetation-atmosphere system allows for multiple stable states as found in present-day climate (Chapter 4).

Beside shifts in the vegetation cover due to varying climates, the plant species altered in the course of evolution. The appearance and the needs of plants constantly adapted to changing environmental conditions such as climatic changes, propagating diseases, or transitions in fauna's diets (Willis and McElwain (2002)). During warm periods, plants benefited from high atmospheric carbon dioxide (CO_2) concentrations, high precipitation rates, and favourable climate conditions in polar regions. Hence, different plant species appeared in warm climates than in present-day climate. Earth System Models (ESMs) are feasible to simulate the vegetation cover according to the simulated climate. Most models consider present-day plant taxa and do not account for the evolution of plants. Considering present-day plant taxa in palaeo-studies likely induces uncertainties in the simulated vegetation cover and climate. I evaluate the early Eocene vegetation cover simulated based on present-day plant taxa (Chapter 5). By comparing the simulated vegetation to vegetation reconstructions, I assess the discrepancy in the simulated early Eocene vegetation cover that emerges from considering present-day plant taxa. This study is the basis for future studies to implement plant taxa of the early Eocene in earth system models.

The following section introduces the early Eocene and highlights in which way the climate, the vegetation cover, and the plant species differed from today. After the basic introduction of the early Eocene, I formulate three key questions that I aim to answer in this thesis.

1.1 Early Eocene: warm climate, ice-free poles, and green continents

The Eocene epoch started with the Paleocene-Eocene Thermal Maximum (PETM)—an extreme warming event where deep-sea temperature rose by 5°C to 6°C in less than 10.000 years and recovered within 200.000 years (Zachos et al. 2001, Figure 1.1). Following the PETM, climate warmed continuously until the temperature peaked in the Early Eocene Climatic Optimum (EECO). Within this thesis, I will consider the period between the end of the PETM and the EECO (Figure 1.1) and refer to it as the early Eocene.

During the early Eocene, the atmospheric CO_2 concentration was higher than today (Hönisch et al. 2012) and the continents were distributed differently (Chapter 2). The specific boundary conditions of the early Eocene led to a significantly warmer climate than today (Zachos et al. 2001). In the tropics, the annual mean temperature was 5°C to 6°C higher than today (Pearson et al. 2007). Fossils of alligators (Markwick 1994) and tortoises (Hutchison 1982) imply temperature above freezing during the whole year in the high north on Ellesmere Island (76°N). Today, the large extent of glaciers illustrates that sub-freezing temperatures prevail on Ellesmere Island. In the southern

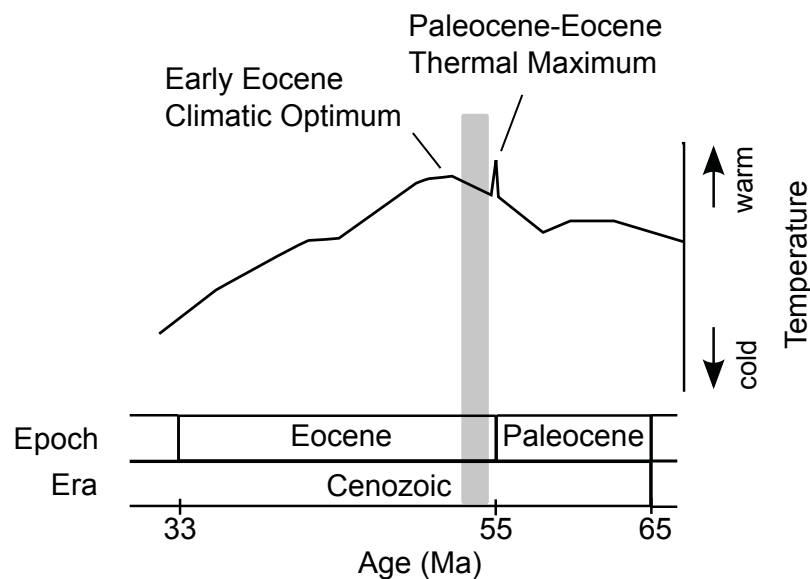


Figure 1.1: Qualitative temperature evolution during the Eocene based on deep-sea temperature estimates adapted from Zachos et al. (2001). The x-axis shows the age since today in Million years (Ma). In this thesis, I consider the early Eocene (gray bar) which is the time between the end of the Paleocene-Eocene Thermal Maximum and the Early Eocene Climatic Optimum.

high latitudes, Ivany et al. (2008) estimate an annual mean temperature of 10°C on Seymour Island (65°S) which is about 19°C higher than the today's temperature at this latitude. In this warm climate, permanent sea ice and ice sheets were absent (Zachos et al. 1992; Ivany et al. 2006).

The warm climate led to a specific vegetation distribution during the early Eocene. Instead of today's ice sheets and tundra, dense vegetation covered the high latitudes (Ivany et al. 2008; Hutchison 1982). Tropical forests grew between 35° south and 35° north today, but extended between 60° south and 60° north during the early Eocene (Utescher and Mosbrugger 2007). Deserts occurred rarely (Willis and McElwain 2002). Only in Central Asia, widely-spread arid conditions have been reconstructed (Zhang et al. 2012; Wang et al. 2013; Quan et al. 2012).

The plant species were adapted to the early Eocene climate and differed from today's plant species. Despite polar night, trees grew in the high latitudes. These trees had larger leaves than in the mid latitudes to cope with polar night (Wolfe 1985). The darkness-tolerant trees have no modern analogue because extremely low temperature precludes tree growth in present-day high latitudes. In the mid to high latitudes, the warm and humid climate led to paratropical rainforest which was a mixture of temperate and tropical forest (Wolfe 1985). Today, paratropical rainforest occurs rarely. Grasslands, which are common in present-day climate, did not exist during the early Eocene because first grass types evolved just in this time (Janis 1993).

1.2 Key questions

The overarching question of this thesis is how vegetation shaped the early Eocene climate. In this context, I focus on three aspects: the influence of vegetation on the early Eocene climate, the stability of the vegetation-atmosphere system, and the early Eocene plant species and how they affected the climate. In the following, I formulate the arising key questions.

The impact of vegetation on climate

In present-day climate, forest tends to warm the high latitudes and tends to cool the tropics by its biogeophysical effect¹. In the high latitudes, boreal forest masks the bright snow cover (Lorantý et al. 2014). The resultant surface albedo reduction leads to a warming (Bonan 1992, 2008; Betts and Ball 1997) and triggers the sea ice-albedo feedback which amplifies the warming in the northern high latitudes (Brovkin et al. 1999, 2009; Claussen et al. 2001; Fraedrich et al. 2005). In the tropics, forest tends to cool climate by transpiring water. Further, the leaves intercept precipitation and the intercepted water enhances evaporation. Through transpiration and interception, tropical forest enhances the latent heat flux and lowers the sensible heat flux. The shift in the heat fluxes results in a cooling (Claussen et al. 2001; Bathiany et al. 2010). The increase in transpiration and evaporation by forest also enhances the cloud cover (Bala et al. 2007). With more clouds, less solar radiation reaches the surface leading to further cooling. On a global scale, the cooling by tropical forests is suggested to outweigh the warming by boreal forests. In simulations by Fraedrich and Kleidon (1999), forests on all continents cause a colder global climate than deserts.

In the past, the impact of vegetation on climate might have been different than today as the study by Otto-Bliesner and Upchurch (1997) indicates. They simulate late Cretaceous climate (~ 66 Ma) which was significantly warmer than today's climate (Miller et al. 2003; Bowman et al. 2013). When they assume a best-guess vegetation cover, the global mean late Cretaceous climate is warmer than with barren continents (Otto-Bliesner and Upchurch 1997). Other than suggested for present-day climate, tropical forest warms in the late Cretaceous climate by reducing the surface albedo. The evaporative effect by tropical forest is weak in the late Cretaceous climate. Like in present-day climate, the snow masking effect in combination with the sea-ice albedo feedback causes a pronounced warming at high latitudes.

The reasons for the difference in the global impact of vegetation on the present-day climate and on the late Cretaceous climate can be twofold. On the one hand, Otto-Bliesner and Upchurch (1997) use a different model than Fraedrich and Kleidon (1999). Also the experimental set-ups differ. For instance, both studies assume different values for the soil albedo leading to a different representation of the albedo effect of vegetation. On the other hand, the different climate states can be the reason for the specific impact

¹The biogeophysical effect refers to changes in the fluxes of energy, momentum, and water between the surface and the atmosphere due to vegetation. Beside the biogeophysical effect, vegetation changes the CO₂ flux between the surface and the atmosphere via the biogeochemical effect.

of vegetation on each climate. This result would imply that the impact of vegetation on present-day climate is not valid for past and future climates. I pursue this hypothesis and ask the question

1. Does the impact of vegetation on climate depend on the climate state?

I address this question in Chapter 3 by estimating the impact of vegetation on the pre-industrial climate and on the early Eocene climate. I use the same climate model and experimental set-up for both climate states. In this way, a comparison between the impact of vegetation on both climates is possible. Both climates are simulated with forest on all continents and without any vegetation. From these two simulations, I derive the radiative forcing by forest and the strength of climate feedbacks induced by forest.

The stability of the vegetation-atmosphere system

The present-day vegetation-atmosphere system is suggested to be intransitive. This means that multiple vegetation-atmosphere states are suggested to exist for present-day boundary conditions (Lorenz 1968). The interaction of climate and vegetation causes these multiple vegetation-atmosphere states. For instance, Charney (1975) suggests that sparse vegetation in the Sahel maintains a dry climate due to the high albedo of bare soil. Vegetation lowers the albedo relative to bare soil and, hence, allows for stronger precipitation. In turn, precipitation favours plant growth. This interdependence leads to two possible vegetation states in the Sahel in climate simulations (Claussen 1998). Starting the simulation from a dense forest cover on all continents leads to a smaller Sahara desert than starting from bare soil on all continents. Other studies confirm multiple vegetation-atmosphere states in the Sahel (Brovkin et al. 1998; Wang and Eltahir 2000; Zeng and Neelin 2000; Zeng et al. 2004) and identify further multiple vegetation-atmosphere states in the Amazon region (Oyama and Nobre 2003) and in the Arabian desert (Claussen 1997).

Climates of the past offer the opportunity to analyse the stability of the vegetation-atmosphere system under different boundary conditions than today. For Last Glacial Maximum (LGM) conditions (21.000 years before present), Kubatzki and Claussen (1998) detect multiple vegetation-atmosphere states in the subtropical deserts. This result stresses that the vegetation-atmosphere system in the cold LGM climate is bistable like in the present-day climate. The stability of the vegetation-atmosphere in a warm, nearly ice-free climate has not been investigated so far. I close this gap and pose the question

2. Does the stability of the vegetation-atmosphere system differ in the early Eocene climate and in present-day climate?

I approach this question in Chapter 4. For both, early Eocene and pre-industrial conditions, I simulate climate and vegetation cover starting from two different states:

All continents are either completely covered by forest or without any vegetation. During the simulations, the vegetation cover establishes, migrates, and shrinks depending on climate. Until the end of the simulations, the vegetation cover and the atmosphere approach an equilibrium state. I analyse whether this equilibrium is the same for the two different initial vegetation covers.

Early Eocene plant species

Sewall et al. (2000) emphasise that the simulated early Eocene climate is sensitive to the assumed vegetation cover. They simulate the early Eocene climate with two different vegetation covers: an outdated vegetation map for the early Eocene and a revised, more realistic one. Seasonal temperature regionally differs by up to 6°C in the two simulations. This result implies that the correct vegetation cover is crucial to simulate the early Eocene climate properly.

To include a realistic vegetation cover, more and more palaeo-studies use Dynamic Global Vegetation Models (DGVMs) which simulate the global vegetation cover according to climate (Foley et al. 1998). For the deep past, however, DGVMs entail a problem: DGVMs consider Plant Functional Types (PFTs) which display present-day plant taxa, but plant taxa of the deep past differed from today. For instance, DGVMs consider grasses which are common today. Before the mid to late Miocene (16 - 5 Ma), however, grasses were rare (Janis 1993). Instead, other taxa were common which are extinct or rare today such as fern or paratropical rainforest. Those plant taxa are not considered by DGVMs.

The discrepancy between the PFTs and the plant taxa of the past has often been emphasised (Donnadieu et al. 2009; Loptson et al. 2014). Nevertheless, attempts to adapt the PFTs to plant taxa of the past are rare so far. Francois et al. (2011) adapt the PFTs in the DGVM CARAIB to represent the late Miocene plant taxa. A set of PFTs that represent early Eocene plant taxa, however, is absent. I take the first steps to develop early Eocene PFTs by answering the question

3. What limitations arise in the simulated early Eocene vegetation from using present-day PFTs?

I address this issue in Chapter 5 in which I simulate the early Eocene vegetation cover with the Max Planck Institute for Meteorology Earth System Model (MPI-ESM). The included DGVM uses present-day PFTs. The comparison of the simulated vegetation cover to vegetation reconstructions yields the discrepancies in the vegetation cover and plant taxa that arise from using present-day PFTs. Based on flora fossils, I evaluate in which way the plant taxa differed during the early Eocene and today and I develop ideas how to adapt the PFTs in the MPI-ESM to the early Eocene plant taxa.

In the next Chapter, I simulate the early Eocene climate with MPI-ESM. The model and the early Eocene boundary conditions are introduced in detail. I present the simulated early Eocene climate and highlight differences to pre-industrial climate. Further,

I compare the simulated early Eocene climate to temperature reconstructions. The evaluation of the simulated early Eocene climate is relevant to interpret the following results of this thesis. After addressing the above stated questions in Chapter 3 to 5, I conclude my results in Chapter 6. Further, I summarise the differing impact of vegetation on the early Eocene climate and on the pre-industrial climate as well as the specific stability of the vegetation-atmosphere system in each of both climates.

Modelling the Early Eocene Climate

2.1 Introduction

The focus of this thesis is on the interaction of vegetation and climate in the early Eocene climate. Climate reconstructions suggest that a warm climate prevailed during the early Eocene with a weak pole-to-equator temperature gradient and without permanent sea ice and ice sheets (Zachos et al. 2001). Hence, the early Eocene provides the opportunity to analyse vegetation-climate interactions in a climate that differs significantly from the present-day interglacial climate. Before I explore the interaction of vegetation and early Eocene climate, I investigate whether my model reproduces a warm, nearly ice-free climate that agrees with temperature reconstructions of the early Eocene epoch. For this purpose, I simulate the early Eocene climate using the Max Planck Institute for Meteorology Earth System Model (MPI-ESM) and I evaluate the simulated early Eocene climate focusing on two questions:

1. Does the simulated early Eocene climate agree with temperature reconstructions of this epoch?

Simulating the early Eocene climate matching reconstructions still remains a challenge. Most models fail to reproduce the high temperatures that prevailed in the high latitudes (Lunt et al. 2012). I compare the temperatures simulated by MPI-ESM to temperature reconstructions to estimate the discrepancies that result from the model and the Eocene set-up. Identifying these discrepancies becomes essential in Chapter 5 where I simulate and evaluate the early Eocene vegetation cover. A bias in the simulated climate might cause differences between the simulated and the reconstructed vegetation cover.

2. In which aspects does the simulated early Eocene climate differ from the pre-industrial climate?

I introduce the simulated early Eocene climate in detail and compare it to the pre-industrial climate. The differences between both climate states become relevant when I analyse why vegetation interacts differently with the early Eocene climate than with the pre-industrial climate.

In the following Section, I introduce MPI-ESM and I present the modelling set-up for the early Eocene simulation. I use a similar set-up as Heinemann et al. (2009) because they succeeded to simulate the early Eocene climate well using the atmospheric

general circulation model (GCM) ECHAM5 coupled to the Max Planck Institute Ocean Model (MPIOM). The successor of ECHAM5–ECHAM6–and MPIOM are included in MPI-ESM. In Section 2.4, I evaluate the simulated early Eocene climate. Firstly, I compare the early Eocene temperature to temperature estimates derived from marine and terrestrial proxies using the compilations by Lunt et al. (2012) and Huber and Caballero (2011). Secondly, I compare the simulated early Eocene climate to the pre-industrial climate. At the end of this Chapter, I conclude the outcome of the evaluation.

2.2 MPI-ESM

The Max Planck Institute for Meteorology Earth System Model (MPI-ESM) consists of the atmospheric GCM ECHAM6 (Stevens et al. 2013), the MPIOM (Jungclaus et al. 2013), the land surface scheme JSBACH (Reick et al. 2013), and the ocean biogeochemistry model HAMOCC (Ilyina et al. 2013). ECHAM6 and JSBACH run in a horizontal resolution of T31, which corresponds to approximately 3.75° times 3.75° . ECHAM6 considers 31 levels in the vertical up to 10 hPa. The ocean grid has a resolution of about 3° and consists of 40 levels in depth.

ECHAM6 calculates the state of the atmosphere. Adiabatic processes are described by the mixed finite-differences/spectral discretisation of the vorticity and divergence form of the primitive equations. Diabatic processes such as vertical mixing are mostly described by parametrisations because they are based on small-scale fluid dynamics which cannot be represented explicitly. The transport of tracers is calculated using the flux-form of the semi-Lagrangian scheme by Lin and Rood (1996).

ECHAM6 is the latest version of the ECHAM-series. The major difference to ECHAM5 is the representation of the short-wave radiative transfer in ECHAM6 (Stevens et al. 2013). The short-wave radiative transfer is represented by the radiative rapid transfer scheme for GCM (Iacono et al. 2008) instead of the four-band model by Fouquart and Bonnel (1980) as in ECHAM5. Further, the representation of the albedo has been improved: ECHAM6 considers the albedo of melt ponds on sea ice, calculates the albedo of snow on land dynamically, and accounts for the zenith dependence of the albedo over the ocean (Roeckner et al. 2012). Other than in ECHAM5, the triggering conditions of convection is not based on a constant temperature increment any more, but on the predicted variance of the virtual potential temperature.

JSBACH describes the land surface processes relevant for ECHAM6 on the same horizontal grid as ECHAM6. To account for sub-grid scale heterogeneities, each grid is separated into tiles (Brovkin et al. 2009). The used model version considers eight tiles (Table 2.1). Each tile refers to one Plant Functional Type (PFT). A PFT represents a group of plants with similar characteristics such as tropical trees. The fractions of all tiles in a grid cell describe the vegetation composition in the grid cell. Depending on this composition, JSBACH calculates fluxes of water, energy, moisture, and carbon dioxide (CO_2) in each grid cell.

Table 2.1: List of Plant Functional Types (PFTs) defined in the land surface scheme JSBACH and their classification in the dynamic vegetation module DYNVEG.

Classification	Plant Functional Type
Woody types	Tropical evergreen trees
	Tropical deciduous trees
	Extra-tropical evergreen trees
	Extra-tropical deciduous trees
	Raingreen shrubs
	Cold shrubs
Grass types	C ₃ grass
	C ₄ grass

JSBACH includes the dynamic vegetation module DYNVEG which calculates the vegetation cover according to climate (Reick et al. 2013). Based on net primary production (NPP), DYNVEG identifies regions where extreme climate conditions prevent plant growth and declares those regions to deserts. In the remaining regions, the bioclimatic limits prescribed for each PFT and disturbances determine the composition of the vegetation cover. A more detailed explanation of DYNVEG is given in Chapter 5.

MPIOM calculates the global ocean state based the primitive equations with hydrostatic and Boussinesq approximation (Marsland et al. 2003; Jungclaus 2006; Jungclaus et al. 2013). The ocean grid is a z-grid in the vertical and an orthogonal curvilinear C-Grid in the horizontal (Arakawa and Lamb 1977). The model provides a free surface elevation. The discretised bottom topography is fully resolved. Vertical eddy viscosity and diffusion is calculated using the scheme by Pacanowski and Philander (1981) as well as a wind mixing parametrisation. MPIOM represents isopycnal tracer mixing induced by unresolved mesoscale eddies based on the parametrisation by Gent et al. (1995).

MPIOM includes a sea-ice model which determines sea-ice dynamics based on viscouplastic rheology (Hibler 1979). Changes in sea-ice thickness are derived from radiative fluxes and turbulent fluxes in the atmosphere and from heat fluxes in the ocean (Jungclaus 2006). MPIOM resolves the sea-ice cover on a sub-grid scale by considering an ice-covered and an ice-free part of the grid cell (Notz et al. 2013).

The global ocean biogeochemistry model HAMOCC calculates the uptake of atmospheric CO₂ and the storage of carbon in the ocean covering time scales from days to millennia (Ilyina et al. 2013). HAMOCC is coupled dynamically to MPIOM and, hence, has the same temporal and spatial resolution as MPIOM. All biogeochemical tracers are treated in the same way as the thermohaline fields in MPIOM.

2.3 Model set-up for the early Eocene

Heinemann et al. (2009) succeed to simulate the early Eocene climate in agreement with climate reconstructions using ECHAM5 coupled to MPIOM. I use a similar setting as Heinemann et al. (2009) because MPI-ESM includes the successor of ECHAM5 and MPIOM. I use the orography and bathymetry map by Bice and Marotzke (2001) which Heinemann (2009) extrapolated from the original resolution of 2° times 2° to the model resolution of T31. The orography map lacks information on sub-grid orography (standard deviation, anisotropy, maximum/minimum elevation, mean slope, mean orientation, mean elevation of orographic features). Hence, ECHAM6 cannot parametrise sub-grid interactions of atmospheric flow with orography (Stevens et al. 2013) and I switch off the module for sub-grid orographic drag and wave generation in ECHAM6. Owing to the early Eocene continent distribution, Heinemann et al. (2009) shift the regular MPIOM north pole of the ocean grid to Palaeo-Asia and the grid south pole to Palaeo-South America. I use the changed ocean grid as well.

Like in Heinemann (2009), the atmospheric CO_2 concentration is fixed to 560 ppm, which represents the lower limit of reconstructions (Zachos et al. 2001; Beerling and Royer 2011). Reconstructions of other greenhouse gases are absent for the early Eocene. Thus, I proceed similar to Heinemann (2009) and prescribe pre-industrial values for methane and nitrous oxide in the early Eocene atmosphere (Table 2.2).

Orbital parameters change on shorter time scales than the early Eocene period lasts (Laskar et al. 2004). Hence, a specific set of orbital parameters for the early Eocene is lacking. Other than Heinemann et al. (2009), I decide to use a module in ECHAM6 that calculates the distance to the sun and the ascension and declination of the sun depending on the simulated year. Using this module, the orbital parameters approximately refer to the year 800 in early Eocene simulation. This is the same orbit as in the pre-industrial equilibrium simulation which I use for comparison in this study.

The early Eocene simulation runs with a fixed homogeneous savannah-like vegetation like in the simulation by Heinemann (2009). Forest and grass cover 16 % and 24 % of each grid cell on land, respectively. The leaf area index (LAI) is homogeneously 2.3. Other than Heinemann (2009), I derive the soil albedo from present-day soil albedo. In regions where early Eocene continents coincide with present-day continents, I prescribe the satellite-derived present-day soil albedo. In other regions, the soil albedo is 0.16. The setting of other parameters is listed in Table 2.2.

The early Eocene simulation starts from the equilibrium ocean state by Heinemann (2009). The atmosphere starts from rest. The simulation runs for 300 years with a static vegetation cover. At the end of the simulation, the global mean surface temperature and sea surface temperature approach a new equilibrium. In the deep ocean, a small but significant trend in temperature of 0.04 K per 100 years remains.

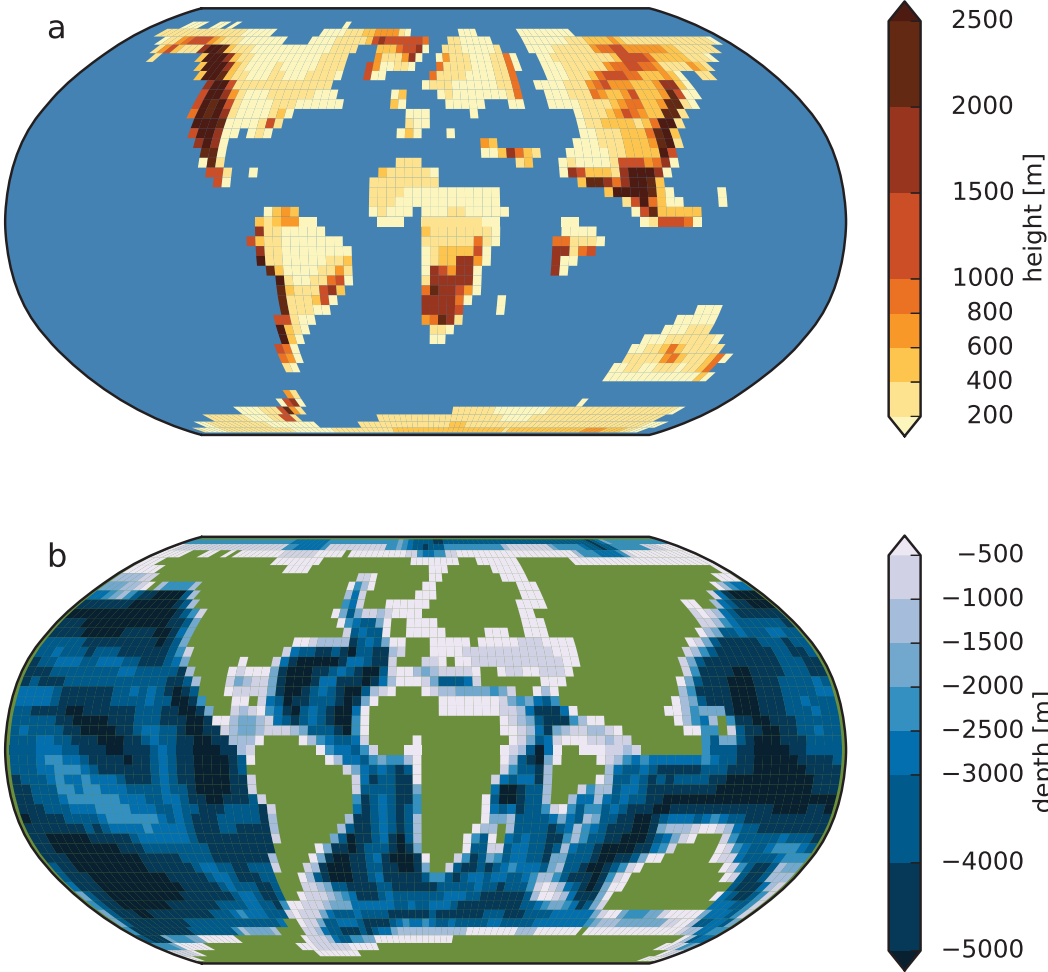


Figure 2.1: Orography map (a) and bathymetry map (b) prescribed in the early Eocene simulation. The maps are derived from the maps by Bice and Marotzke (2001).

Table 2.2: Boundary conditions in the early Eocene climate simulation and in the pre-industrial climate simulation which is used for comparison. The soil flag expresses the heat capacity and diffusivity of soils.

	Pre-industrial	Early Eocene
CO ₂ concentration	280 ppm	560 ppm
Methane	0.8 ppm	0.8 ppm
Nitrous oxide	0.288 ppm	0.288 ppm
Orbit	year 800	approx. year 800
Bathymetry and orography	present-day	Bice and Marotzke (2001)
Vegetation ratio	dynamic	0.4
Forest fraction	dynamic	0.16
Leaf area index	dynamic	2.3
Soil albedo	satellite-based	0.16/satellite-based
Surface roughness length	dynamic	1.6 m
soil flag based on FAO	dynamic	3 (similar to mudd)

2.4 Results: The early Eocene climate

The model simulates a warm early Eocene climate. Global annual mean temperature is 24° C. Even in the high latitudes, annual mean temperature is above the freezing point leading to an ice-free ocean in summer. In the following, I evaluate the simulated climate in two ways. Firstly, I compare the early Eocene climate to temperature reconstructions. Secondly, I present the simulated early Eocene in detail and compare it to the pre-industrial climate.

2.4.1 Comparison to temperature reconstructions

I compare the simulated early Eocene climate to marine and terrestrial temperature reconstructions. The marine temperature estimates originate from the data compilation by Lunt et al. (2012) which includes palaeotemperature estimates at the sea surface, near the sea surface, and in shallow inner-shelf bottom water. The temperature reconstructions are based on oxygen isotope ($\delta^{18}O$) values and Magnesium-Calcium ratios (Mg/Ca) derived from planktic foraminifera as well as on TEX₈₆. In all measurement sites, several methods have been applied to estimate the temperature. Like Lunt et al. (2012), I use the average over all temperature estimates in one site. The compilation includes temperature reconstructions from just before the onset of the Paleocene-Eocene Thermal Maximum (PETM) until the Early Eocene Climatic Optimum (EECO). Temperature estimates of the PETM itself are excluded from the data compilation. I further neglect temperature reconstructions of the EECO in my comparison.

Huber and Caballero (2011) provide a compilation of monthly annual mean temperature for the early Eocene based on terrestrial proxy data. Most temperature estimates in this compilation result from the analysis of macrofloral assemblage data. The used

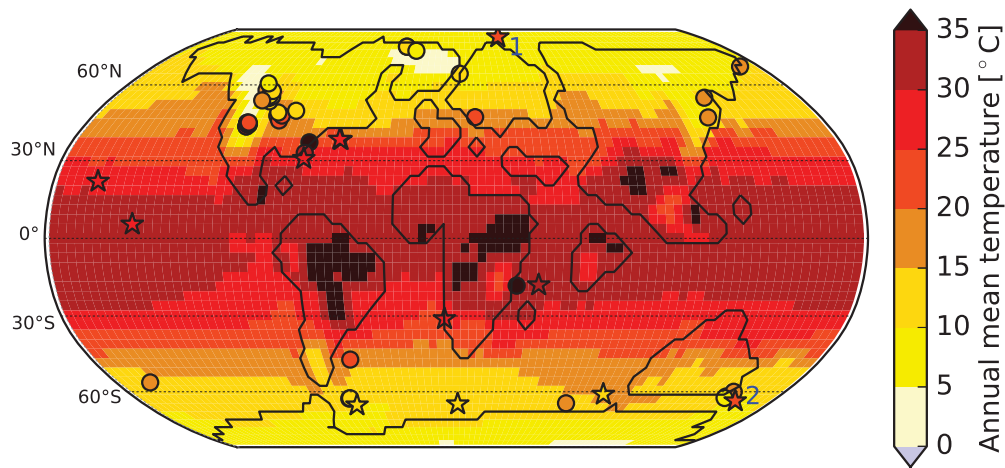


Figure 2.2: Annual mean 2-m temperature in the early Eocene simulation in shaded colours. Stars show reconstructed annual mean SST derived from the marine proxy data compilation by Lunt et al. (2012). The data compilation includes temperature estimate based on $\delta^{18}\text{O}$, Mg/Ca, and TEX₈₆ estimates. The numbers 1 and 2 mark SST reconstructions by Sluijs et al. (2006) and Bijl (2009), respectively. Cycles refer to terrestrial annual mean temperature estimates provided by Huber and Caballero (2011). Reconstructions are derived from macrofloral and palynoflora assemblage data and from teeth, hydrogen isotopes, and oxygen isotopes.

analysing techniques are the Climate-Leaf Analysis Multivariate Program (CLAMP) (Wolfe 1995) and the Leaf Margin Analysis (LMA) (Wilf 1997). Further, the compilation by Huber and Caballero (2011) includes temperature estimates based on teeth, hydrogen isotopes, oxygen isotopes, and palynoflora assemblage data.

The simulated early Eocene annual mean temperatures show a good agreement with the marine temperature estimates in the tropics and subtropics (Figure 2.2). In the mid to high latitude, discrepancies between the simulated early Eocene temperature and the temperature estimates appear. In North America, some reconstructions indicate a warmer climate than the simulation, others indicate a colder climate. The reason for the large spread of temperature estimates is the mountainous terrain that appeared in this region during the early Eocene. The reconstructed temperature varies strongly because the altitude changes over small distances. The model fails to reproduce the small-scale temperature variations because small-scale orographic features are not resolved.

In the northern high latitudes, terrestrial temperature reconstructions indicate a warmer climate than in the simulation. North of Greenland, the marine temperature reconstruction by Sluijs et al. (2006) strongly exceeds the simulated annual mean temperature (Figure 2.2). The SST estimate by Sluijs et al. (2006) is derived from TEX₈₆, which likely has a bias to summer temperatures (Sluijs et al. 2006). Considering summer temperatures, the model produces a 5°C lower temperature than suggested by Sluijs et al. (2006) in this region.

In the southern high latitudes, the simulation agrees with marine and terrestrial temperature estimates. The only exception is the SST reconstruction by Bijl (2009) that suggests temperature of 24°C at the Tasman Plateau (Figure 2.2). Like Sluijs et al.

Table 2.3: Comparison of the simulated pre-industrial climate and the early Eocene climate in terms of the global annual mean values. For the snow cover, the average over land is considered. For the sea-ice cover, the average over the ocean is considered. The meridional temperature gradient is defined in Equation 2.1.

	Pre-industrial	Early Eocene
Surface temperature [°C]	14.0	24.0
Meridional temperature gradient [°C/°]	-0.61	-0.37
Precipitation [mm/day]	2.75	3.56
Relative cloud cover	0.63	0.57
Relative snow cover	0.21	0.06
Relative sea ice cover	0.06	0.0

(2006), Bijl (2009) use TEX_{86} to estimate SST. Hence, the temperature estimate likely has a bias to summer temperatures, too. Considering the summer temperature, the simulation is still too cold by 9°C over the southern Pacific Ocean.

The cold bias in the high latitudes is well-known in climate models. Lunt et al. (2012) compare early Eocene simulation of several climate models and all of them show the cold bias in the high latitudes. Interestingly, the models with the highest atmospheric CO_2 concentration have the smallest bias in the high latitude, while tropical temperatures still agree with reconstructions. In my simulation, the atmospheric CO_2 concentration is at the lower limit of CO_2 reconstructions. For low- CO_2 simulations, Lunt et al. (2012) assume that increasing the atmospheric CO_2 might decrease the cold bias in the high latitudes.

2.4.2 Comparison to the pre-industrial climate

I compare the simulated early Eocene climate to the simulated equilibrium pre-industrial climate by Port et al. (2012). Port et al. (2012) use the earlier version of MPI-ESM, which includes ECHAM5 instead of ECHAM6. In the pre-industrial simulation, the atmospheric CO_2 concentration is 275 ppm (Table 2.2). Present-day continent distribution, orography, bathymetry, and ice sheets are prescribed. The soil albedo is derived from satellite maps of present-day earth. Vegetation is calculated dynamically by the dynamic vegetation module in JSBACH.

The global annual mean temperature is about 10°C higher in the early Eocene climate than in the pre-industrial climate (Table 2.3). While the warming is weak in the tropics with 6.4°C (averaged from 13° south to 13° north), the warming is strongest in the high latitudes (Figure 2.3). Over Antarctica, temperature is 41.2°C higher (averaged from 60° south to the South pole) in the early Eocene climate than in the pre-industrial climate. The warming results from the warmer climate and from the lower elevation of Antarctica when ice sheets are absent. In the northern high latitudes, temperature is 17.3°C higher (averaged from 60° north to the North pole) in the early Eocene climate.

The warming is stronger in the high latitudes than in the tropics. Hence, the meridional temperature gradient is weaker in the early Eocene climate than in the pre-industrial

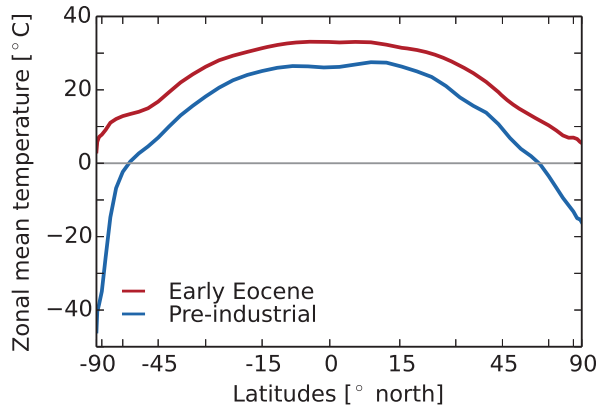


Figure 2.3: Zonal mean surface temperature averaged over 30 years in the early Eocene climate (red line) and in the pre-industrial climate (blue line).

climate (Figure 2.5). I quantify the meridional temperature gradient by calculating the change in zonal mean surface temperature, $[T]$, with increasing latitude, ϕ ,

$$\frac{\Delta[T]}{\Delta\phi} = \frac{[T]_2 - [T]_1}{\phi_2 - \phi_1}. \quad (2.1)$$

The zonal mean temperature is almost constant in the tropics. Hence, I consider the change from $\phi_1 = 17^\circ$ north to $\phi_2 = 87^\circ$ north. For the pre-industrial climate, Equation 2.1 indicates that zonal mean temperature decreases by 0.61°C per degree of latitude (Table 2.3). In the early Eocene climate, the decline in zonal mean temperature is 40 % weaker than in the pre-industrial climate.

Permanent sea ice is absent in the early Eocene climate. Seasonal sea ice forms rarely in the Arctic Ocean. The snow cover is significantly smaller in the early Eocene than in the pre-industrial climate. Figure 2.5 illustrates the snow-cover extent at the end of the winter in the respective hemisphere in both climate states. In the pre-industrial climate, the snow cover extends up to 50° south, while the snow cover is limited to the Antarctic continent in the early Eocene climate. The snow cover reaches from 90° north to 45° north in pre-industrial climate. In the early Eocene climate, the snow cover extends to 60° north in plain regions. Only in mountainous regions, the snow cover reaches 40° north.

The hydrological cycle is stronger in the early Eocene climate than in the pre-industrial climate which manifests in a 17 % stronger precipitation and evaporation. The zonal precipitation pattern is intensified relative to the pre-industrial climate: Precipitation is stronger in the tropics and mid latitudes, while precipitation is weaker in the subtropics. The different distribution of continents in both climates leads to regional precipitation differences such as in the region of the Tethys Ocean. Australia was located in the mid latitudes during the early Eocene leading to stronger precipitation than in pre-industrial Australia. The polar regions receive more precipitation in the early Eocene climate than in the pre-industrial climate due to the absence of permanent sea ice and ice sheets in the early Eocene climate.

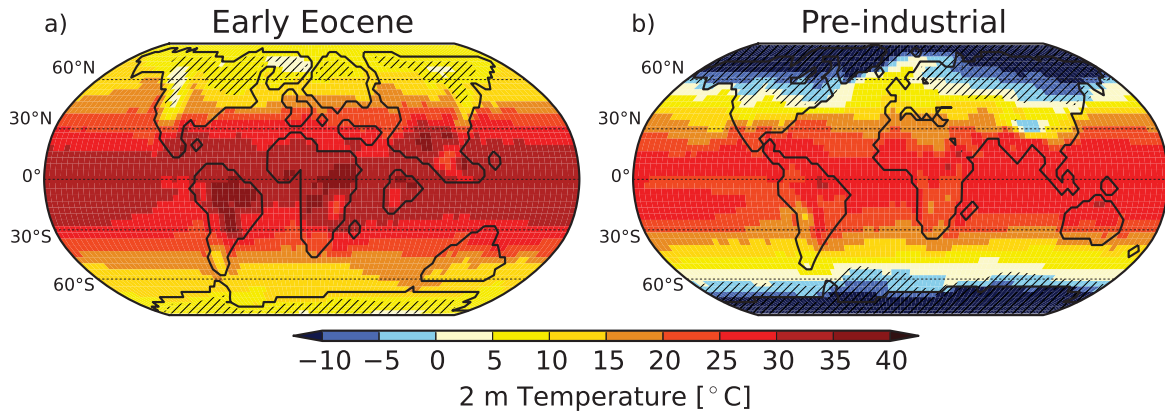


Figure 2.4: Annual-mean 2-m temperature in the early Eocene climate (a) and in the pre-industrial climate (b). In hatched regions, snow cover and sea-ice cover exceeds 0.3 at the end of the respective hemispheric winter (March in the northern hemisphere and September in the southern hemisphere).

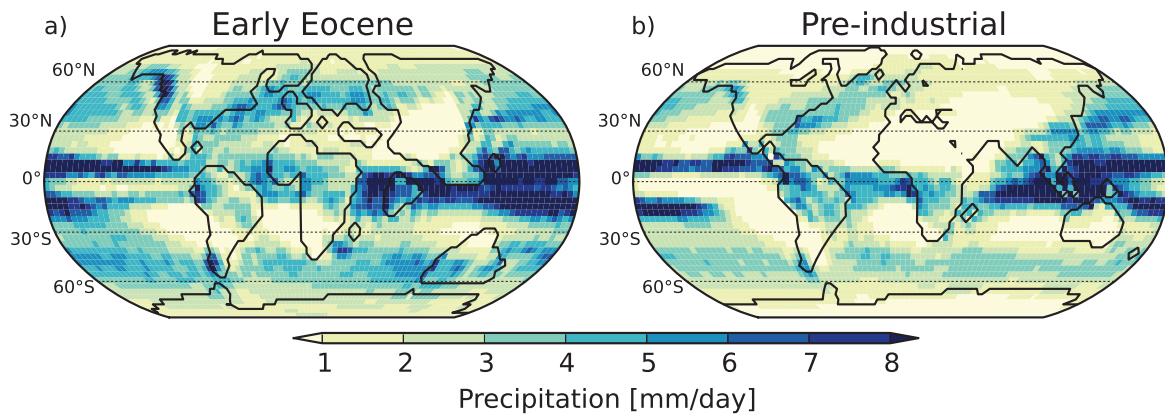


Figure 2.5: Annual mean precipitation in the early Eocene climate (a) and in the pre-industrial climate (b).

2.5 Conclusion

I evaluate the early Eocene climate simulation performed with the MPI-ESM. The comparison of the simulated early Eocene climate to temperature reconstructions illustrates that the simulated climate agrees with temperature reconstructions in the tropics. At the high latitudes, however, temperatures are lower in the simulation than reconstructions suggest. The cold bias in the high latitudes becomes relevant in Chapter 5 where I simulate the vegetation cover according to the early Eocene climate.

The comparison of the simulated early Eocene climate with the pre-industrial climate indicates that global mean temperature is significantly higher in the early Eocene climate. Further, the pole-to-equator temperature gradient is weaker. Even in the high latitudes, annual mean temperature is above the freezing point leading to an ice-free ocean in summer. The global annual mean evaporation and precipitation is stronger than in the pre-industrial climate indicating a stronger hydrological cycle. Different spatial precipitation patterns evolve in both climates due to the specific distribution of continents and the differences in the sea-ice and ice-sheet cover. The specific early Eocene climate and the distribution of continents are the reason for different vegetation-climate interactions in both climates which will be discussed in Chapter 3 and 4.

Despite the cold bias in the high latitudes, the simulated early Eocene climate is warmer, more equable, and more humid than the pre-industrial climate. With these characteristics, the simulated early Eocene climate represents an ideal test bed to explore vegetation-climate interactions in a warm, nearly ice-free climate.

Chapter 3

Radiative Forcing by Forest and Subsequent Feedbacks

3.1 Introduction

In the present-day climate, forest tends to warm the northern high latitudes and forest tends to cool the tropics. In the northern high latitudes, leaves and stems mask the bright snow cover and reduce the surface albedo strongly (Bonan 1992; Betts and Ball 1997; Bonan 2008). The sea-ice albedo feedback amplifies warming by trees (Claussen et al. 2001; Fraedrich et al. 2005; Brovkin et al. 2009). In the tropics, transpiration and evaporation from trees enhance the cloud cover leading to an increased planetary albedo. Further, transpiration and evaporation from trees enhance latent heat flux and reduce sensible heat flux. The increase in albedo and the shift in heat fluxes lead to a cooling (Bathiany et al. 2010).

In climates different from present-day's climate, the strength of biogeophysical processes and feedbacks might change. Otto-Bliesner and Upchurch (1997) investigate the impact of vegetation on the Late Cretaceous climate (66 Million years ago) which was warmer than present-day climate. Their simulations reveal that trees warm the high latitudes also in the late Cretaceous climate by masking the snow cover. The ice-albedo feedback amplifies the warming by trees.

In the simulation by Otto-Bliesner and Upchurch (1997), substantial sea-ice coverage in the North Pacific Arctic occurs in winter and spring. In a climate that was presumably warmer than the Late Cretaceous and nearly free of ice, the snow masking effect by trees and the sea-ice albedo feedback will be weak. Hence, the vegetation will affect a warm nearly ice-free climate differently than the present-day climate. The early Eocene climate (54-52 Ma) was such a warm nearly ice-free climate. Annual mean temperature on Seymour Island (65° south) was 10°C (Ivany et al. 2008). Alligators (Markwick 1994) and tortoises (Hutchison 1982) on Ellesmere Island (76° north) imply above freezing temperature during the whole year in the northern high latitudes. In agreement with proxy data (Zachos et al. 1992), no permanent sea ice occurs in early Eocene climate simulations by Heinemann et al. (2009).

Here, I investigate the impact of vegetation on two different climate states: on pre-industrial interglacial climate which is characterised by an extended perennial Arctic sea-ice cover and snow cover and on a warm, nearly ice-free and snow-free climate such as the early Eocene climate. Plant taxa during the early Eocene differed from today.

For instance, grasslands did not exist during the early Eocene (Willis and McElwain 2002). Instead, other plant taxa prevailed that are rare or extinct today such as polar forest and paratropical rainforest (Wolfe 1985). Since the bioclimatic limits and the physiology of early Eocene plant taxa are known only to a limited extent, I prescribe an extreme vegetation coverage. To explore first-order effects, I simulate pre-industrial climate and early Eocene climate with a dense forest on all continents or with bare soil on all continents, respectively.

Based on the differences in temperature and radiative flux between the respective 'forest world' and the respective 'desert world', I derive the radiative forcing by forests and the subsequent climate feedbacks. I expect that the radiative forcing by forest depends on the soil albedo. To isolate the impact of soil albedo on the radiative forcing by forest, I simulate the desert world two times. In a first case, a homogeneous soil albedo of 0.1 is used, which is approximately the albedo of volcanic rocks and granite bedrock (Warner 2004). In this case, soil and vegetation have similarly low values of albedo. In a second case, a homogeneous soil albedo of 0.4 is taken. The bright soil has a much higher albedo than the vegetation.

For the early Eocene climate and the pre-industrial climate, I prescribe an atmospheric carbon dioxide (CO_2) concentration of 560 ppm and 280 ppm, respectively. For each climate, the respective CO_2 concentration is assumed in the forest world and in the desert worlds. Thus, I neglect the biogeochemical effect of vegetation and I consider the biogeophysical effect of forest.

3.2 Model and experiments

Using the Max Planck Institute for Meteorology Earth System Model (MPI-ESM), I perform the same three simulations with early Eocene boundary conditions (Chapter 2) and pre-industrial boundary conditions (Table 3.1). The pre-industrial simulations run with the same concentration of atmospheric methane and nitrous oxide as the early Eocene simulations (Table 2.2). For both climates, orbital parameters are derived from the simulated year (Chapter 2). The simulations for both climates run from the year 800 to 1200. Hence, the orbital parameters represent the orbit of this time in both climates. This approach limits the differences between the early Eocene and the pre-industrial boundary conditions to the distribution of the continents, the bathymetry,

Table 3.1: Simulations performed with boundary conditions for the early Eocene climate and the pre-industrial climate. The listed vegetation cover is prescribed on all ice-free continents. The values for the surface albedo refers to the land surface. In the desert world, the soil albedo equals the surface albedo. In the forest world, trees cover the soil completely and the albedo of the forest determines the surface albedo.

	Vegetation	Surface albedo
Dark desert world	none	0.1
Bright desert world	none	0.4
Forest world	100% tree cover	0.12

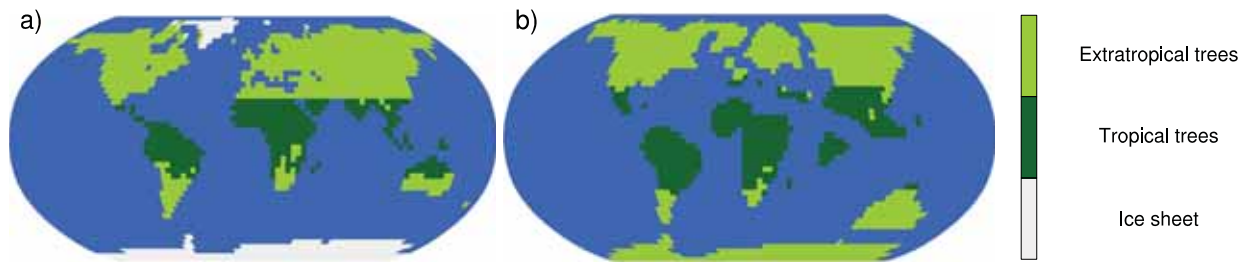


Figure 3.1: Vegetation cover in the forest world for pre-industrial (a) and early Eocene boundary conditions (b). Extra-tropical trees and tropical trees differ concerning their leaf area index and roughness length.

the appearance of ice sheets, and the atmospheric CO_2 concentration. All simulations start from the equilibrium early Eocene climate and pre-industrial climate introduced in Chapter 2.

In the *dark desert world* and in the *bright desert world*, no vegetation occurs on all continents. Both simulations differ concerning the assumed soil albedo. While all soils have an albedo of 0.1 in the dark desert world, all soils have an albedo of 0.4 in the bright desert world. In the *forest world*, tree cover is 100% on all ice-free continents. The vegetation cover is static and the leaf area index (LAI) is constant throughout the whole simulation independently of season, temperature, and water availability. I distinguish between tropical and extra-tropical trees (Figure 3.1). Tropical trees have a LAI of 7 and a roughness length of 2 m. Extra-tropical trees have a LAI of 5 and a roughness length of 1 m. The soil albedo does not matter in the forest world which was tested by simulating the forest world climate with low and high soil albedo, respectively. Both soil albedo values reveal the same climate (not shown here) because trees completely mask the soil leading to a land surface albedo of approximately 0.12 in snow-free regions in the forest world.

3.3 Methods

I estimate the radiative forcing by forest and the subsequent climate feedbacks based on the comparison of the forest world to the desert worlds. The first part of this Section introduces the linear regression approach which I use to quantify the radiative forcing and the strength of climate feedbacks. This linear regression approach is derived from the approach by Gregory et al. (2004). The second part of this Section presents the technique I apply to separate the net radiative forcing and the net climate feedback into their single components. This separation reveals the mechanisms by which forest affects climate.

3.3.1 Radiative forcing and climate feedbacks

At the beginning of each simulation, I change the vegetation cover and the soil albedo drastically. The modification of the land surface acts as an external forcing on the

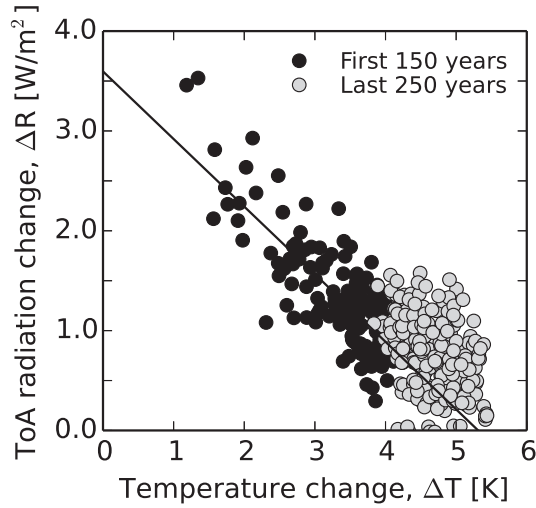


Figure 3.2: Evolution of radiative flux at the top of the atmosphere with temperature changes in the early Eocene bright desert world. At the beginning of the simulation, savannah-like vegetation is replaced by bare soil with an albedo of 0.4. Black points refer to the first 150 simulated years. Gray points reflect the remaining 250 years. The black line is the regression line fitted to the first 150 years.

climate system and perturbs the radiation balance at the top of the atmosphere (ToA). During the simulation, the perturbation in the ToA radiation balance, ΔR , changes surface temperature. Temperature changes induce mechanisms in the climate system that feed back to ΔR . In the global mean, ΔR is assumed to relate linearly to the temperature changes, ΔT ,

$$\Delta R(t) = \Delta Q + \lambda \Delta T(t). \quad (3.1)$$

The instantaneous response of radiative flux to the modification of the land surface is called radiative forcing, ΔQ . The climate feedback parameter¹, λ , quantifies the strength of feedbacks between temperature and ΔR .

From the model simulations, I obtain pairs of ΔR^i and ΔT^i for each year, i . Figure 3.2 shows the points of $(\Delta T^i, \Delta R^i)$ for the early Eocene bright desert world simulation. The initial climate for this simulation is the early Eocene climate presented in Chapter 2. The initial climate is the equilibrium climate that established with savannah on all continents. In the first year, savannah is replaced by bright desert, and the simulated climate progressively approaches a new equilibrium. The straight line fitted to the points of $(\Delta T^i, \Delta R^i)$ yields the parameters in Equation 3.1 (Gregory et al. 2004). The intersection of the regression line with the ΔR -axis, ΔR is the radiative forcing ΔQ . The slope of the regression line is the feedback parameter λ . λ is negative here indicating that feedbacks stabilise climate because they counteract the perturbation in the ToA radiation balance. The new climate equilibrium is defined by the intersection of ΔR with the ΔT -axis, i.e. the perturbation ΔR approaches zero, and the new equilibrium temperature is

¹Note that the Equation 3.1 might differ from other studies which use $\Delta R(t) = \Delta Q - \lambda \Delta T(t)$. In this case, $-\lambda$ is defined as feedback parameter.

$$\Delta T^{eq} = -\frac{\Delta Q}{\lambda}. \quad (3.2)$$

This approach likely underestimates the equilibrium temperature response because the slope of the regression line is not constant in time but decreases during the simulation (Gregory et al. 2004). Gregory et al. (2004) consider a few decades of a simulation performed with an Atmosphere Ocean General Circulation Model. They find that the slope of the regression line is constant for this time. In line with Gregory et al. (2004), I use the first 150 years of my simulation for the regression.

Here, I focus on the difference between the forest world and the desert world. Therefore, I combine two perturbation experiments. Let ΔR_d be the perturbation of the net radiation at the top of the atmosphere in the case of replacing savannah with desert and ΔR_f the perturbation in the case of replacing savannah with forest. In the linear approach, the difference, ΔR_{fd} , is the perturbation due to replacing deserts by a complete tree cover. For each year in the simulation, i , I receive

$$\Delta R_{fd}^i = \Delta R_f^i - \Delta R_d^i. \quad (3.3)$$

Consistently, I subtract the temperature differences of the two perturbation experiments to obtain

$$\Delta T_{fd}^i = \Delta T_f^i - \Delta T_d^i = T_f^i - T_d^i. \quad (3.4)$$

Considering Equation 3.1, the regression line to the points $(\Delta T_{fd}, \Delta R_{fd})$ is

$$\Delta R_{fd} = \Delta Q_{fd} + \lambda_{fd} \Delta T_{fd}. \quad (3.5)$$

The difference in radiative forcing between the forest world and the desert world, $\Delta Q_{fd} = \Delta Q_f - \Delta Q_d$ reflects the radiative forcing of afforesting the desert world. The feedback parameter for afforesting the desert world is λ_{fd} . The equilibrium temperature response, ΔT_{fd}^{eq} , is approximated by the intersection $\Delta R_{fd}(\Delta T_{fd} = 0)$.

3.3.2 Decomposition of the radiation balance

Net perturbation in the ToA radiation balance consists of a long-wave component (LW) and a short-wave component (SW). Both components constitute of a cloud share (cl) and a clear-sky share (cs) leading to

$$\Delta R = \Delta R_{LWcl} + \Delta R_{LWcs} + \Delta R_{SWcl} + \Delta R_{SWcs} \quad (3.6)$$

The clear-sky share in radiation reflects the radiation when clouds are neglected. The cloud share refers to the difference between the clear-sky radiation and the radiation when clouds are considered. I apply the linear regression technique on each of the four radiation components. The corresponding regression lines are described by

$$\Delta R_{LWcl} = \Delta Q_{LWcl} + \lambda_{LWcl} \Delta T, \quad (3.7)$$

$$\Delta R_{LWcs} = \Delta Q_{LWcs} + \lambda_{LWcs} \Delta T, \quad (3.8)$$

Table 3.2: Mechanisms that cause the respective radiation forcings and feedbacks in the simulations.

Abbreviation	Mechanism
ΔQ_{SWcs}	Radiative forcing by changed surface albedo
ΔQ_{SWcl}	Radiative forcing by changed planetary albedo due to clouds
ΔQ_{LWcl}	Radiative forcing by changed greenhouse effect due to clouds
ΔQ_{LWcs}	Radiative forcing by changed greenhouse effect
λ_{SWcs}	Ice-albedo feedback
λ_{SWcl}	Cloud albedo feedback
λ_{LWcl}	Cloud water-vapour feedback
λ_{LWcs}	Planck feedback, water-vapour feedback, lapse-rate feedback
λ_{WV+LR}	Lapse-rate/water-vapour feedback

$$\Delta R_{SWcl} = \Delta Q_{SWcl} + \lambda_{SWcl} \Delta T, \quad (3.9)$$

$$\Delta R_{SWcs} = \Delta Q_{SWcs} + \lambda_{SWcs} \Delta T. \quad (3.10)$$

This approach separates net radiative forcing and feedback into the single components of radiation (Andrews et al. 2012).

Table 3.2 gives an overview over the main mechanisms that cause the respective radiative forcing and feedback in the simulations. Forest induces a radiative forcing by modifying the land surface albedo, the cloud cover, and the water content in the atmosphere. The short-wave clear-sky radiative forcing, ΔQ_{SWcs} , results from surface albedo changes by forest relative to bare soil.

The short-wave cloud radiative forcing, ΔQ_{SWcl} , reflects the forcing by albedo changes due to cloud cover changes. Forest increases the cloud cover because trees transpire water and intercept precipitation. Hence, trees enhance evaporation and more clouds can form. A larger cloud cover increases planetary albedo and less short-wave radiation reaches the surface. Further, clouds enhance the greenhouse effect because water is a greenhouse gas. The radiative forcing by changes in the greenhouse effect of clouds is captured by the long-wave cloud radiative forcing, ΔQ_{LWcl} .

The long-wave clear-sky radiative forcing, ΔQ_{LWcs} , refers to changes in the greenhouse effect of the atmosphere. Clouds are neglected in this case. In my study, the concentration of CO₂, methane, and nitrous oxide in the atmosphere are fixed. The only variable greenhouse gas is water vapour. Hence, ΔQ_{LWcs} refers to the radiative forcing by an increased humidity due to forest.

Analogous to the separation of the net radiative forcing, the net feedback parameter decomposes into four components. The short-wave clear-sky feedback parameter, λ_{SWcs} , quantifies the strength of the sea-ice/snow albedo feedback. This feedback is suggested to be positive. To illustrate this feedback, I assume a warming by any forcing. The sea-ice and the snow cover shrink due to this warming. The resulting decrease in surface albedo amplifies the warming. The warming is most pronounced in the high latitudes where the sea-ice and snow cover decreases.

The long-wave and short-wave cloud feedback parameter, λ_{LWcl} and λ_{SWcl} , describe cloud feedbacks. In a warming world, the cloud cover is suggested to increase because more water evaporates from the ocean. More clouds enhance the greenhouse effect of water vapour leading to an additional warming. This positive cloud water-vapour feedback is captured by λ_{LWcl} . Further, more clouds increase planetary albedo. This effect counteracts the warming. This negative cloud albedo feedback is described by λ_{SWcl} .

The long-wave clear-sky feedback parameter, λ_{LWcs} , refers to the sum of the Planck feedback, the water vapour feedback, and the lapse rate feedback. The Planck feedback, λ_P , results from the increased emission of long-wave radiation when the earth surface temperature changes. For instance, a warming increases the emission of long wave radiation by the surface leading to an energy loss at the top of the atmosphere. The energy loss induces a cooling. Hence, the Planck feedback counteracts the initial warming and stabilises climate.

I estimate λ_P for the early Eocene climate and for the pre-industrial climate using a simple zero dimensional energy balance model

$$\lambda_P = \frac{\partial R}{\partial T} = -4\sigma\epsilon T^3. \quad (3.11)$$

The term on the right hand side consists of the Stefan-Boltzmann constant, σ , and the emissivity of the atmosphere, ϵ . The emissivity describes the strength of the greenhouse effect and varies depending on the climate state. The pre-industrial climate and the early Eocene climate introduced in Chapter 2 have an emissivity of 0.585 and 0.541, respectively. Considering the different emissivity values and global mean surface temperatures in Kelvin (Table 2.3), Equation 3.11 yields a Planck feedback of -3.1 W/m² and -3.3 W/m² in the pre-industrial climate and in the early Eocene climate, respectively. Assuming that feedbacks act linearly, I subtract λ_P from λ_{LWcl} . The remaining feedback factor is the lapse-rate/water-vapour feedback which I name λ_{WV+LR} .

I quantify the uncertainty of radiative forcings and feedback parameters in terms of the 95% confidence interval which I assess using bootstrapping. I randomly select 150 pairs of differences in temperature and ToA radiative flux out of the first 150 years of the respective simulation. Each pair of the simulation can be selected several times for the selection. I repeat the resampling 10.000 times. From each time, I estimate the feedback parameters and radiative forcings. I sort the resulting 10.000 values for the feedback parameter and the radiative forcing. Truncating the upper and lower 2.5% provides the 95% confidence interval.

3.4 Results

I present the results for the bright soil case and for the dark soil case separately. For both soil albedo cases, I analyse the early Eocene simulations and the pre-industrial simulations in the same way. I compare the forest world with the respective desert

world. Differences in surface temperature and ToA radiative flux between both simulations reveal the radiative forcing of afforestation and resulting feedbacks. I compare the estimated radiative forcing and feedback parameters for both climates with each other.

3.4.1 Afforestation of a bright desert world

Relative to the bright desert world, the forest world is 4.3 K and 5.7 K warmer at the end of the early Eocene simulations and of the pre-industrial simulations, respectively. The warming results from a positive radiative forcing by trees which is 5.8 W/m² and 5.2 W/m² in the early Eocene climate and in the pre-industrial climate, respectively (Table 3.3). Figure 3.3 shows the evolution of differences in the ToA radiative flux between the forest world and the bright desert world with differences in near-surface temperature. Considering the confidence interval, the radiative forcing by trees is similarly strong in early Eocene climate as in pre-industrial climate.

The slope of the regression line is steeper in the early Eocene climate than in the pre-industrial climate (Figure 3.3), i.e. feedbacks stabilise the early Eocene climate stronger than the pre-industrial climate. Stronger stabilising feedbacks lead to a smaller equilibrium temperature response, ΔT_{equ} , and a smaller temperature difference between the bright desert world and the forest world at the end of the simulations (Table 3.3).

The main part of the radiative forcing results from surface albedo changes as the short-wave clear-sky component of the radiative forcing, ΔQ_{SWcs} , indicates (Figure 3.4). Q_{SWcs} amounts to some 15 W/m² in both climate states and exceeds the other components of the radiative forcing. To evaluate the surface albedo changes by forest, I assess the difference in the land surface albedo between the forest world and the bright desert world in the first year of the simulations. In the first year, the surface albedo differences are mainly attributed to the contrasting vegetation cover. The response of the climate system to the radiative forcing by forest is weak in the first year. Hence, changes in the snow cover and in the sea-ice cover due to forest are small. In the global mean, the land surface albedo is 0.28 lower in the forest world than in the bright desert world in the early Eocene climate. In the pre-industrial climate, the land surface albedo

Table 3.3: Net radiative forcing by afforesting a bright desert world in the early Eocene climate and the pre-industrial climate. Further, the net feedback parameter and the equilibrium temperature change are listed. The values are derived from the comparison of the respective forest world with the respective bright desert world. The 95% confidence interval is given. The transient temperature change refers to the temperature difference at the end of both simulations.

	Early Eocene	Pre-industrial
Radiative forcing [W/m ²]	5.8 ± 0.4	5.2 ± 0.5
Feedback parameter [W/m ² K]	-1.4 ± 0.1	-0.7 ± 0.1
Equilib. temperature change [K]	4.1 ± 0.1	7.3 ± 0.7
Transient temperature change [K]	4.2	5.7

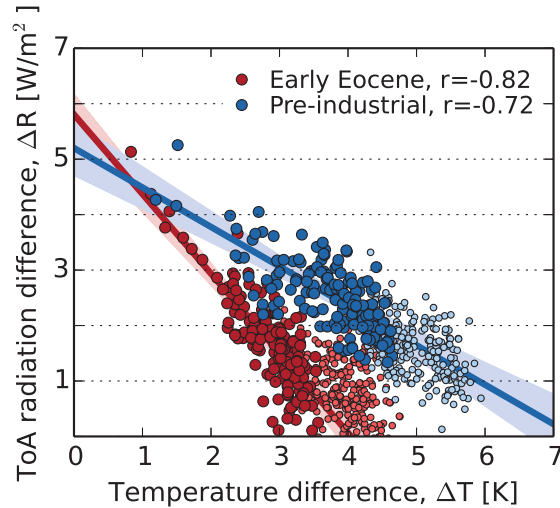


Figure 3.3: The evolution of differences in the ToA radiative flux between the forest world and the bright desert worlds with corresponding differences in near-surface temperature. Global annual-mean values are considered. Red points relate to the early Eocene climate and blue points refer to the pre-industrial climate. The first 150 years are shown as dark large points. The last 250 years are displayed as bright small points. The regression and the correlation coefficient, r , consider the first 150 years. The shaded areas refer to the 95% confidence interval for the regression lines.

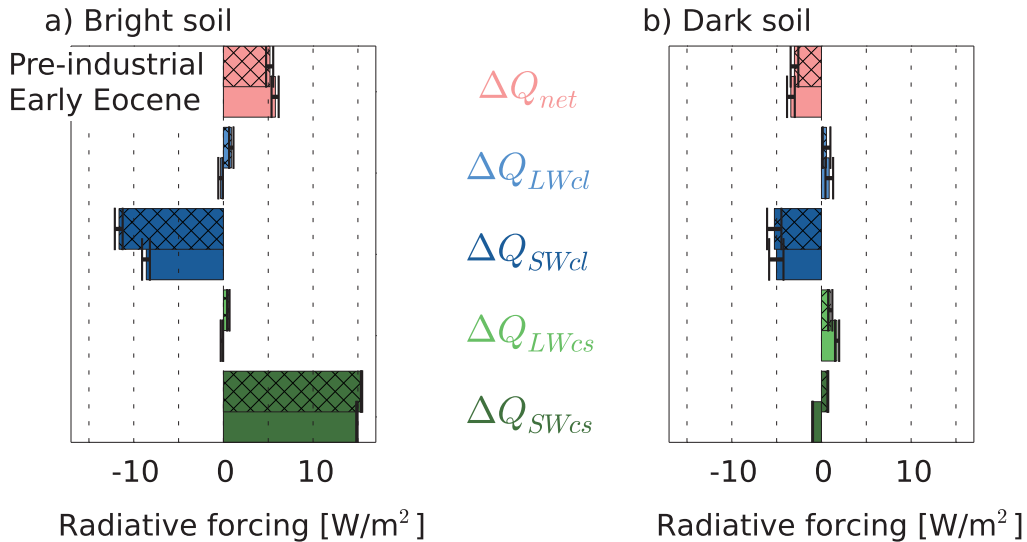


Figure 3.4: Net radiative forcing and its single components for the comparison of the forest world to the bright desert world (a) and for the comparison of the forest world to the dark desert world (b). The hatched and the plain bars show the radiative forcings for the pre-industrial climate and the early Eocene climate, respectively. The error bars refer to the 95% confidence interval.

decreases by 0.26 due to forest. The strong land surface albedo reduction confirms the pronounced short-wave clear-sky radiative forcing ΔQ_{SWcs} by forest.

The short-wave cloud radiative forcing, ΔQ_{SWcl} , counteracts the positive ΔQ_{SWcs} (Fig-

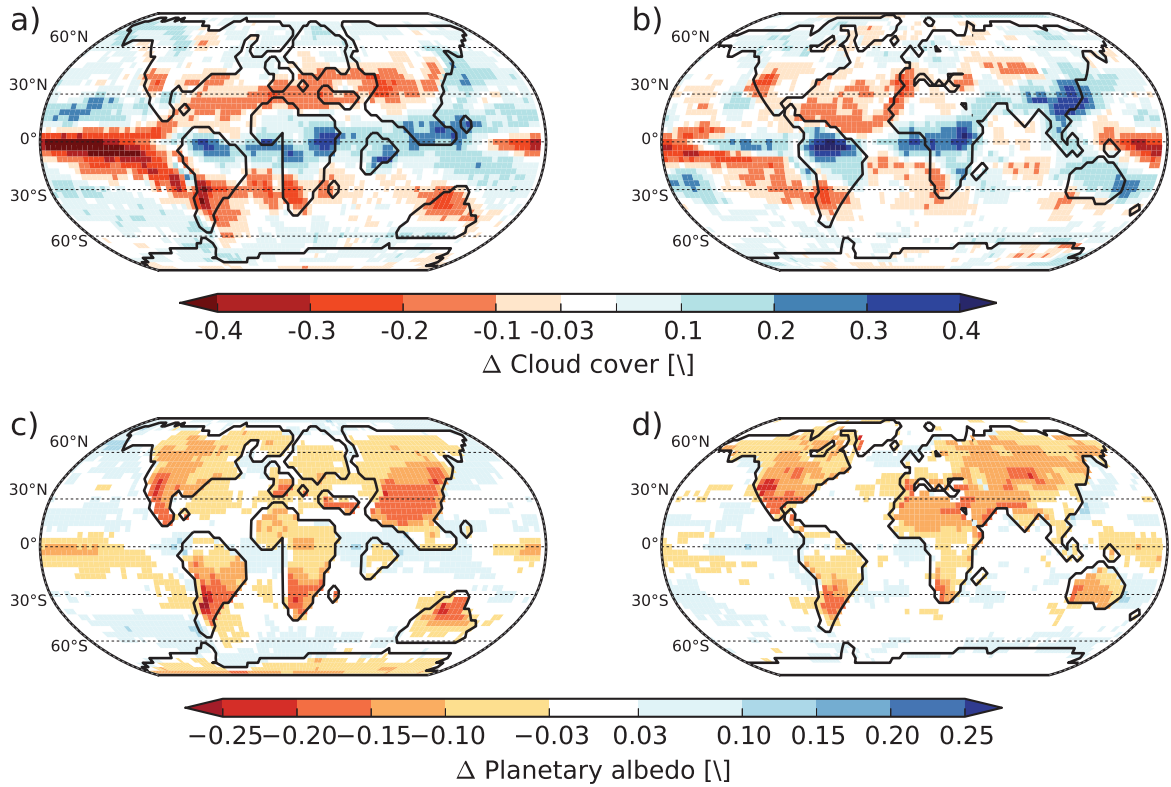


Figure 3.5: Difference in cloud cover and planetary albedo between the forest and the bright desert world averaged over the first year of the simulations. a) and c) show the differences for the early Eocene climate and b) and d) for the pre-industrial climate.

ure 3.4). ΔQ_{SWcl} reflects that forest increases the cloud cover over land by transpiring water and increasing evaporation. Figure 3.5 shows the difference in cloud cover and in planetary albedo between the forest world and the bright desert world in the first year of the simulations. Over the continents, the planetary albedo decreases due to the surface albedo reduction by forest. In regions where the cloud cover increases, however, the decrease in planetary albedo is weak. The clouds mask the surface albedo reduction by forest.

Feedbacks are differently strong in the early Eocene climate and the pre-industrial climate. The short-wave clear-sky feedback parameter, λ_{SWcs} , reflects the sea-ice/snow albedo feedback. In the pre-industrial climate, the ice-albedo feedback is pronounced. Hence, the warming by forest is amplified in the high latitudes (Figure 3.7 b). In the early Eocene climate, the ice-albedo feedback is weak because sea ice is almost absent in the early Eocene climate and snow occurs only seasonally. With a weak ice-albedo feedback, the warming by forest is zonally uniform (Figure 3.7 a).

The sum of the negative lapse-rate feedback and the positive water-vapour feedback is quantified in λ_{WV+LR} . λ_{WV+LR} is larger in the early Eocene climate than in the pre-industrial climate. The reason for the larger λ_{WV+LR} in the early Eocene climate could be a weaker lapse rate feedback than in the pre-industrial climate, a stronger water vapour feedback, or both. λ_{LWcl} is larger in the early Eocene than in the pre-industrial climate indicating a stronger water-vapour feedback by clouds. For present-day climate,

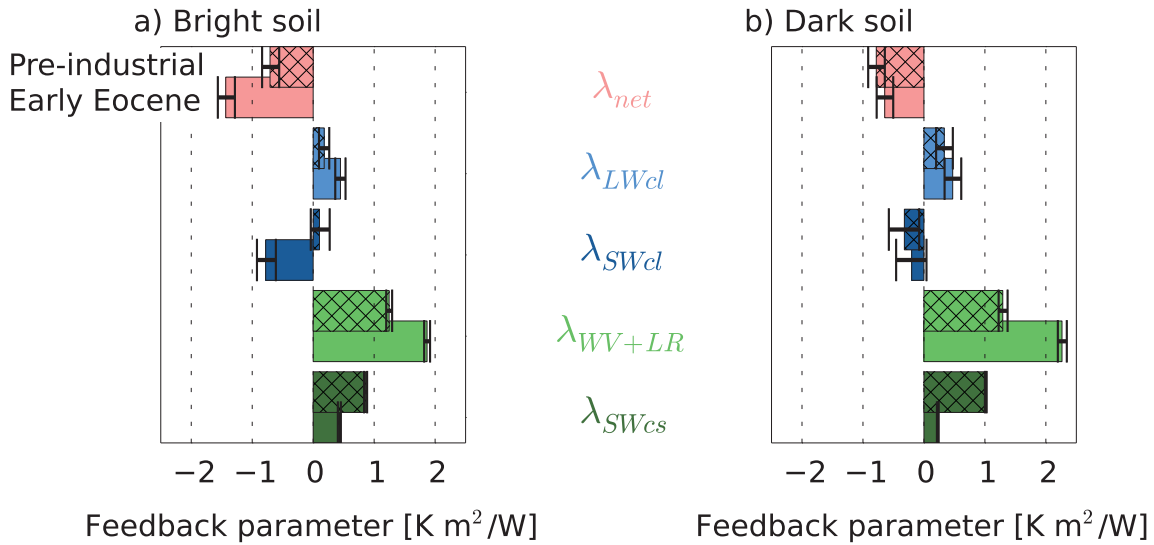


Figure 3.6: Net feedback parameter and its single components for the comparison of the forest world to the bright desert world (a) and for the comparison of the forest world to the dark desert world (b). The lapse-rate and water-vapour feedback, λ_{WV+LR} , is derived by subtracting the Planck feedback parameter from the long-wave clear-sky feedback parameter. The hatched and the plain bars show the feedback factors for the pre-industrial climate and the early Eocene climate, respectively. The error bars refer to the 95% confidence interval.

Meraner et al. (2013) suggest that the strength of the water-vapour feedback increases with warming. They attribute the stronger water-vapour feedback to the rise of the troposphere with warming.

The cloud albedo feedback, λ_{SWcl} , is negative in the early Eocene climate. In the pre-industrial climate, it is small. Despite the large uncertainty in the estimate of λ_{SWcl} , one can conclude that the cloud albedo feedback is stronger in the early Eocene climate than in the pre-industrial climate. I separate the difference in the short-wave cloud radiative flux between the forest world and the bright desert world, ΔR_{SWcl} , into ΔR_{SWcl} above the ocean and above the continents (similar to Andrews et al.

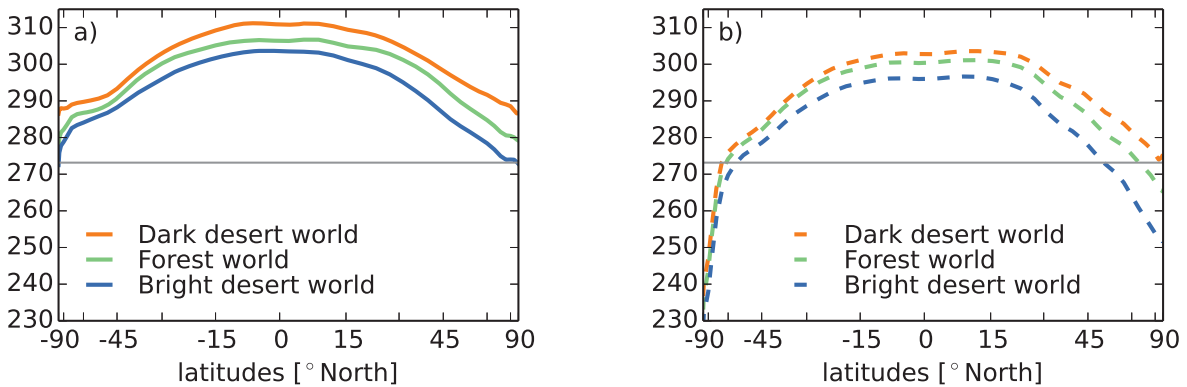


Figure 3.7: Zonal mean temperature in the dark desert world (orange line), the forest world (green line), and the bright desert world (blue line). The graphs show the average over the last 30 years of each early Eocene simulation (a) and of each pre-industrial simulation (b).

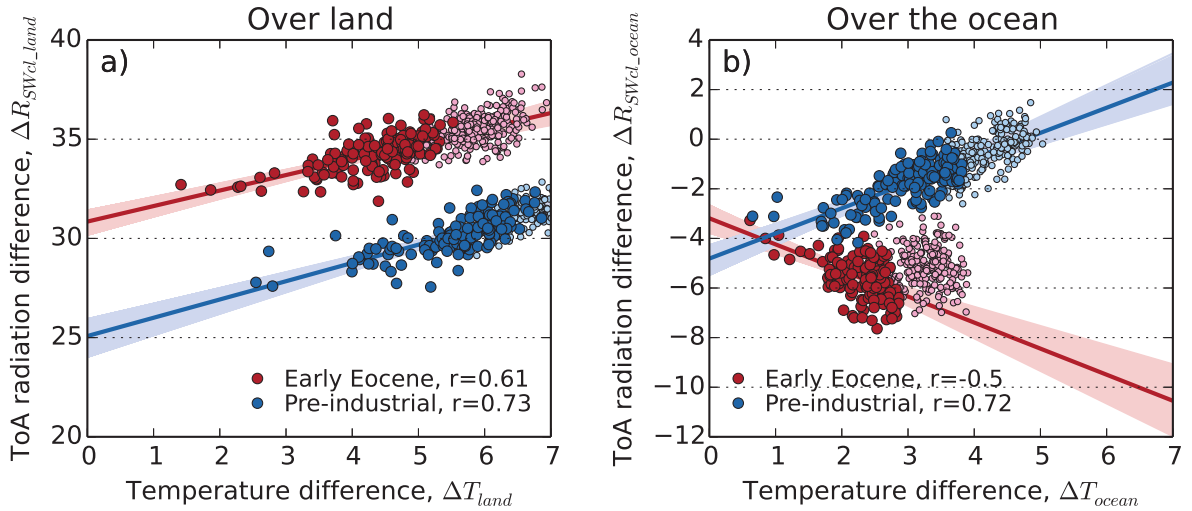


Figure 3.8: Evolution of the difference in ToA short-wave cloud radiative flux, R_{SWcl} , with differences in near-surface temperature between the forest world and the bright desert world. The evolution of R_{SWcl} is separated in the evolution above the land (a) and above the ocean (b). Global annual-mean values are considered. Red points relate to the early Eocene climate. Blue points refer to the pre-industrial climate. The first 150 years are shown as dark large points, the last 250 years are shown as bright small points. The regression and the correlation coefficient, r , consider the first 150 years. The shaded areas refer to the 95% confidence interval for the regression lines.

2012). Over land, the cloud feedback is nearly of the same strength in both climate states as the slope of the regression lines in Figure 3.8 a) illustrates. Over the ocean, the cloud albedo feedback is negative in the pre-industrial climate and positive in the early Eocene climate. Presumably, the different sign of the cloud albedo feedback results from a different structure in cloud cover changes with changes in sea-surface temperature in both climates.

The regression line for the first 150 years in Figure 3.8 b) does not match the last 250 years. Hence, the linear regression does not represent the evolution of ΔR_{SWcl} over the ocean well in the early Eocene climate. This behaviour indicates a time-dependent cloud feedback which is not captured by the regression approach. Senior and Mitchell (2000) also find a time-dependent cloud feedback parameter in present-day climate. They attribute the time-dependence to delayed cloud feedbacks over the Southern Ocean.

3.4.2 Afforestation of a dark desert world

The forest world is colder than the dark desert world by 4.2 K and 3.0 K at the end of the early Eocene and the pre-industrial simulations, respectively (Table 3.4). The cooling results from a negative radiative forcing of about 3 W/m^2 in both climate states (Figure 3.9). The main contributor to the net radiative forcing is the negative short-wave cloud radiative forcing, ΔQ_{SWcl} . Like in the bright-soil case, trees increase cloud cover leading to a higher planetary albedo in the forest world than in the dark

Table 3.4: Net radiative forcing by afforesting a dark desert world in the early Eocene climate and in the pre-industrial climate. Further, the net feedback parameter and the equilibrium temperature change are listed. The values are derived from the comparison of the respective forest world with the respective dark desert world. The 95% confidence interval is given. The transient temperature change refers to the temperature difference at the end of both simulations.

	Early Eocene	Pre-industrial
Radiative forcing [W/m ²]	-3.4 ± 0.4	-3.1 ± 0.5
Feedback parameter [W/m ² K]	-0.7 ± 0.1	-0.8 ± 0.2
Equilib. temperature change [K]	-5.3 ± 0.6	-3.8 ± 0.5
Transient temperature change [K]	-4.2	-3.0

desert world. The surface albedo change by trees is weak leading to a small short-wave clear-sky radiative forcing, ΔQ_{SWcs} .

Interestingly, ΔQ_{SWcs} is slightly negative in the early Eocene climate and slightly positive in the pre-industrial climate. In the first year of the early Eocene simulations, global mean land surface albedo value is 0.02 higher in the forest world than in the dark desert world, because trees have a slightly higher albedo value than the dark soils. The surface albedo increase causes a negative ΔQ_{SWcs} in the early Eocene climate. In the first year of the pre-industrial simulations, global mean land surface albedo value is 0.01 lower in the forest world than in the desert world because trees mask the snow cover in the high latitudes. The surface albedo reduction causes a positive ΔQ_{SWcs} in

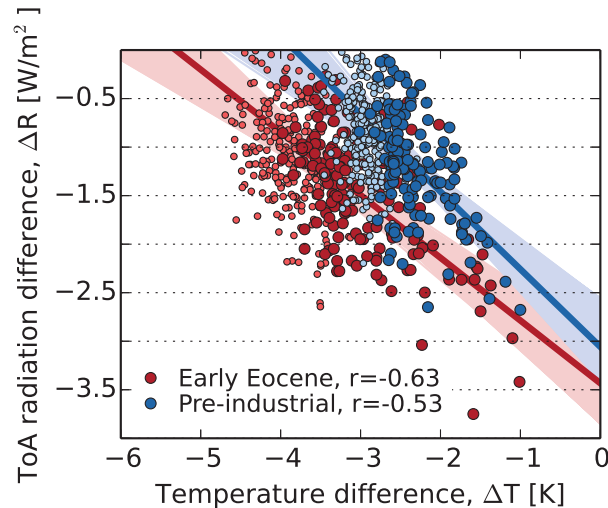


Figure 3.9: The evolution of differences in the ToA radiative flux between the forest world and the dark desert worlds with corresponding temperature differences. Global annual mean values are considered. The red points relate to the early Eocene climate and the blue points to the pre-industrial climate. The first 150 years are shown as dark large points, the last 250 years are shown as bright small points. The regression and the correlation coefficient, r , consider the first 150 years. The shaded areas refer to the 95% confidence interval for the regression lines.

the pre-industrial climate. The different sign of ΔQ_{SWcs} in both climates reveals that the lacking snow masking effect in the early Eocene climate leads to a different radiative forcing by forest than in the pre-industrial climate. On a global scale, however, the resulting difference in the radiative forcing is weak.

The ice-albedo feedback is weaker in the early Eocene than in the pre-industrial climate due to the absence of permanent sea ice and snow (Figure 3.6). With a weak ice-albedo feedback, the polar amplification is less pronounced in the early Eocene climate than in the pre-industrial climate (Figure 3.7). The lapse-rate/water-vapour and the cloud water-vapour feedback are stronger in the warm early Eocene climate than in the pre-industrial climate. The weaker sea-ice-albedo feedback in the early Eocene climate than in the pre-industrial climate is compensated by the stronger lapse-rate/water-vapour feedback and the stronger cloud water-vapour feedback. The net feedback is almost as strong in the early Eocene as in the pre-industrial climate (Table 3.4).

3.5 Conclusion

I estimate the impact of vegetation on the warm, nearly ice-free early Eocene climate and on the interglacial pre-industrial climate. For Eocene and for pre-industrial conditions respectively, I compare a world with continents completely covered by forests with a world either with bright deserts or with dark deserts only. Bright deserts are characterised by a soil albedo of 0.4 similar to the surface albedo in some regions of the Sahara. Dark deserts have a soil albedo of 0.1 similar to the albedo of volcanic rocks. Based on the comparison of the forest world with the desert worlds, I assess radiative forcing by forest and subsequent feedbacks using the approaches by Gregory et al. (2004) and Andrews et al. (2012).

Forest induces a radiative forcing of similar strength in the early Eocene climate and in the pre-industrial climate. Relative to the bright desert world, forest induces a positive radiative forcing by reducing the surface albedo. Further, forest causes a negative radiative forcing by extending the cloud cover. The cloud forcing partly counteracts the forcing due to surface albedo reduction. The net radiative forcing is positive leading to a warming by forest. Relative to the dark desert world, forest changes surface albedo just slightly. The resulting radiative forcing by surface albedo changes is weak. The negative cloud radiative forcing is the major forcing leading to a cooling.

The feedbacks that follow the radiative forcing differ in both climate states. In the warm early Eocene climate, the lapse-rate/water-vapour feedback is stronger than in the colder pre-industrial climate. Further, the ice-albedo feedback is weak in the early Eocene climate, because sea ice occurs only rarely and snow cover is much smaller than in the pre-industrial climate. With a weak ice-albedo feedback, also polar amplification is weak in the early Eocene climate.

In this study, I assume the same forest taxa in the early Eocene as in the pre-industrial climate. During the early Eocene, however, different forest taxa existed than today. Considering early Eocene forest taxa might lead to additional differences in the impact of vegetation on the early Eocene and on the pre-industrial climate.

This study highlights that the impact of vegetation on climate depends on the climate state. Feedback between vegetation and climate, however, are neglected so far. Vegetation-climate feedbacks play an important role in present-day arid and cold regions. For instance, in the Sahel, precipitation limits vegetation growth. At the same time, vegetation increases precipitation by reducing the surface albedo. This interdependence of vegetation and precipitation is suggested to allow multiple vegetation states in the Sahel (e.g. Charney 1975 and Claussen 1998). In the next chapter, I will investigate whether vegetation-climate feedbacks depend on the climate state.

Chapter 4

The Stability of the Vegetation-Atmosphere System in the Early Eocene Climate

The previous chapter illustrated that vegetation affects the early Eocene climate differently than the pre-industrial climate because feedbacks are specific in each of both climates. Feedbacks between vegetation and climate, however, were neglected in the previous chapter. Vegetation-climate feedbacks are of special interest because they are suggested to cause multiple stable states of the vegetation-atmosphere system. Here, I focus on climate-vegetation feedbacks. To investigate whether the stability of the vegetation-atmosphere system depends on the climate state, I evaluate multiple vegetation-atmosphere states in the pre-industrial climate and in the early Eocene climate.

4.1 Introduction

Vegetation and climate interact with each other leading to feedbacks between them. These feedbacks are suggested to cause multiple stable vegetation-atmosphere states. For instance in arid regions, precipitation rate determines plant growth. In turn, vegetation increases precipitation. Conceptual models suggest that this vegetation-climate feedback may cause two stable states in arid regions (Brovkin et al. 1998; Wang and Eltahir 2000): Firstly, an arid state allows only little vegetation which maintains the dry climate. Secondly, a humid state allows abundant vegetation which preserves the humid climate.

Climate models indicate that multiple stable states exist in the present-day vegetation-atmosphere system. Using an interactive atmosphere-biome model, Claussen (1997) simulates the pre-industrial vegetation cover together with climate. At the beginning of the simulation, he either assume bare soil or dense forest on all continents. Starting from bare soil on all continents, the same vegetation cover establishes as we observe today. Starting from a dense forest, precipitation is sufficient to maintain vegetation in large parts of the Sahara region. Hence, a significantly smaller Sahara desert establishes than in the simulation started from bare soil. Several modelling studies confirm that the Saharan vegetation cover might be bistable (Claussen 1997, 1998; Brovkin et al. 1998; Wang and Eltahir 2000; Zeng and Neelin 2000). Further multiple vegetation-atmosphere states are suggested in the Amazon region (Oyama and Nobre 2003), in

the Asian monsoon region (Claussen 1998), and in the northern high latitudes (Dekker et al. 2010).

Climates of the past offer the opportunity to analyse the stability of the vegetation-atmosphere system for boundary conditions that differ from the present-day boundary conditions. For instance, Kubatzki and Claussen (1998) evaluate the stability of the vegetation-atmosphere system in the Last Glacial Maximum (LGM) climate (21,000 years before present) which was much colder than today's climate (Sarnthein et al. 2003 and Gersonde et al. 2005). Similar to the present climate, two stable vegetation-atmosphere states are suggested to exist in the Sahara in the LGM climate (Kubatzki and Claussen 1998). Going further back in time, climate has often been much warmer than today (Frakes 1979). The stability of the vegetation-atmosphere system in an extremely warm climate has not been analysed so far.

During the early Eocene, such an extremely warm climate prevailed due to a high atmospheric CO₂ concentration between 300 ppm and 2000 ppm (Beerling and Royer 2011) together with a specific distribution of continents (cf. Chapter 1). Especially in the high latitudes, temperatures were much higher than today and rarely dropped below the freezing point (Hutchison 1982; Markwick 1994; Ivany et al. 2008). Hence, perennial ice sheets and sea ice were absent. Further, the vegetation cover differed significantly from the present one. The warm climate caused a dense vegetation cover in almost all regions (Willis and McElwain (2002)). I evaluate the stability of the vegetation-atmosphere system in the early Eocene climate and in the pre-industrial climate. The comparison of the results for both climates addresses the question: Does the stability of the vegetation-atmosphere system depend on the climate state? Answering this question enhances the knowledge about the processes that cause, or prevent, instabilities in the vegetation-atmosphere system.

Using the earth system model MPI-ESM, I simulate the early Eocene climate and the pre-industrial climate interactively with the respective vegetation cover. Thereby, I assume two different initial vegetation covers. Either a dense forest or bare soil covers all continents at the beginning of the simulations. After 1000 years, the atmosphere and the biosphere reach equilibrium. I investigate whether multiple stable vegetation-atmosphere states evolve for the two initial vegetation covers.

In order to identify the vegetation-climate feedbacks that cause, or prevent, multiple vegetation-atmosphere states, I perform the sensitivity study two times. All soils have either a similar albedo as vegetation or a much higher albedo than vegetation. In the first case, changes in the vegetation cover modify the moisture flux and the heat flux between the surface and the atmosphere. Radiative fluxes, however, remain unaffected. Hence, vegetation-climate feedbacks are mainly related to hydrological changes. In the second case, changes in the vegetation cover alter fluxes of moisture and of heat as well as radiative fluxes between the surface and the atmosphere. Hence, vegetation-climate feedbacks are related to hydrological changes and to albedo changes.

The atmospheric carbon dioxide (CO₂) concentration is fixed to 280 ppm and 560 ppm in the pre-industrial simulations and in the early Eocene simulations, respectively. The atmospheric CO₂ concentration remains constant even though the vegetation cover changes. In other words, I consider biogeophysical vegetation-climate feedbacks and neglect biogeochemical feedbacks.

Our model assumes present-day plant species to simulate the early Eocene vegetation cover. During the early Eocene, however, plant species differed from today's plant species (Wolfe 1985; Willis and McElwain 2002). Here, I neglect that the plant species in the model does not represent the early Eocene plant species. The emerging limitations in the simulated vegetation cover are discussed in Chapter 5.

In the following, I present the vegetation-climate feedbacks that are suggested to cause multiple stable vegetation-atmosphere states in present-day climate. I will refer to the introduced vegetation-climate feedbacks when I discuss the results. The next section presents the experiment that was performed for this study. After that, I evaluate and compare multiple vegetation-atmosphere states in the early Eocene climate and in the pre-industrial climate. Thereby, I start with the results for the dark soil simulations followed by the results for the bright soil simulations. Finally, I summarise the results and draw conclusions about the stability of the vegetation-atmosphere system in different climates.

4.1.1 Positive climate-vegetation feedbacks in present-day climate

Previous studies identify the vegetation-climate feedbacks that may cause multiple stable vegetation-atmosphere states in the Sahara, in the Amazon region, and in the northern high latitudes. These vegetation-climate feedbacks are regionally specific. Figure 4.1 gives an overview of the vegetation-climate feedbacks in respective regions. I introduce these feedbacks in the following and refer to them in the discussion of my results.

Charney (1975) and Charney et al. (1977) suggest that hot deserts preserve their desert state due to their high surface albedo. They argue that a bright desert reflects more solar radiation than its surrounding. Further, the desert's surface is warmer and fewer clouds appear over the desert than over the vegetated surrounding (Figure 4.1 a). These characteristics of a desert lead to a loss of energy above the desert. Above the vegetated surrounding, however, the atmosphere gains energy. The contrast in energy leads to colder air above the desert than above the vegetated surrounding. To counteract the temperature gradient, air subsides over the desert. The subsidence prevents convection leading to a weak precipitation in the desert. Vegetation can not establish in the dry climate and the surface albedo remains high. This feedback is suggested to cause multiple vegetation-atmosphere states in the Sahel. Assuming different initial vegetation covers, Claussen (1997) simulates climate and vegetation interactively. When the initial vegetation cover is a desert on all continents, the Charney effect causes subsidence over Northern Africa leading to weak precipitation. A large Sahara establishes with little vegetation in the Sahel. When the initial vegetation cover is a dense forest on all continents, the surface albedo is low in Northern Africa leading to weak subsidence and strong precipitation over the Sahel. Hence, vegetation remains in the Sahel.

Oyama and Nobre (2003) suggest that a *hydrological feedback* between vegetation and precipitation causes multiple stable vegetation-atmosphere states in the Amazon region (Figure 4.1 b). In this region, water recycling is a major process leading to precipitation. Observations reveal that 40% - 60% of the precipitated water originates from

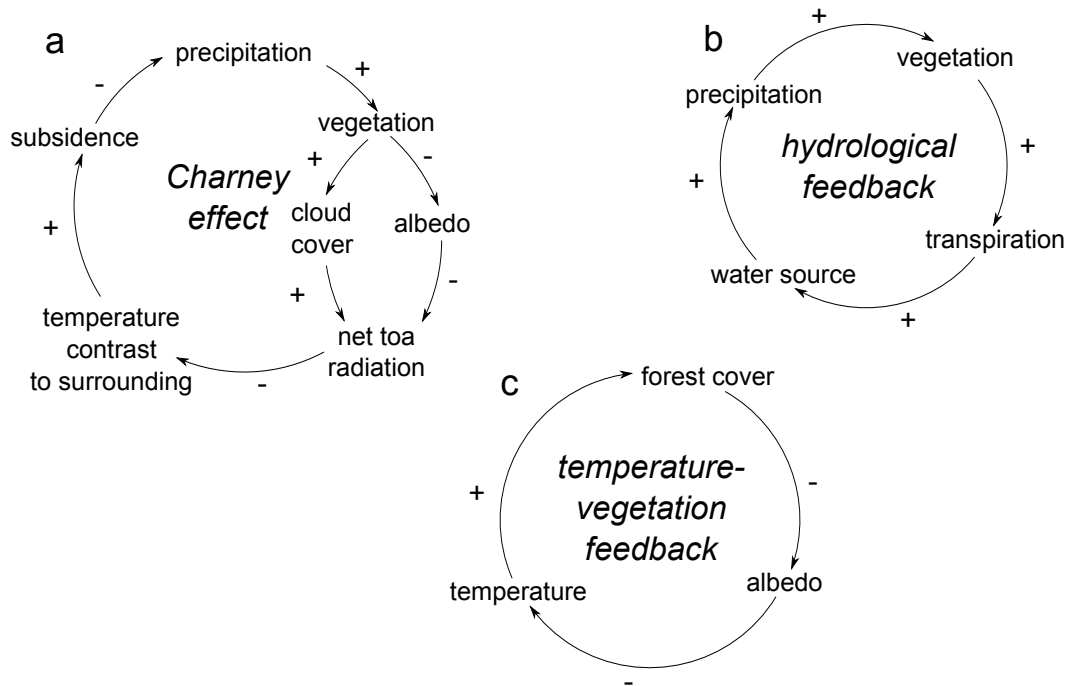


Figure 4.1: Feedback mechanisms that are suggested to cause multiple stable vegetation-atmosphere states in the Sahel (a), in the Amazon (b), and in the boreal region (c). Signs indicate the relationship between two variables connect with the respective arrow. Assuming the arrow connects X and Y, a positive sign indicates that an increase in X causes an increase in Y. A negative sign implies that an increase in X results in a decrease in Y.

evaporation and transpiration in the Amazon region (Salati and Vose 1984). Hence, vegetation determines precipitation. Oyama and Nobre (2003) simulate global climate and vegetation cover. When the simulation starts from forests on all continents, water recycling is strong in the Amazon region and a dense forest remains. When the simulation starts from deserts on all continents, water recycling is weak in the Amazon region leading small precipitation rates. Vegetation cannot establish and the desert state persists in the Amazon region.

In the boreal region, temperature and vegetation are interdependent. On the one hand, temperature limits plant growth. On the other hand, forest warms the high latitudes because forest masks the snow cover leading to a reduced surface albedo (Figure 4.1 c). In a conceptual model, Brovkin et al. (2003) show that this *temperature-vegetation feedback* may cause two stable vegetation-atmosphere states in the boreal region. High latitude forest leads a high temperature that maintains forest growth. Tundra vegetation leads to a low temperature that prohibits forest growth. Tundra vegetation persists in the cold climate. Using an earth system model of intermediate complexity, Dekker et al. (2010) simulate these two vegetation states in the boreal region. Starting from minimum biomass, a cold climate establishes in the high latitudes. Biomass does not build up in this cold climate. Starting from maximum biomass, temperature remains high enough to maintain large parts of the biomass.

4.2 Experiment

I use the Max Planck Institute for Meteorology Earth System Model (MPI-ESM), which consists of the atmospheric general circulation model (GCM) ECHAM6 (Stevens et al. 2013), the Max Planck Institute Ocean Model (MPIOM) (Jungclaus et al. 2013), the land surface scheme JSBACH (Reick et al. 2013), and the ocean biogeochemistry model HAMOCC (Ilyina et al. 2013). ECHAM6 runs with 31 levels in the vertical and in a horizontal resolution of T31, which corresponds to approximately 3.75° . The ocean grid has a horizontal resolution of about 3° and 40 levels in depth. JSBACH includes a dynamic vegetation module based on a tiling approach (Brovkin et al. 2009). Vegetation is represented by the eight Plant Functional Types (PFTs) listed in Table 2.1. MPI-ESM is introduced in more detail in Chapter 2.

In the previous chapter, I simulated a forest world and a desert world for the early Eocene climate and the pre-industrial climate. In the forest world and in the desert world, a dense forest and bare soil cover all ice-free continents. The simulations ran for 400 years. I performed the forest world simulations and the desert world simulations with dark soil (soil albedo of 0.1) and with bright soil (soil albedo of 0.4). This approach revealed four different states of the early Eocene climate and of the pre-industrial climate: a forest world with dark soil, a desert world with dark soil, a forest world with bright soil, and a desert world with bright soil.

In this chapter, I extend these simulations for a further 1000 years. During the extended simulations, vegetation establishes, migrates, and retreats dynamically. Table 4.1 gives an overview of all simulations. The name of each simulation refers to the initial vegetation-atmosphere state (**F**orest world and **D**esert world), the soil albedo (**D**ark soil and **B**right soil), and the boundary conditions (**E**arly Eocene and **P**re-industrial).

Table 4.1: Simulations included in the experiment. The same set of simulations is performed for the early Eocene climate and for the pre-industrial climate. Detailed information about the different boundary conditions are given in Chapter 2. For both climates, the simulations differ concerning the initial vegetation-atmosphere state and the soil albedo. The initial vegetation-atmosphere states are the forest worlds and desert worlds introduced in Chapter 3. Soils are either bright or dark with a homogeneous soil albedo of 0.4 or 0.1, respectively.

Exp ID	Initial state	Soils	Time slice
FD_P	F orest world	D ark	P re-industrial
DD_P	D esert world	D ark	
FB_P	F orest world	B right	
DB_P	D esert world	B right	
FD_E	F orest world	D ark	E arly Eocene
DD_E	D esert world	D ark	
FB_E	F orest world	B right	
DB_E	D esert world	B right	

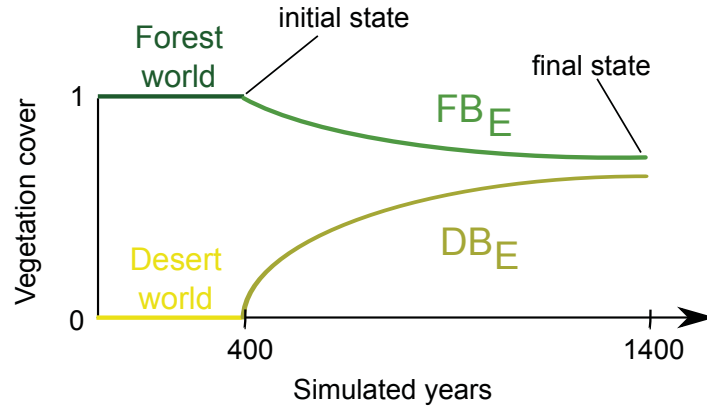


Figure 4.2: Idealised development of the vegetation cover in the FB_E simulation and in the DB_E simulation. Starting from a forest world and from a desert world, vegetation cover evolves according to climate. I investigate whether the vegetation cover reaches the same state in both simulations. Therefore, I analyse the last 30 years for the simulations (final state) and the last 30 years for the forest world and desert world simulations (initial state).

As an example, Figure 4.2 shows the idealised development of the vegetation cover in the FB_E and DB_E simulation. The simulations start from the forest world and from the desert world, respectively. I analyse whether the vegetation cover reaches the same state in both simulations. For this analysis, I compare the average over the last 30 years of the simulations. I refer to this average as the *final state*. To identify the mechanism that causes potential differences in the vegetation cover between both simulations, I analyse the *initial state*. The initial state is the average over the last 30 years of the forest world simulation and of the desert world simulation.

4.3 Results and Discussion

I investigate the stability of the vegetation-atmosphere system in the early Eocene climate and in the pre-industrial climate. Thereby, I assume either dark soil or bright soil on all continents. Firstly, I present the results for the dark-soil case. Soils and vegetation have a similar albedo in this case. Hence, vegetation mainly influences the water flux between the surface and the atmosphere. Secondly, I show the results for the bright-soil case. Bright soil has a much higher albedo than vegetation. Hence, vegetation affects the energy balance at the surface and the water fluxes. The early Eocene vegetation cover is presented only to a small extent in this chapter. A more detailed description of the simulated early Eocene vegetation cover and a comparison to vegetation reconstructions follow in Chapter 5.

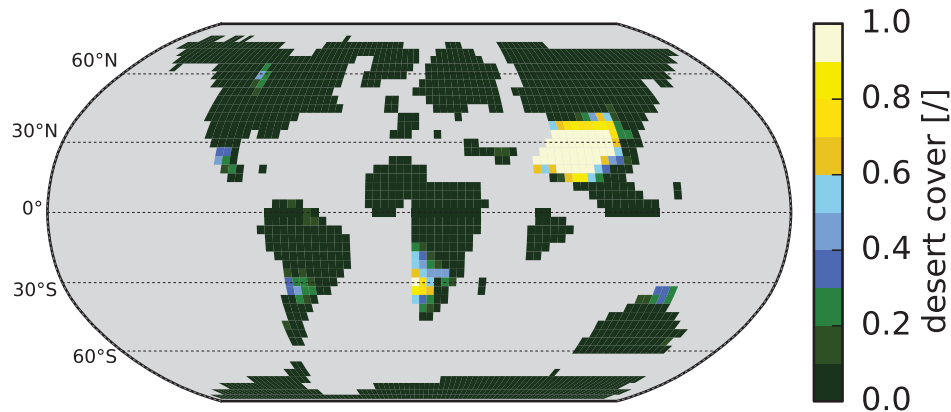


Figure 4.3: Desert cover in the DD_E simulation. The average over the last 30 years of the simulation is shown. Green indicates a minimum desert cover. Bluish colours refer to open vegetation. Yellow colours mark desert regions.

4.3.1 Dark soil: hydrological feedbacks cause multiple vegetation-atmosphere states

Early Eocene climate

The warm and humid early Eocene climate allows a dense vegetation cover in almost all regions. Only in Central Asia and in southern Africa, deserts establish in the DD_E simulation (Figure 4.3). Subtropical semi-deserts evolve in South America, North America, and Australia. In these arid and semi-arid regions, vegetation cover reaches a different state when the simulation starts from a forest world instead of a desert world (Figure 4.4).

In the semi-desert in western North America, the desert cover is larger by 0.43 in the FD_E simulation than in the DD_E simulation (Figure 4.5 c). Precipitation is smaller by 0.52 mm/day (70%). In the semi-desert in southern South America, desert cover is larger by 0.19 and precipitation is smaller by 0.5 mm/day (43%) in the FD_E simulation than in the DD_E simulation (Figure 4.5 d). These results are counterintuitive because starting from a forest world leads to less vegetation than starting from a desert world. Later I will show that a global mechanism superposes the regional vegetation-precipitation feedbacks in western North America and southern South America leading to the surprising multiple vegetation states in these regions.

In southern Africa, desert cover is smaller by 0.12 at the end of the FD_E simulation than at the end of the DD_E simulation. A trend of -0.04 and 0.07 per 100 years remains in the FD_E simulation and in the DD_E simulation, respectively (Figure 4.5 b). Considering the remaining trends, the difference in vegetation cover is not robust.

In Central Asia, the differences in the vegetation cover are most pronounced. At the southern edge of the desert more grass and trees remain in the FD_E simulation than in the DD_E simulation. At the beginning of the FD_E simulation, the dense forest transpires 1.35 mm/day leading to an evapotranspiration of 1.7 mm/day in Central

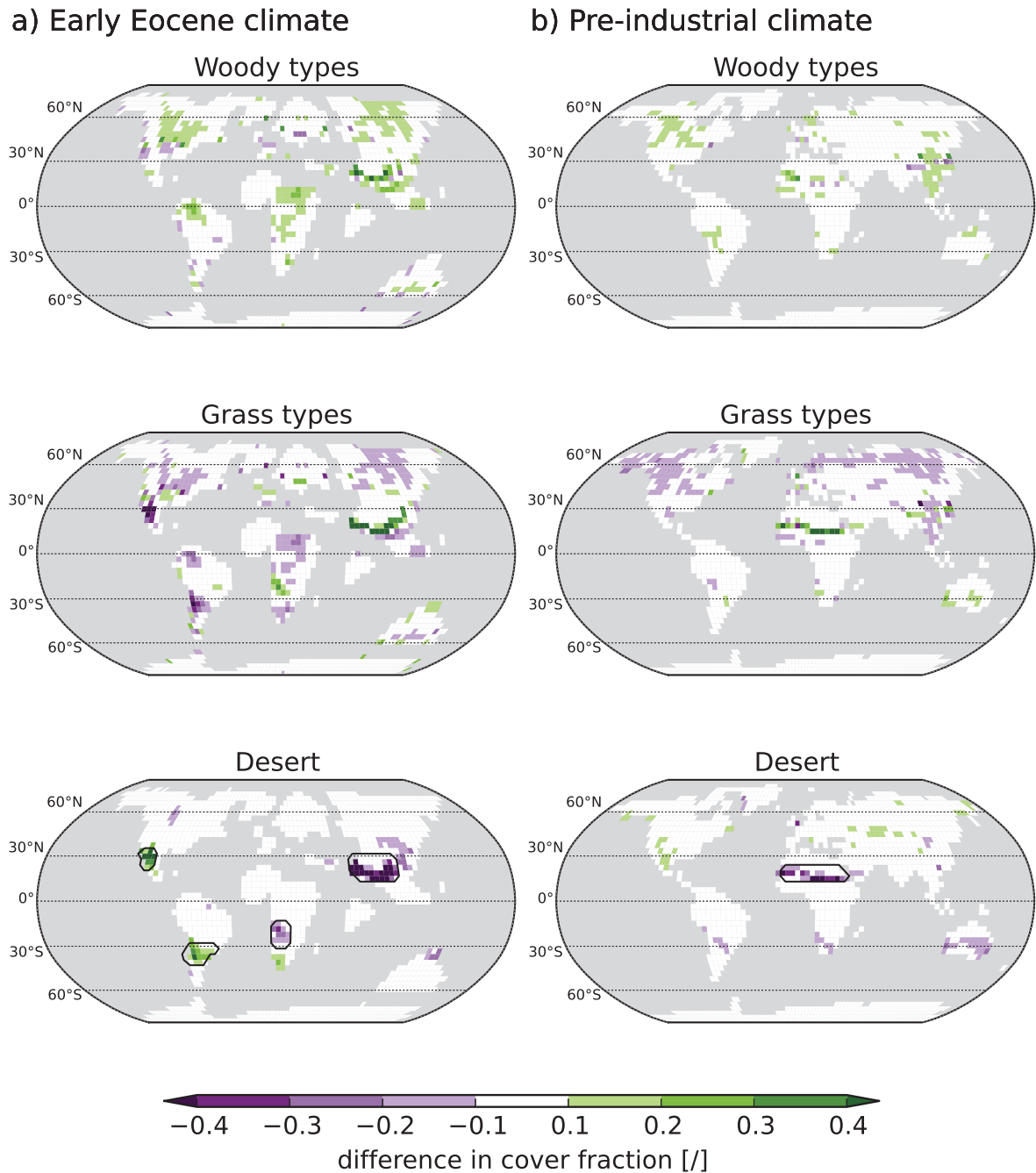


Figure 4.4: Dark soil: Differences in vegetation cover between the simulations that start from a forest world and from a desert world. Shown are differences for the early Eocene climate ($FD_E - DD_E$) (a) and for the pre-industrial climate ($FD_P - DD_P$) (b). Mapped differences are significant on a 95% confidence interval. Woody types include all trees and shrubs. Grass types refer to C_4 grass and to C_3 grass. Green colours indicate a higher cover fraction in the FD than in the DD simulation. Purple colours refer to a smaller cover fraction in the FD simulation. Black contour lines mark regions which are analysed in more detail in Figure 4.5 and Figure 4.9.

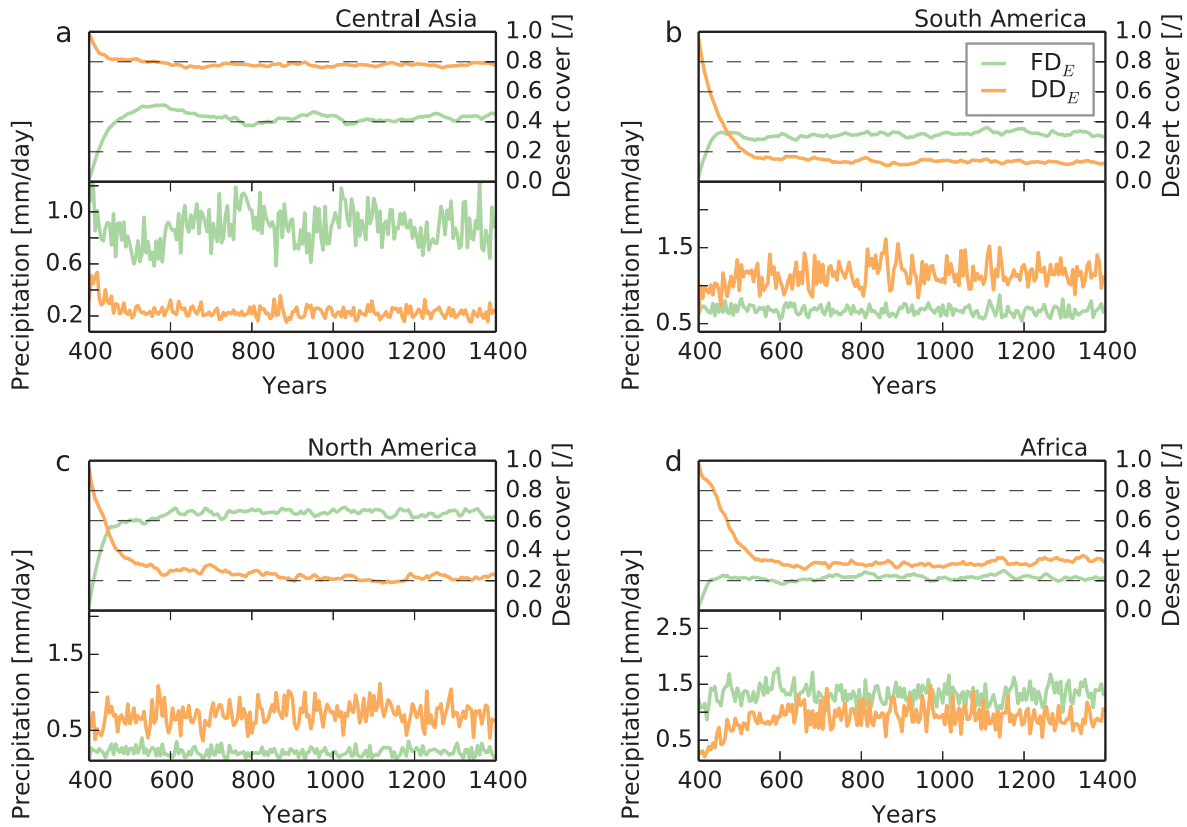


Figure 4.5: Time series of desert cover and precipitation in selected regions in Central Asia (a), South America (b), North America (c), and Africa (d) in the FD_E simulation (green line) and in the DD_E simulation (orange line). The regions are marked in Figure 4.4. Both time series show five-year mean values.

Asia (the considered region is marked in Figure 4.4). Precipitation is 1.8 mm/day in this region. During the FD_E simulation, precipitation is sufficient to maintain a large part of the vegetation cover (Figure 4.5 a). The remaining vegetation preserves high transpiration rates. The resulting high precipitation again sustains plant growth. By the end of the FD_E simulation, desert cover is 0.43 and precipitation is 0.82 mm/day in Central Asia.

At the beginning of the DD_E simulation, evapotranspiration in Central Asia is ten times weaker than at the beginning of the FD_E simulation because vegetation is absent. The precipitation rate is six times smaller (Figure 4.5 a). Starting from this dry climate, only little vegetation establishes during the DD_E simulation. With sparse vegetation, the climate remains dry in Central Asia. At the end of the DD_E simulation, desert cover reaches 0.79 in Central Asia and precipitation is 0.22 mm/day.

The precipitation difference in Central Asia between the FD_E simulation and the DD_E simulation is most pronounced in summer when the Asian monsoon is strong. The seasonal precipitation difference indicates that vegetation enhances the Asian monsoon. In the sum, I suggest the following feedback: Vegetation increases water recycling and enhances the Asian monsoon relative to bare soil. The resulting increase in precipitation sustains a dense vegetation cover.

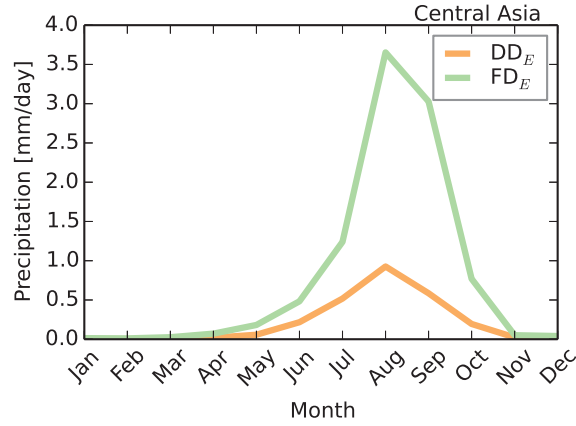


Figure 4.6: Annual cycle of precipitation in early Eocene Central Asia. The respective region is marked in Figure 4.4. Lines refer to the FD_E simulation (green) and the DD_E simulation (orange). The average over the last 30 years of each simulation is considered.

For present-day Asia, Meehl (1994) suggests a similar feedback but he relates soil moisture to the Asian monsoon. He shows that low soil moisture leads to a weak Asian monsoon and weak precipitation. Soil moisture remains low in this case. A high soil moisture, however, acts as an additional moisture source leading to a stronger Asian monsoon than with a low soil moisture. The resulting stronger precipitation sustains the high soil moisture. The similarity between the soil moisture-precipitation feedback and the vegetation-precipitation feedback that I find implies that the Asian monsoon is sensitive to additional water sources in general. Both, soil moisture and vegetation can be the additional water source.

I investigate the impact of vegetation on the large scale atmospheric circulation in further detail. Similar to Claussen (1997), I analyse the velocity potential at 200 hPa which reflects large scale convection and subsidence in the tropics. The velocity potential is derived from the wind field. The separation of the horizontal wind, \mathbf{V} , in the rotational component, \mathbf{V}_Ψ , and in the divergent component, \mathbf{V}_χ , yields

$$\mathbf{V} = \mathbf{V}_\Psi + \mathbf{V}_\chi. \quad (4.1)$$

The divergent part of the wind is the gradient of the velocity potential, χ ,

$$\nabla\chi = \mathbf{V}_\chi. \quad (4.2)$$

The gradient of the velocity potential is directed towards the strongest increase in the velocity potential field. Hence, Equation 4.2 indicates that the divergent part of the wind is directed along the strongest increase in the velocity potential. This relation implies that air flows from the centre of negative velocity potential to the centre of positive velocity potential. Therefore, air diverges in the centre of negative velocity potential. Below the divergence, air rises indicating convection. Air converges in the centre of positive velocity potential. Below the convergence, air subsides indicating weak convection.

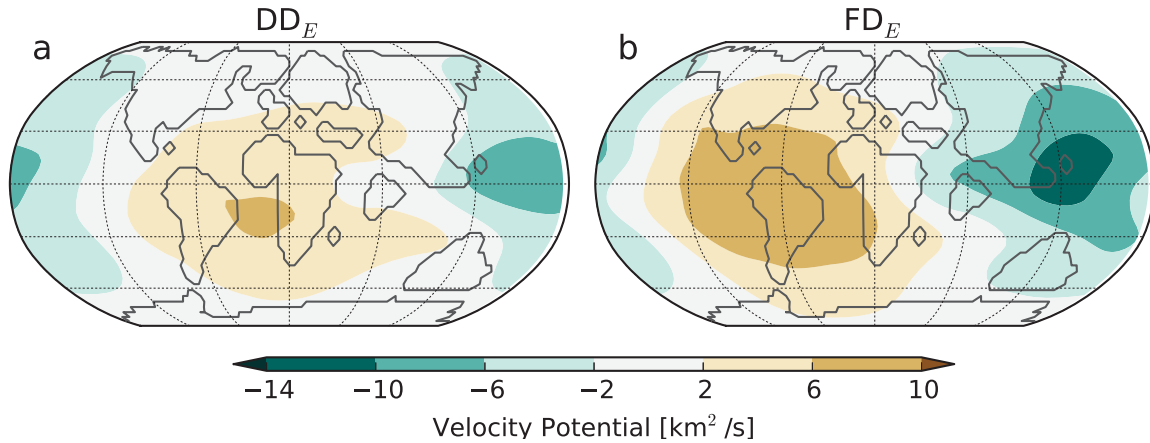


Figure 4.7: Velocity potential at 200 hPa in the FD_E simulation (a) and in the DD_E simulation (b). The 30-year average for the Asian monsoon season (July, August, and September) is shown. Brownish colours refer to a positive velocity potential. Air converges in regions of positive velocity potential and air subsides below. Greenish colours refer to a negative velocity potential. Air diverges in regions of negative velocity potential and air rises below.

Figure 4.7 a) shows the map of global velocity potential at 200 hPa at the end of the DD_E simulation. The mean over the monsoon season (July, August, and September) is considered. The centre of positive velocity potential over the tropical Atlantic Ocean refers to subsidence over this region. The centre of negative velocity potential over the western Pacific Ocean indicates strong convection over this region. Over Central Asia, velocity potential is around zero in the DD_E simulation. The small velocity potential implies that convection is weak over Central Asia. In the FD_E simulation, the centre of negative velocity potential is stronger and shifted relative to the DD_E simulation (Figure 4.7 b). The Asian desert is smaller in the FD_E simulation leading to stronger convection over Asia. Hence, vegetation in Central Asia intensifies and shifts the centre of negative velocity potential relative to the DD_E simulation.

The intensification and shift in the velocity potential in the FD_E simulation goes beyond the western Pacific Ocean and Central Asia. On a global scale, the velocity potential pattern intensifies and shifts westwards relative to the DD_E simulation. The difference in the velocity potential pattern between both simulations refers to a different global atmospheric circulation. Precipitation and temperature patterns evolve differently in FD_E simulation than in the DD_E simulation due to the different global atmospheric circulation (Figure 4.8).

The two different climate states lead to two different global vegetation states. At the west coast of the American continents, precipitation is weaker in the FD_E simulation than in the DD_E simulation. Hence, the semi-arid regions in western North America and southern South America are larger in the FD_E simulation. In other words, the multiple vegetation-atmosphere states in these semi-arid regions are driven by the multiple vegetation-atmosphere state in Central Asia. This result indicates a global connection of several multiple stable vegetation states in the early Eocene climate. Such a connection has, so far, not been found in present-day climate. Claussen (1997) simulates a shift in the atmospheric circulation with different vegetation states in the

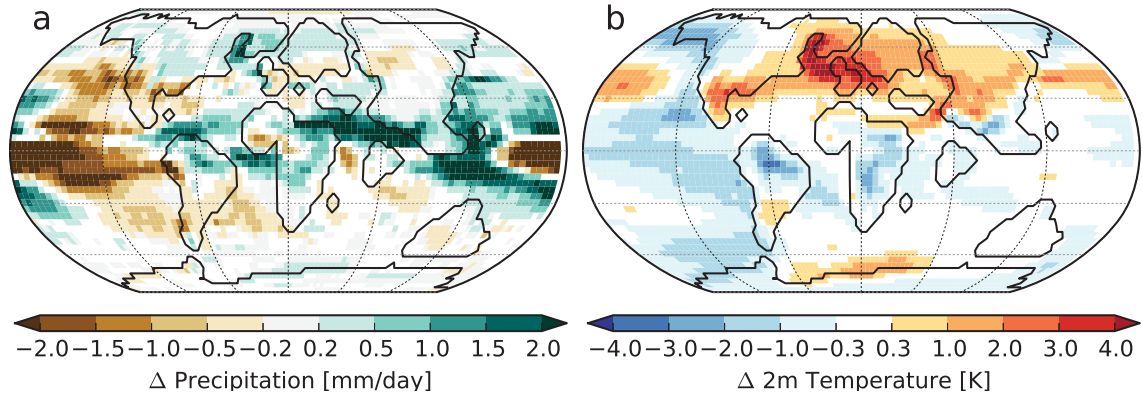


Figure 4.8: Precipitation differences (a) and temperature differences (b) between the FD_E simulation and the DD_E simulation. The average over the last 30 years of the respective simulation is considered. Depicted differences are significant on a 95% confidence interval.

Sahara. The shift in the atmospheric circulation affects the vegetation in the Sahara only.

The question remains which mechanism connects the multiple stable vegetation states in Central Asia and on the American continents. I assume that the hydrological effect of vegetation in Central Asia intensifies the Walker circulation. In present-day climate, the Walker circulation describes the zonal atmospheric circulation over the subtropical Pacific Ocean. Together with the zonal ocean circulation in the Pacific Ocean, the Walker circulation forms the El Niño-Southern Oscillation (ENSO). ENSO is an important characteristic of present-day global climate.

The present-day Walker circulation is driven by the easterly trade winds over the Pacific Ocean which transports ocean water westwards. At the eastern side of the Pacific Ocean, the trade winds transport ocean water away from the coast. Upwelling compensates for the divergence of water. The upwelling water has a low temperature leading to low Sea Surface Temperatures (SSTs) at the eastern side of the Pacific Ocean. The contrast in SST between the eastern side and the western side of the Pacific Ocean induces an atmospheric circulation. Air rises over the warm water at the western side of the Pacific Ocean. Air descends over the cold water at the eastern side of the Pacific Ocean.

In the early Eocene simulation, the Walker circulation establishes. The velocity potential illustrates the bipolar pattern of rising air over the western Pacific Ocean and subsiding air over the eastern Pacific Ocean (Figure 4.7). The bipolar pattern, however, differs for the FD_E simulation and the DD_E simulation. Strong convection over Central Asia intensifies the convection branch of the Walker circulation in the FD_E simulation relative to the DD_E simulation (Figure 4.7). Stronger convection over Asia forces stronger descending at the American coast due to continuity reasons. In summary, vegetation in Central Asia leads to a stronger Walker circulation in the FD_E simulation than in the DD_E simulation.

The difference in surface temperature between the FD_E simulation and the DD_E simulation further supports the hypothesis of a stronger Walker circulation in the FD_E simulation. At the eastern side of the Pacific Ocean, surface temperature is

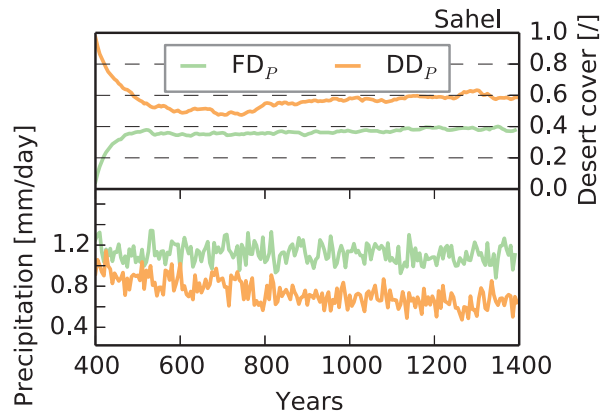


Figure 4.9: Time series of desert cover and precipitation in pre-industrial Sahel in the FD_P simulation (green line) and in the DD_P simulation (orange line). The Sahel region is marked in Figure 4.4. Both time series show five-year mean values.

lower in the FD_E simulation than in the DD_E simulation (Figure 4.8 b). The lower temperature implies a lower SST and a stronger upwelling at the eastern side of the Pacific Ocean. Stronger upwelling in this region indicates a stronger Walker circulation in the FD_E simulation than in the DD_E simulation.

Pre-industrial climate

In the pre-industrial climate, two different vegetation states establish in the Sahel in the DD_P simulation and in the FD_P simulation (Figure 4.4). The desert cover in the Sahel reaches equilibrium at 0.58 in the DD_P simulation (Figure 4.9). At the end of the FD_P simulation, the desert cover in the Sahel is 0.21 smaller than in the DD_P simulation. The precipitation in the Sahel is about two times stronger.

At the beginning of the FD_P simulation, precipitation in the Sahel is two times stronger than at the beginning of the DD_P simulation. Starting from the more humid climate,

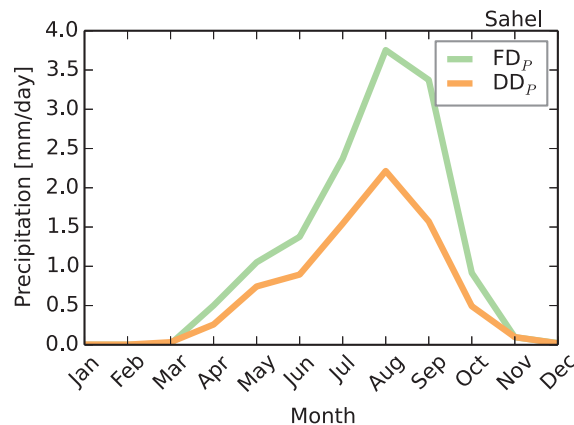


Figure 4.10: Annual cycle of precipitation in the pre-industrial Sahel. The respective region is marked in Figure 4.4. The lines refer to the end of the FD_P simulation (green) and in the DD_P simulation (orange) simulation. 30-year average values are shown.

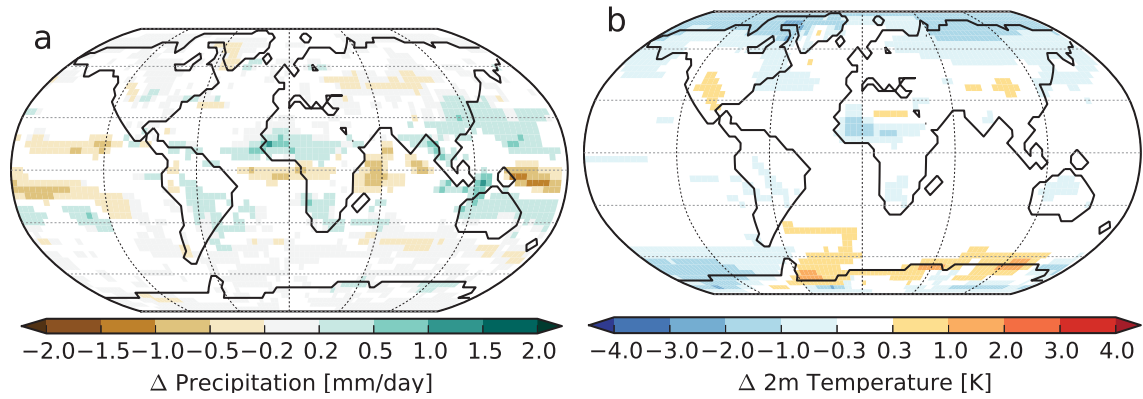


Figure 4.11: Precipitation differences (a) and temperature differences (b) between the end of the FD_P simulation and the end of the DD_P simulation. Depicted differences are significant on a 95% confidence interval.

more vegetation survives in the FD_P simulation. The persisting vegetation maintains high precipitation rates especially in the monsoon season (Figure 4.10).

With a smaller desert cover in the Sahel, regional climate differs in the FD_P simulation and in the DD_P simulation (Figure 4.11). On a global scale, however, climatic differences are weak. The reason for the limited impact of the vegetation in the Sahel on climate is the location of the Sahel relative the atmospheric circulation. Northern Africa lies in a subsidence region in the DD_P simulation (Figure 4.12). In the FD_P simulation, more vegetation enhances evapotranspiration in the Sahel. However, the surplus in evapotranspiration induces only weak convection, because subsidence suppresses convection. A similar global atmospheric circulation prevails in the FD_P simulation as in the DD_P simulation. With a similar atmospheric circulation, the global climate is similar in both simulations.

I showed above that the vegetation in the early Eocene Central Asia affects global climate by inducing convection. In contrast to the pre-industrial Sahel, the early Eocene Asian desert lies in a convection region. In the convection region, vegetation can induce convection. Due to the increase in convection by vegetation, multiple stable vegetation states in the Asian desert lead to two atmospheric circulation states. This result suggests that the location of multiple vegetation-atmosphere states determines the spatial extent of the instability. The location of the multiple vegetation-atmosphere states strongly depends on the specific continent distribution and orography. For instance, during the early Eocene the Tethys Ocean spread where North Africa is located today. In turn, the present-day Arabian Sea appears where the Asian desert establishes in my early Eocene simulations. I conclude that the specific distribution of continents leads to a global instability in the vegetation-atmosphere system in the early Eocene climate.

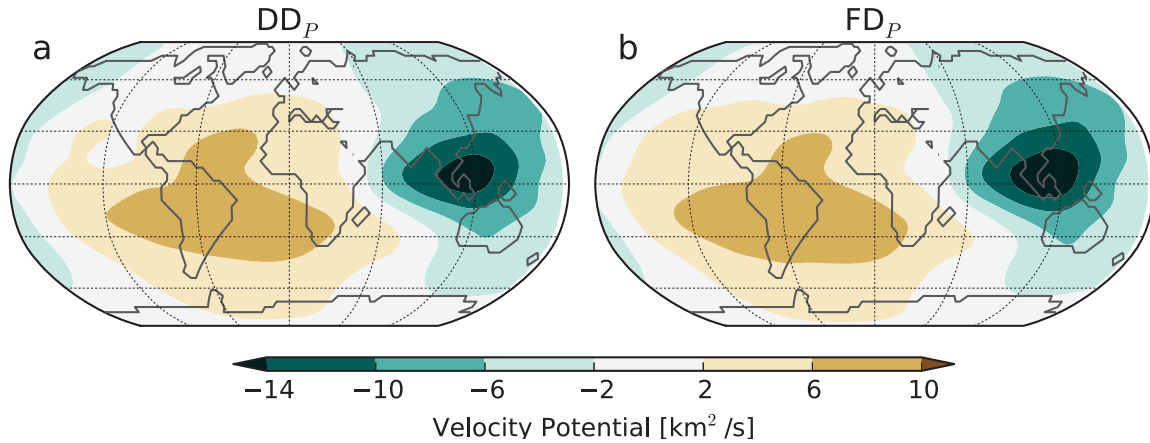


Figure 4.12: Velocity potential at 200 hPa in the FD_P simulation (a) and in the DD_P simulation (b). The 30-year average for the African monsoon season (July, August, and September) is shown. Brownish colours refer to a positive velocity potential. Air converges in regions of positive velocity potential and air subsides below. Greenish colours refer to a negative velocity potential. Air diverges in regions of negative velocity potential and air rises below.

4.3.2 Bright soil: albedo feedbacks stabilise the vegetation-atmosphere system

Early Eocene climate

In this section, I present the results of the bright-soil simulations. With bright soil, the vegetation cover reaches the same state in the FB_E simulation as in the DB_E simulation (Figure 4.14). In Central Asia, precipitation drops immediately and desert expands rapidly in the first decades of the FB_E simulation (Figure 4.13). After about 300 years, the vegetation cover reaches the same desert state as establishes in the DB_E simulation.

The rapid decrease in precipitation and the expansion of desert in Central Asia in the

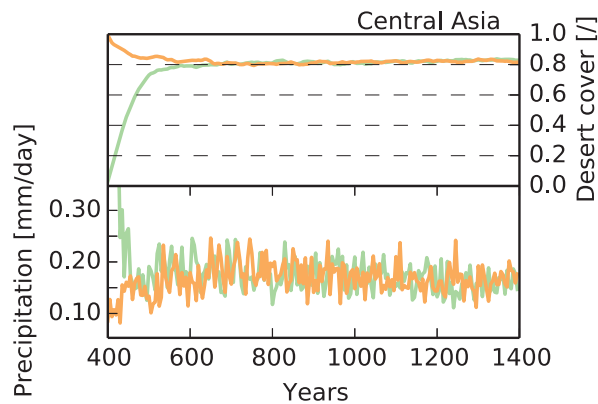


Figure 4.13: Time series of desert cover and precipitation in early Eocene Central Asia in the FB_E simulation (green line) and in the DB_E simulation (orange line). The early Eocene Central Asia is marked in Figure 4.4. Both time series show five-year mean values.

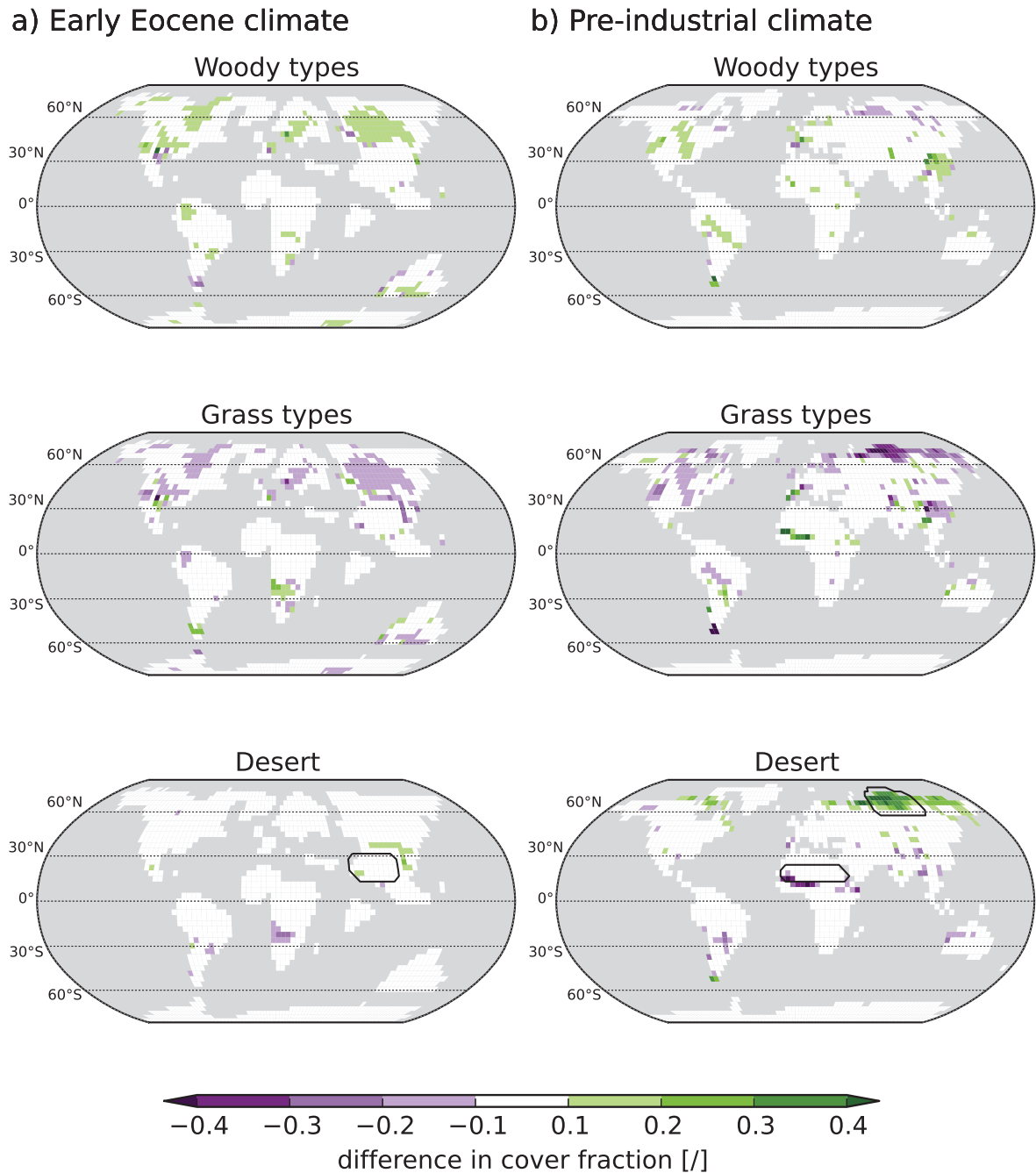


Figure 4.14: Bright soil: Differences in vegetation cover between the simulations that start from a forest world and from a desert world. Shown are differences in vegetation cover for the early Eocene climate ($FB_E - DB_E$) (a) and for the pre-industrial climate ($FB_P - DB_P$) (b). Mapped differences are significant on a 95% confidence interval. Woody types include all trees and shrubs. Grass types refer to C_4 grass and to C_3 grass. Green colours indicate a higher cover fraction in the FD simulation than in the DD simulation. Purple colours indicate a smaller cover fraction in the FD simulation. Black contour lines mark regions which are analysed in more detail in Figure 4.13 and Figure 4.18.

Table 4.2: Radiation at the top of the atmosphere, hydrology, surface albedo, and surface temperature in early Eocene Central Asia in the initial state and final state of the FB_E simulation and DB_E simulation. The considered region is marked in Figure 4.14. The initial state refers to the average over the last 30 years of the forest world and bright-desert world simulation (Figure 4.2). The final state refers to the average over the last 30 years of the respective simulation.

	FB_E		DB_E	
	Initial state	Final state	Initial state	Final state
Net ToA radiation [W/m^2]	22.1	-26.4	-28.6	-26.8
solar [W/m^2]	303.7	259.2	251.3	259.8
terrestrial [W/m^2]	-281.6	-285.4	-279.9	-286.4
Precipitation [mm/day]	1.63	0.17	0.08	0.18
Evapotranspiration [mm/day]	-1.5	-0.16	-0.03	-0.16
Vert. inter. humidity [kg/m^2]	36.3	17.7	14.0	17.8
Relative cloud cover [∕]	0.32	0.18	0.2	0.18
Surface albedo [∕]	-0.13	-0.37	-0.4	-0.37
Surface temperature [$^{\circ}C$]	34.2	26.7	23.7	2.2

FB_E simulation is connected to the soil albedo. At the beginning of the FB_E simulation, precipitation is not sufficient to maintain a dense vegetation cover. The first retreat of vegetation enhances surface albedo, because the soil albedo is much higher than the vegetation albedo. The increase in surface albedo induces the vegetation-albedo-precipitation feedback introduced by Charney (1975) and Charney et al. (1977) (cf. Section 4.1.1).

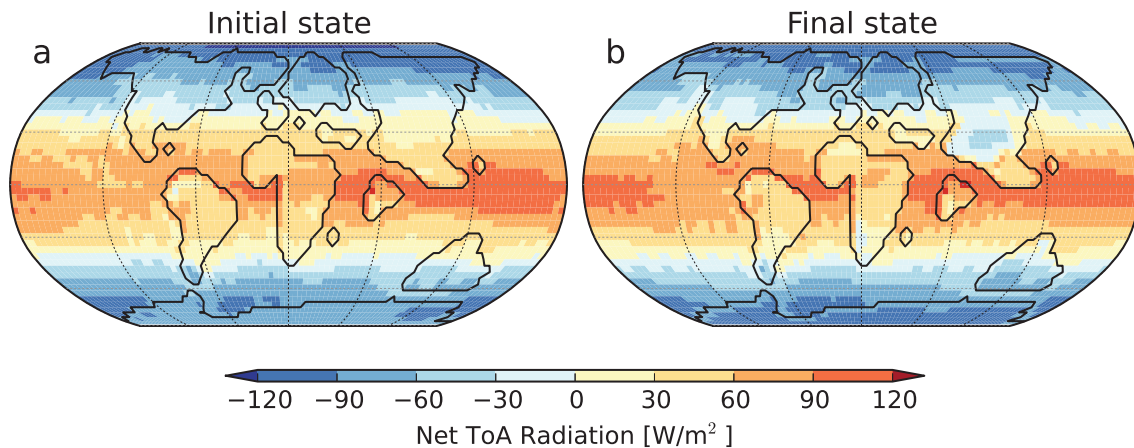


Figure 4.15: Net radiation at the top of the atmosphere in the initial state (a) and in the final state (b) of the FB_E simulation. The initial state refers to the average over the last 30 years of the early Eocene forest world simulation. The final state reflects the average over the last 30 years of the FB_E simulation. Yellow colours and reddish colours indicate a positive net radiation at the top of the atmosphere. The atmosphere gains energy in these regions. Bluish colours indicate a loss of energy. During the simulation, net radiation mainly changes in Central Asia.

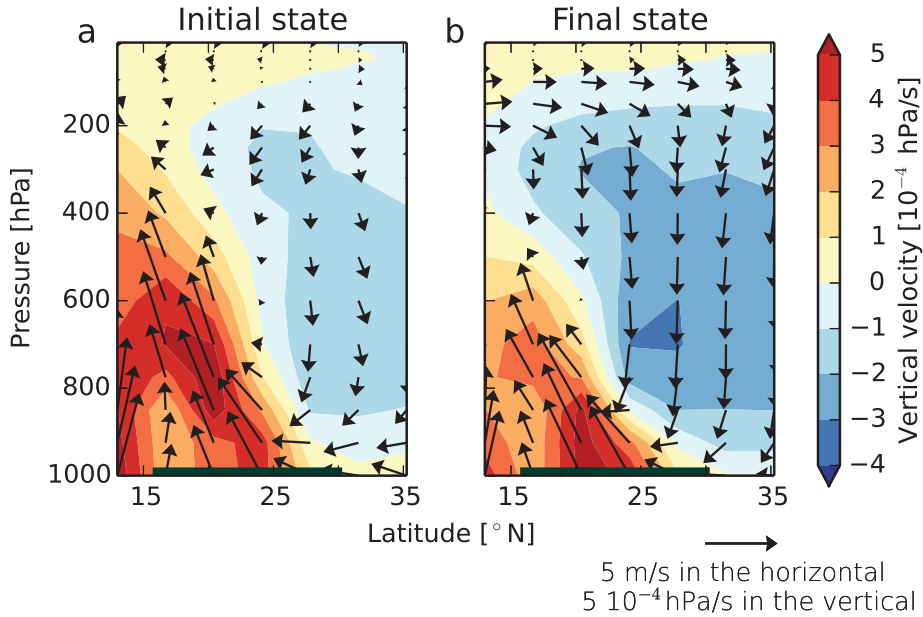


Figure 4.16: Meridional circulation averaged from 58°E to 90°E in the initial state (a) and in the final state (b) of the FB_E simulation. Shown is the seasonal mean over July, August, and September. The initial state and the final state refer to the average over the last 30 years of the forest world simulation and of the FB_E simulation. The location of the Asian desert is marked by the grey bar at 1000 hPa.

I illustrate the Charney feedback based on the radiation balance at the top of the atmosphere (ToA) and the meridional circulation over Central Asia. At the beginning of the FB_E simulation, forest covers all continents. In this case, net ToA radiation over Central Asia is as strong as over the adjacent regions (4.15 a). The meridional circulation is characterised by rising air over the southern part of the Asian desert (Figure 4.16 a). Hence, convection occurs over the Asian desert and annual-mean precipitation is 1.63 mm/day.

During the FB_E simulation, vegetation cover shrinks and surface albedo increases from 0.13 to 0.37 (Table 4.2). The increase in surface albedo enhances outgoing ToA solar radiation by 45 W/m^2 . Furthermore, shrinking vegetation cover reduces evapotranspiration. Weaker evapotranspiration leads to a lower air humidity and fewer clouds. With a lower humidity and fewer clouds, less long-wave radiation is trapped in the atmosphere. The outgoing ToA long-wave radiation increases by 4 W/m^2 over Central Asia during the FB_E simulation. In the sum, net ToA radiation decreases by 49 W/m^2 due to shrinking vegetation cover.

At the end of the FB_E simulation, net ToA radiation over Central Asia is negative. In the adjacent regions, net ToA radiation remains positive (Figure 4.15 b). The contrast between the loss of radiation over Central Asia and the gain of radiation over the adjacent regions induces subsidence over Central Asia according to Charney's theory (cf. Section 4.1.1). Strong subsidence prevails over northern Central Asia (Figure 4.16 b). Over southern Central Asia, convection becomes weak during the FB_E simulation. With stronger subsidence, precipitation declines by 1.46 mm/day (90%) to 0.14 mm/day in Central Asia.

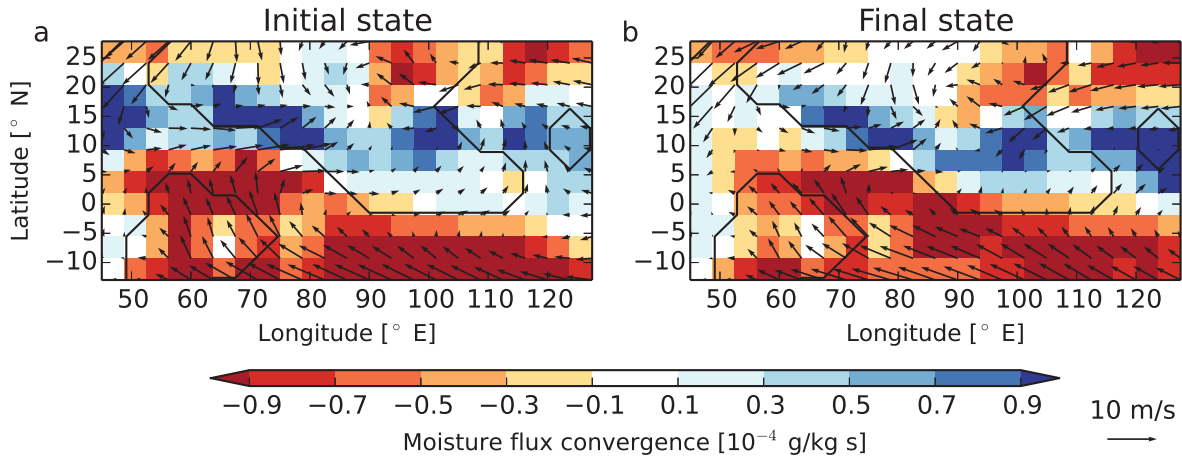


Figure 4.17: Moisture convergence at the surface (shading) and wind at 10 meters above the surface (arrows) in the initial state (a) and in the final state (b) of the FB_E simulation. Shown is the seasonal mean for July, August, and September. The initial state and the final state refer to the average over the last 30 years of the forest world simulation and of the FB_E simulation.

The strong subsidence over Central Asia at the end of the FB_E simulation leads to divergence at the surface in this region (Figure 4.16). Divergence counteracts the Asian monsoon. To illustrate the weakening of the Asian monsoon, I analyse the horizontal moisture flux convergence together with the horizontal wind field. Banacos and Schultz (2005) define the horizontal moisture flux convergence, MFC , as

$$MFC = \nabla \cdot (q\mathbf{V}). \quad (4.3)$$

I consider the specific humidity, q , and the horizontal wind, \mathbf{V} , near the surface to calculate the horizontal surface moisture flux convergence. I calculate the 30-year average of the monsoon season (July, August, and September) of the horizontal surface moisture flux convergence and of the surface wind field.

Figure 4.17 a) shows the horizontal moisture flux convergence at the surface over Central Asia at the beginning of the FB_E simulation. Moisture converges in the southern part of Central Asia, because south-westerlies transport moist air from the ocean to Central Asia. At the end of the FB_E simulation, subsidence is strong over Central Asia. With strong subsidence, the south-westerlies are weak and the horizontal moisture flux convergence is weak (Figure 4.17 b).

Meehl (1994) suggests that an increase in surface albedo in present-day Central Asia weakens the Asian monsoon, because an increase in albedo causes a reduction in surface temperature. He shows that the temperature drop decreases the temperature contrast between the ocean and the continent. This temperature contrast is a major driver of the Asian monsoon (Webster 1987). Hence, the Asian monsoon becomes weaker with a smaller temperature contrast. During my FB_E simulation, the surface temperature decreases by 7.5 K in Central Asia (Table 4.2). Following Meehl (1994), this temperature drop weakens the Asian monsoon. I suggest that both the temperature drop and subsidence induced by the Charney effect weakens the Asian monsoon in the FB_E simulation.

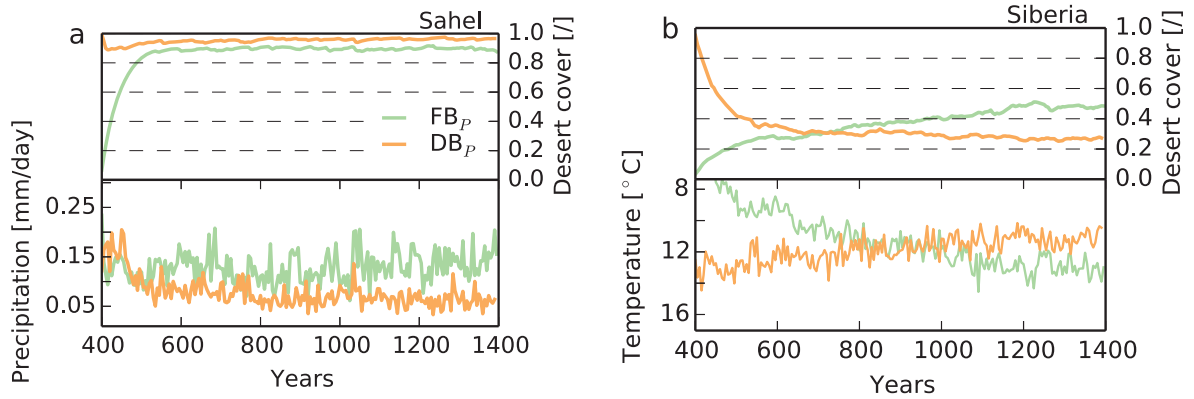


Figure 4.18: Time series of desert cover and precipitation in pre-industrial Sahel (a) and time series of desert cover and temperature at 2 m above the surface in Siberia (b) in the FB_P simulation (green line) and in the DB_P simulation (orange line). The Sahel region is marked in Figure 4.14. All time series show five-year mean values.

Pre-industrial climate

In the pre-industrial climate, vegetation cover in the Sahel reaches the same state in the FB_P simulation as in the DB_P simulation (Figure 4.14 and 4.18 a). Like in early Eocene Central Asia, the Charney feedback amplifies aridification in the Sahel in the FB_P simulation. At the beginning of the FB_P simulation, precipitation is too weak for a dense vegetation cover in the Sahel leading to a retreat of vegetation. The resulting increase in surface albedo induces subsidence and reduces precipitation in the Sahel. The reduction in precipitation leads to further retreat of the vegetation cover. This feedback continues until the Sahel reaches same desert state as evolves in the DB_P simulation.

Table 4.3: Radiation at the top of the atmosphere, hydrology, surface albedo, and surface temperature in the pre-industrial Sahel in the initial state and final state of the FB_P simulation and DB_P simulation. The considered region is marked in Figure 4.14. The initial state refers to the average over the last 30 years of the forest world and bright-desert world simulation (Figure 4.2). The final state refers to the average over the last 30 years of the respective simulation.

	FB _P		DB _P	
	Initial state	Final state	Initial state	Final state
Net ToA radiation [W/m ²]	35.8	-10.8	-4.65	-15.41
solar[W/m ²]	304.7	261.2	254.0	258.8
terrestrial [W/m ²]	-268.9	-272.0	-258.7	-274.3
Precipitation [mm/day]	1.37	0.16	0.11	0.06
Evapotranspiration [mm/day]	-1.34	-0.15	-0.03	-0.04
Vert. inter. humidity [kg/m ²]	28.0	14.9	12.0	13.8
Relative cloud cover [/]	0.36	0.25	0.34	0.23
Surface albedo [/]	0.13	0.38	0.4	0.39
Surface temperature [°C]	30.7	25.2	22.4	24.6

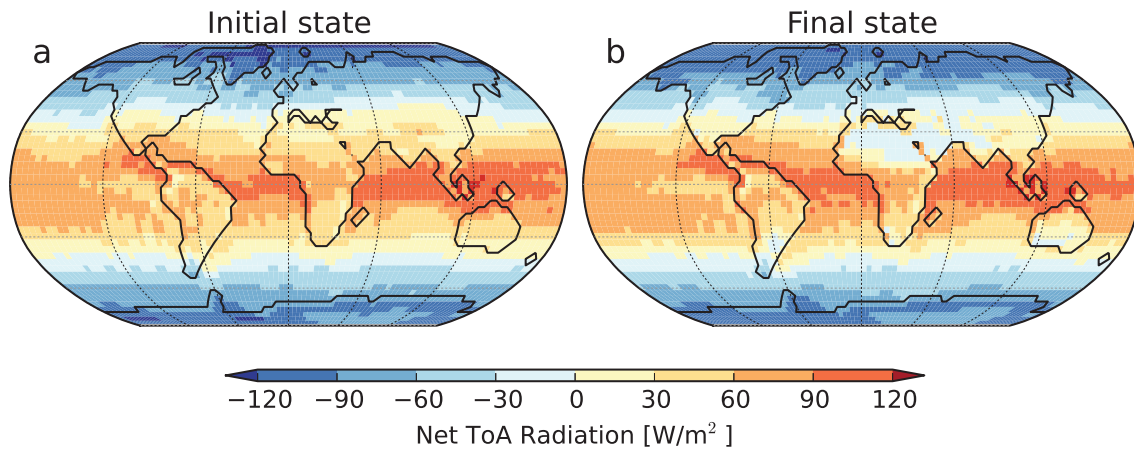


Figure 4.19: Net radiation at the top of the atmosphere in the initial state (a) and in the final state (b) of the FB_P simulation. The initial state and the final state refer to the average over the last 30 years of the forest world simulation and of the FB_P simulation. Yellow colours and reddish colours refer to a positive net radiation at the top of the atmosphere. The atmosphere gains energy in these regions. Bluish colours indicate a loss of energy. During the FB_P simulation, net ToA radiation changes strongly above the Arabian desert and Northern Africa.

The ToA radiation balance over the Sahel confirms the Charney feedback in the FB_P simulation. Shrinking vegetation cover in the Sahel increases surface albedo by 0.25 from the beginning until the end of the FB_P simulation (Table 4.3). The increase in surface albedo reduces net solar ToA radiation by 43.5 W/m^2 . With less vegetation, evapotranspiration decreases. Less evapotranspiration leads to a lower air humidity and fewer clouds. More long-wave radiation escapes from the atmosphere due to the reduction in humidity and cloud cover. Net ToA radiation decreases by 47 W/m^2 from the beginning until the end of the FB_P simulation. Net ToA radiation over the Sahara becomes negative. In the adjacent regions, vegetation persists. The net ToA radiation remains positive over the adjacent regions (Figure 4.19). The energy loss over the Sahara and the energy gain over the adjacent region establish a temperature contrast between cold air above the Sahara and warm air above the vegetated adjacent regions. This temperature contrast forces subsidence above the Sahara. Subsidence suppresses convection and reduces precipitation.

Figure 4.20 illustrates that subsidence becomes stronger during the FB_P simulation. At the beginning of the FB_P simulation when forest covers the Sahel, air rises up to 300 hPa over the Sahel. At the end of the simulation, a desert spreads in the Sahel. Subsidence is strong over whole Northern Africa (Figure 4.21 b). Only at the southern edge of the Sahel, air rises slightly.

The airflow from the oceans to the Sahel is similar at the beginning and at the end of the FB_P simulation. In the early Eocene Central Asia, the flow of moist air from the oceans weakens with an increase in surface albedo. The weaker flow of moist air from the ocean amplifies aridification in early Eocene Central Asia. This effect is absent in the pre-industrial Sahel.

For present-day Sahara, Claussen (1997, 1998) simulates two stable vegetation states.

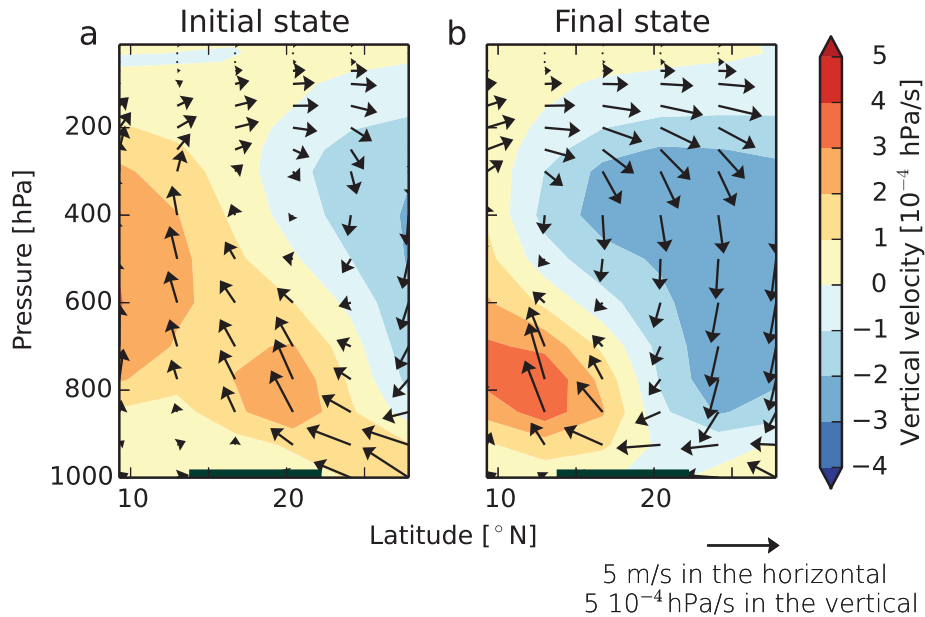


Figure 4.20: Meridional circulation averaged from 10°W to 40°E in the initial state (a) and in the final state (b) of the FB_P simulation. Shown is the seasonal mean over July, August, and September. The initial state and the final state refer to the average over the last 30 years of the forest world simulation and of the FB_P simulation. The location of the Asian desert is marked by a grey bar at the 1000 hPa level.

Starting the simulation from a forest world and from a desert world, a humid climate with dense vegetation and a dry climate with sparse vegetation establish in the Sahel, respectively. In the simulation that starts from the forest world, precipitation is strong enough to maintain a dense vegetation cover in the Sahel. With a persisting vegetation, the surface albedo remains low. Without an increase in surface albedo, the Charney feedback is absent and the dense vegetation cover persists.

In the beginning of the FB_P simulation, precipitation is too weak for a dense vegetation cover in the Sahel. Shrinking vegetation cover initiates the Charney feedback which continues until climate and vegetation in the Sahel reach a desert state. The transition from a forest to a desert in the Sahel suggests that a first decrease in vegetation cover leads to a desert state. In other words, the Charney effect prevents stable semi-desert states in pre-industrial Sahel.

In Siberia, more grass appears in the DB_P simulation than in the FB_P simulation (Figure 4.14). The time series of the desert cover and of the temperature illustrate the driving mechanism of the difference in vegetation cover. At the beginning of the FB_P simulation, temperature is not sufficient to maintain a dense vegetation cover (Figure 4.18 b). Decreasing vegetation cover increases surface albedo, because fewer dark branches mask the bright snow cover. With a higher surface albedo, the surface absorbs less solar radiation. The resulting cooling leads to further decrease in the vegetation cover. In the DB_P simulation, the same feedback occurs but with the opposite direction. At the beginning of the DB_P simulation, the climate is warm enough for plant growth. Increasing vegetation cover reduces surface albedo due to

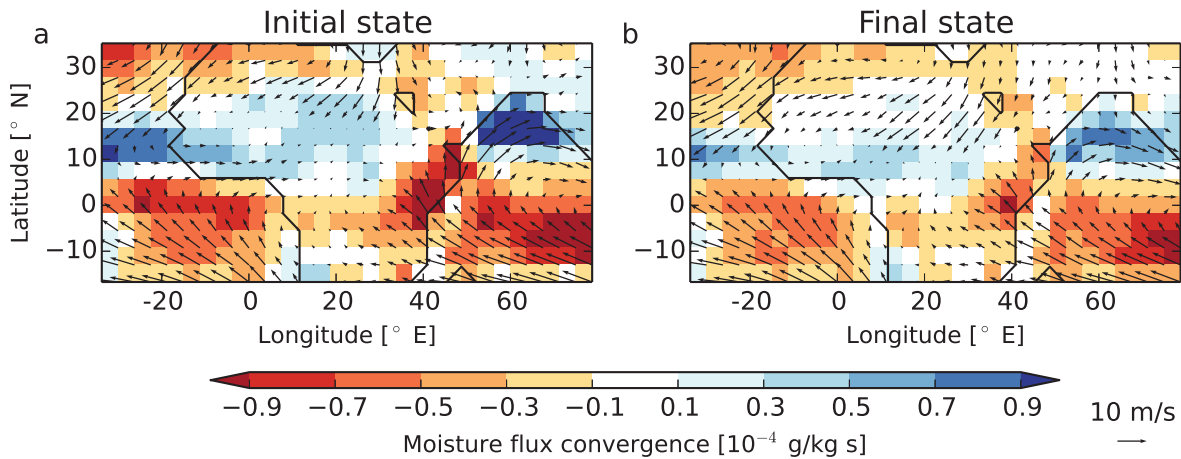


Figure 4.21: Moisture convergence at the surface (shading) and wind at 10 meters above the surface (arrows) in the initial state (a) and in the final state (b) of the FB_P simulation. Shown is the seasonal mean over July, August, and September. The initial state and the final state refer to the average over the last 30 years of the forest world simulation and of the FB_P simulation.

the snow masking effect. With a lower surface albedo, temperature increases and vegetation cover expands further.

Interestingly, the vegetation cover in the DB_P simulation overshoots the vegetation cover in the FB_P simulation. At the end of the simulations, desert cover reaches 0.27 and 0.48 in the DB_P simulation and in the FB_P simulation, respectively (Figure 4.18 b). However, the climate and the vegetation cover in Siberia are not in equilibrium at the end of both simulations. The long time scale of vegetation dynamics in the cold northern high latitudes has been emphasised by Devaraju et al. (2011). Due to the slow vegetation dynamics in Siberia, I cannot say whether the climate-vegetation state will turn into the same state in both simulations or whether two stable equilibrium states will develop.

The study by Dekker et al. (2010) suggest that multiple vegetation-atmosphere states may exist in the northern high latitudes. They use a model of intermediate complexity which represents vegetation as gross primary production (GPP). They start one simulation from maximum GPP and another simulation from minimum GPP. A positive feedback between GPP, albedo, and temperature leads to a larger biomass in the northern high latitudes when the simulation starts from maximum GPP instead of from minimum GPP. In other words, their simulations and my simulations come to opposite results. As mentioned above, my simulations, however, are not in equilibrium. Extending the simulations might change my results.

Brovkin et al. (2009) investigate the stability of present-day vegetation cover using a previous version of MPI-ESM. They simulate present-day vegetation cover starting from forest on all continents and starting from grass on all continents. After 500 years, boreal vegetation reaches the same equilibrium in both simulations. In my version of MPI-ESM, the lifetime of extra-tropical trees is 50 years instead of 30 years as in the MPI-ESM-version used by Brovkin et al. (2009). The change in lifetime is likely the reason for the slower vegetation dynamics in my simulations relative to the study by

Brovkin et al. (2009).

4.4 Summary and Conclusion

I investigate and compare the stability of the vegetation-atmosphere system in the pre-industrial climate and in the early Eocene climate. Using the Max Planck Institute for Meteorology Earth System Model (MPI-ESM), I simulate both climates and the respective vegetation covers with two different initial vegetation covers. Either dense forest or bare soil spreads on all continents at the beginning of the simulations. I analyse whether multiple stable vegetation-atmosphere states establish for the two initial vegetation covers. To identify the mechanism that causes instabilities in the vegetation-atmosphere system, I vary the soil albedo. All soils have either a much higher albedo than vegetation or a similar albedo as vegetation.

With a high soil albedo, vegetation affects the hydrological cycle and reduces the surface albedo relative to bare soil. In this case, only one stable vegetation-atmosphere state establishes in the pre-industrial climate as well as in the early Eocene climate. Previous studies suggest that albedo changes by vegetation cause multiple vegetation-atmosphere states in present-day Sahara. The pre-industrial simulations, however, suggest that albedo changes by vegetation prevent multiple vegetation-atmosphere states in the Sahara.

With a low soil albedo, vegetation mainly affects the hydrological cycle. In this case, multiple vegetation-atmosphere states exist in the pre-industrial climate and in the early Eocene climate. In the pre-industrial Sahel, vegetation depends on precipitation. At the same time, vegetation enhances water recycling and increases precipitation. The resulting feedback between vegetation and precipitation leads to more vegetation in the Sahel when the initial vegetation cover is forest instead of bare soil on all continents.

In the early Eocene climate, multiple vegetation-atmosphere states exist for a desert in Central Asia. Similar to the pre-industrial Sahel, vegetation depends on precipitation and enhances water recycling in Central Asia. Due to the resulting feedback, a small Asian desert and a large Asian desert evolve when the simulation starts from a forest world and from a desert world, respectively. Moreover, vegetation enhances the Asian monsoon. The resulting shift in the large scale atmospheric circulation leads to two globally different climate states with a large Asian desert and with a small Asian desert. In the two climate states, further multiple vegetation states exist on the American continent. So far, such a global connection of multiple vegetation-atmosphere states in several regions has not been identified in present-day climate.

In my pre-industrial simulations, the multiple stable vegetation-atmosphere states are predominately limited to Northern Africa. With present-day distribution of continents, subsidence prevails over Northern Africa. Consequently, vegetation induces only weak convection and fails to shift large scale atmospheric circulation. I conclude, that the spatial extent of an instability in the vegetation-atmosphere system depends on the distribution of continents and on the climate state. On geological time scales, the distribution of continents and the climate change permanently. Hence, the stability of the vegetation-atmosphere system is likely specific for each climate.

Chapter 5

Simulating Early Eocene Plant Species

In order to evaluate the early Eocene vegetation cover simulated by the Max Planck Institute for Meteorology Earth System Model (MPI-ESM), I compare the simulated vegetation cover with reconstructions of palaeovegetation. The evaluation focuses on the limitation that arises from using present-day Plant Functional Types (PFTs) to simulate the early Eocene vegetation cover. Further, I develop ideas to improve the representation of the early Eocene vegetation cover and plant taxa in MPI-ESM.

5.1 Introduction

Simulating the early Eocene climate is still a challenge because climate models fail to reproduce the warm high latitudes that are suggested by temperature reconstructions (Lunt et al. 2012). The contradiction of climate models and temperature reconstructions in the high latitudes indicates that the state-of-the-art climate models might lack important processes and might fail to simulate climate states that differ from the present one (Valdes 2012). Hence, many studies seek to understand the discrepancy between the simulated and the reconstructed early Eocene temperatures (Huber and Caballero 2011). Loftson et al. (2014) investigate whether an improved representation of the vegetation cover reduces this discrepancy. Previous studies assume a homogeneous vegetation cover such as savannah or shrub land on all continents (Heinemann et al. 2009; Lunt et al. 2010). Loftson et al. (2014) use an Earth System Model (ESM), which simulates the early Eocene climate and vegetation cover interactively. The resulting early Eocene climate matches climate reconstructions better than the climate simulated with a homogeneous shrub cover on all continents. Especially in the high latitudes, the interactive vegetation cover improves the agreement to temperature reconstructions relative to the shrub cover.

ESMs represent vegetation in PFTs which are groups of plant species that share similar properties. Those PFTs are designed to represent present-day plant taxa. During the early Eocene, however, plant taxa were different from today's plant taxa. For instance, C_4 grass is common today but did not exist during the early Eocene. The C_4 pathway developed after the early Eocene—during the mid to late Miocene (16 - 5 Ma) (Cerling et al. 1993). Instead, other typical taxa were common during the early Eocene but are not considered in ESMs such as fern or paratropical rainforest (Utescher and Mosbrugger 2007; Wolfe 1985).

The discrepancy between the PFTs and the plant taxa of the past has often been emphasised (e.g. Donnadieu et al. 2009; Loptson et al. 2014). Nevertheless, attempts to adapt the PFTs to plant taxa of the past are rare. Taking the first step in this direction, I compare the early Eocene vegetation cover simulated in Chapter 4 with vegetation reconstructions. The focus lies on the limitation that emerges in the simulated vegetation from using PFTs that represent today’s plant taxa. Further, I review in which way the early Eocene plant taxa differed from present-day plant taxa, and I develop ideas to improve the representation of early Eocene vegetation in MPI-ESM.

5.2 Method

Using the MPI-ESM, I simulate the early Eocene climate and vegetation cover interactively. MPI-ESM includes the land surface scheme JSBACH which calculates the vegetation cover (Reick et al. 2013). The vegetation cover is composed of the eight PFTs listed in Table 5.1 and deserts. All regions where net primary production (NPP) is not sufficient to maintain plant tissues refer to deserts. In all other regions, JSBACH derives the vegetation composition from disturbances and bioclimatic limits prescribed for each PFT (Table 5.1). Disturbances, i.e. fire and windthrow, remove all vegetation. After disturbances, grass types (C_4 grasses and C_3 grasses) expand at first. Woody types (all trees and shrubs) follow because they establish slower than grass types. Hence, in case of frequent disturbances, a grassland prevails even though climate allows woody types. Woody types compete based on their bioclimatic limits and their NPP. In the sum, the vegetation composition establishes depending on bioclimatic demands, NPP, and disturbances.

I consider the vegetation cover of the FD_E simulation (Chapter 4). The early Eocene boundary conditions are described in Chapter 2. In the FD_E simulation, all soils have

Table 5.1: The bioclimatic limits and the phenology of the PFTs in JSBACH. The minimum and the maximum of the lowest multi-year monthly-mean temperature are reflected by TC_{\min} and TC_{\max} , respectively. TW_{\max} is the maximum of the highest multi-year monthly-mean temperature. GDD_{\min} is the minimum of growing degree days. All these parameters are given in $^{\circ}C$. If no value is given, no limit exists. JSBACH considers four types of phenology. Evergreen vegetation does not shed its leaves. Summergreen and raingreen PFTs shed their leaves when climate gets too cold and too dry, respectively. Grasses have their own phenology.

Plant Functional Type	TC_{\min}	TC_{\max}	TW_{\max}	GDD_{\min}	Phenology
Tropical evergreen trees	15.5	–	–	–	raingreen
Tropical deciduous trees	15.5	–	–	–	raingreen
Extra-tropical evergreen trees	-32.5	18.5	–	350	evergreen
Extra-tropical deciduous trees	–	18.5	–	350	summergreen
Raingreen shrubs	2.0	–	–	900	raingreen
Deciduous shrubs	–	-2.0	18.0	300	summergreen
C_3 grass	–	15.0	–	–	grass phenology
C_4 grass	10.0	–	–	–	grass phenology

an albedo of 0.1. The simulation starts from a forest world and runs for 1000 years. After that time, global mean vegetation cover is in equilibrium.

The simulated vegetation cover is compared to the vegetation reconstruction by Utescher and Mosbrugger (2007). The reconstruction is based on a collection of flora fossils (macroflora and microflora) from 143 globally-distributed localities. Utescher and Mosbrugger (2007) allocate the fossil taxa to their Nearest Living Relatives (NLRs) using the palaeobotanical data base 'Palaeoflora' (Utescher and Mosbrugger (2006)). Further, they group the NLRs to PFTs. The relative abundance of a PFTs in a flora refer to the diversity of the PFT.

Diversity is a measure of plant composition in an ecosystem and reveals information about occurrence and dominance of plant species. JSBACH provides the absolute coverage of each PFT. Hence, a quantitative comparison of the reconstructed diversity and the simulated coverage of a PFT is not possible. Instead, I use the diversity as a proxy for the occurrence of a PFT. I assume that a PFT occurred when its diversity exceeds 10%. I then compare the simulated spatial distribution of a PFT to the reconstructed spatial distribution of a PFT (Figure 5.1). JSBACH considers different PFTs than Utescher and Mosbrugger (2007) consider for the vegetation reconstructions. The allocation of the simulated PFTs to the reconstructed PFTs is shown in Table 5.2.

The fossil collection by Utescher and Mosbrugger (2007) includes flora from the whole Eocene (~ 54.8 to 33.7 Ma). I consider reconstructions from the period after the Paleocene-Eocene Thermal Maximum (PETM) until the Early Eocene Climatic Optimum (EECO) for comparison only.

Table 5.2: Arboreal PFTs in JSBACH and their allocation to the arboreal PFTs by Utescher and Mosbrugger (2007).

PFTs in JSBACH	PFTs by Utescher and Mosbrugger (2007)
Tropical evergreen trees	broad-leaved evergreen tropical tree
Tropical deciduous trees	broad-leaved raingreen trees
Extra-tropical evergreen trees	broadleaved evergreen temperate trees needle-leaved evergreen trees
Extra-tropical deciduous trees	broadleaved summergreen trees needle-leaved summergreen trees

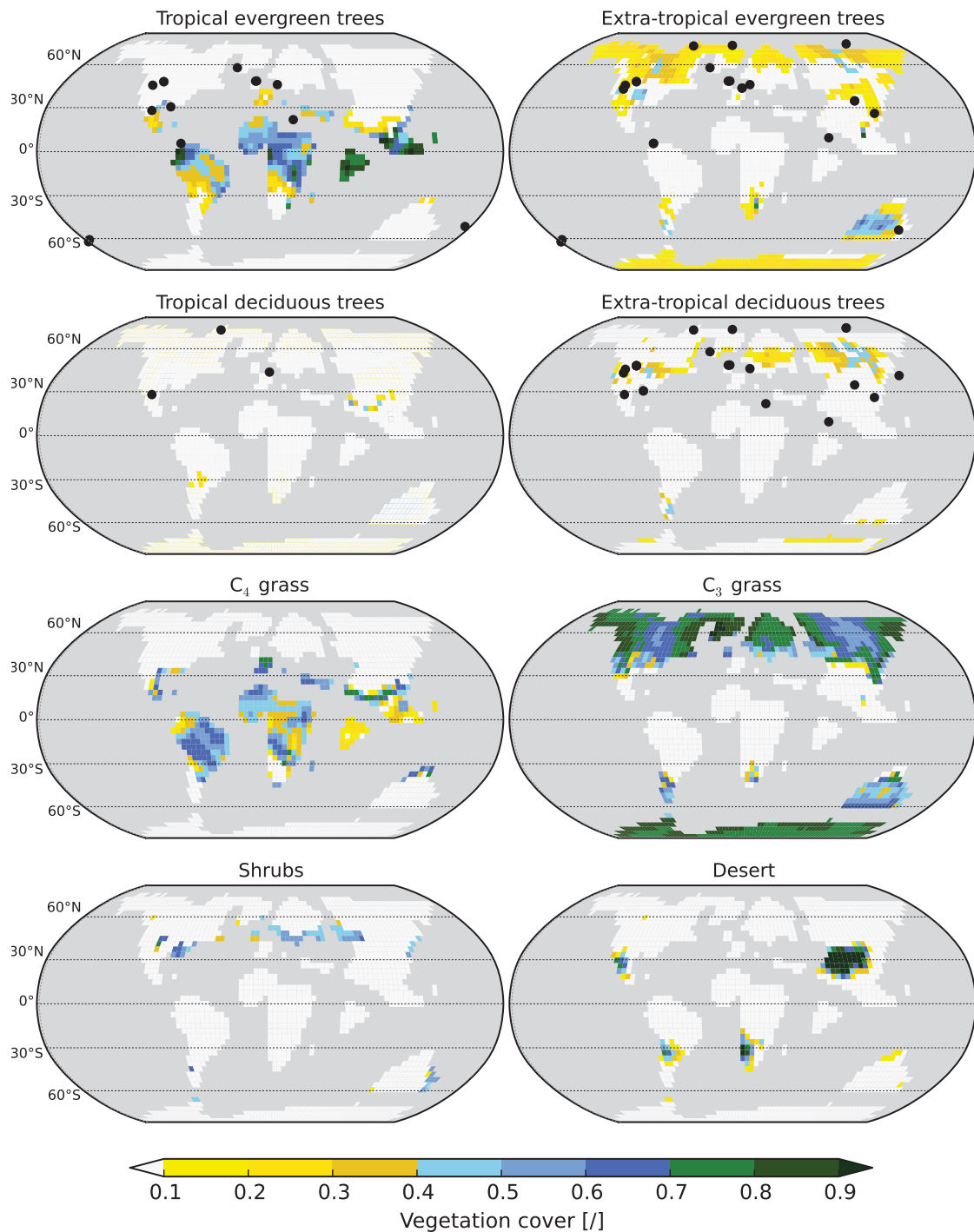


Figure 5.1: Simulated early Eocene vegetation cover in the FD_E simulation in shading. Dots indicate sites where the flora collection by Utescher and Mosbrugger (2007) suggests the existence of the respective PFTs. The allocation of reconstructed PFTs to simulated PFTs is listed in Table 5.2.

5.3 Results

Fossil assemblages indicate that tropical forest extended between 60° north and 60° south (Wolfe 1985; Willis and McElwain 2002; Utescher and Mosbrugger 2007). In the simulation, however, tropical forest is bounded between 30° north and 30° south (Figure 5.1). Poleward of 30° north and 30° south, the bioclimatic limit for tropical trees is not fulfilled because the coldest multi-year monthly-mean temperature drops below 15.5°C (Table 5.1). To reduce the mismatch between the simulated and the reconstructed extent of tropical trees, Thomas Hickler¹ raised the idea to change the bioclimatic limit of tropical trees in JSBACH. As an alternative to the monthly-mean temperature threshold, the occurrence of frost is a reasonable criterion for tropical trees. Present-day tropical trees resist cold temperature as long as temperature stays above the freezing point. In case of sub-freezing temperatures, plant tissues die because the cellular water in the cell interior crystallises (Lüttge 2008).

I evaluate the frost criteria based on the simulated surface temperature. Figure 5.2 marks the regions where the six-hourly temperature never drops below 0°C in 30 years and the regions where the lowest multi-year monthly-mean temperature is above 15.5°C. Both approaches lead to almost the same result. Only in few coastal regions, the frost criteria has a larger poleward extent. The comparison of the two criteria implies that changing the monthly-mean threshold in JSBACH to the frost criteria does not diminish the discrepancies between the reconstructed and the simulated poleward extent of tropical forest. Assuming that tropical trees were sensitive to frost during the early Eocene, the monthly-mean temperature threshold is a valid bioclimatic limit for early Eocene tropical trees as well because it matches the frost criteria.

After evaluating the bioclimatic limit of tropical trees, I conclude that the simulated mid latitudes are too cold for tropical trees. Besides, the evaluation of the simulated early Eocene climate (Chapter 2) illustrates that the simulated mid latitudes are colder than temperature estimates suggest by up to 5°C. Hence, I assume that the simulated climate causes the discrepancy between the simulated and the reconstructed extent of

¹Thomas Hickler, personal communication (June 2013)

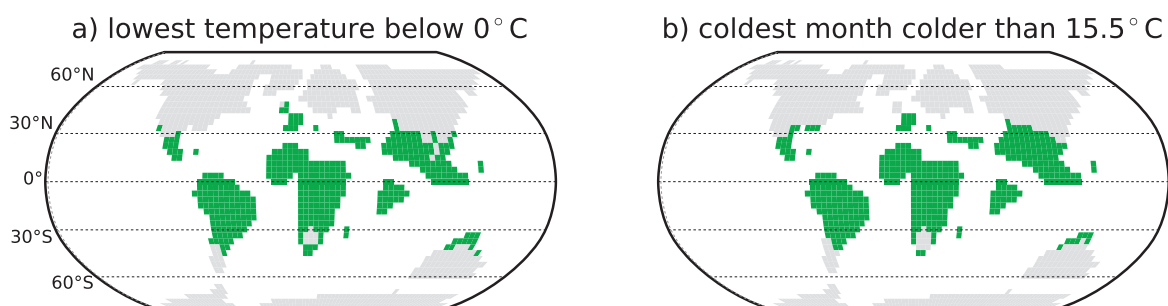


Figure 5.2: Frost criterion and lowest multi-year monthly mean temperature threshold. The simulated early Eocene climate allows tropical trees in the green shaded regions according to the respective criteria. The frost criteria means that the 6-hourly temperature never drops below 0°C. The lowest multi-year monthly mean temperature threshold is 15.5°C.

tropical forest. The discrepancy can only be decreased by simulating warmer mid to high latitudes in agreement with temperature reconstructions.

C₃ grasses dominate the vegetation cover in the mid to high latitudes in the simulation but taxa of C₃ grass occur only at a few sites in early Eocene floras. Wide-spread grassland that are common in present-day climate evolved after the Eocene in the early to mid Miocene (20 -10 Ma) (Janis 1993). In the tropics, JSBACH simulates a large coverage of C₄ grass which does not represent the early Eocene vegetation cover. The C₄ pathway evolved and expanded in the mid to late Miocene (Cerling et al. 1993). Due to the limited extent of grass, the PFTs for grasses should be neglected when simulating the early Eocene vegetation cover.

Arboreal taxa are dominant in most flora fossil assemblages in the mid to high latitudes indicating a dense forest in these regions (Utescher and Mosbrugger 2007). JSBACH, however, simulates an open forest with a tree cover of 30 % and less in this region (Figure 5.1). Instead of trees, grasses dominate the vegetation cover. The grass growth indicates that the NPP is sufficient for vegetation growth. Hence, tree growth is either restricted by the bioclimatic limits of extra-tropical trees or by disturbances. The bioclimatic limit for extra-tropical evergreen trees demands that the lowest multi-year monthly-mean temperature is above -32.5°C (Table 5.1). The warm early Eocene climate fulfills this criterion everywhere. Since climate is sufficient for tree growth, I assume that disturbances remove trees regularly. The dominant disturbance in the simulation is fire.

The question remains whether the fire frequency is overestimated by JSBACH or trees are too sensitive to fires. I assume that both factors play a role. Firstly, the fire frequency is likely overestimated due to the applied fire model and due to the consideration of grasses. The fire model derives the occurrence of fires only from the relative air humidity. The fuel content of the appearing vegetation is neglected. In the latest version of JSBACH, the included fire model SPITFIRE considers the relative air humidity and the fuel content of the vegetation (Thonicke et al. 2010; Lasslop et al. 2014). Based on this approach, grasses burn better than forests in SPITFIRE. Hence, when I exclude grasses and use a SPITFIRE instead of the old fire model, the fire frequency likely decreases. Secondly, the trees in JSBACH might be too sensitive to fires because fire-tolerant or fire-resistant trees are not considered. In present-day climate, trees are adapted to fires in regions where fires occur regularly. Those trees have a thick bark that is fire resistant or even need fires to reproduce (Berg 2008). Assuming fires were more frequent in the warm early Eocene climate, trees likely have been adapted to fires as in present-day climate.

In the northern high latitudes, evergreen trees spread in the simulation while flora fossils indicate deciduous trees (Figure 5.1). Wolfe (1985) describes the *polar forest* as a deciduous forest which shed its leaves due to seasonal droughts and polar night. This forest has no modern analogue because today the cold climate prohibits forest growth in regions of polar night. The present-day conditions make a drought-sensitive, darkness-tolerant forest redundant. Hence, JSBACH considers deciduous extra-tropical trees that shed leaves due to a seasonal cycle in temperature and neglects that forest growth depends on light. These summergreen deciduous extra-tropical trees represent present-day boreal forest but fail to represent the raingreen polar forest described by

Wolfe (1985).

Shrubs are almost absent in the simulation. Deciduous shrubs represent present-day tundra vegetation. JSBACH simulates deciduous shrubs when the coldest month and the warmest month are colder than -2°C and 18°C , respectively (Table 5.1). In the warm early Eocene climate, these bioclimatic limits are rarely fulfilled. In agreement with flora fossils, raingreen shrubs grow around the Tethys Ocean and at the east coast of the Asian Continent (Figure 5.1). In Central Asia, however, raingreen shrubs are absent, even though, flora fossils indicate a high diversity of shrubs in this region.

5.4 Ideas for improvement

After identifying the discrepancies between the simulated and the reconstructed vegetation cover, I collect ideas to improve the representation of the early Eocene vegetation in JSBACH.

Forests

In general, the early Eocene vegetation was characterised by forest which covered all continents and had a high diversity (Utescher and Mosbrugger 2007). JSBACH considers four arboreal taxa only. This number is too small to represent the forest-dominated early Eocene vegetation. For instance, polar forest and paratropical rainforest covered large parts of the globe during the early Eocene but are not represented by any PFT in JSBACH. Implementing polar trees and paratropical trees as PFTs increases the diversity of trees and likely improves the representation of early Eocene vegetation.

Polar trees covered the northern high latitudes. A modern analogue for polar trees is absent because they shed their leaves due to seasonal droughts and polar night (Wolfe 1985). Further, macrofossils indicate that the leaves of polar trees were larger than the leaves of temperate trees (Wolfe 1985). With its large leaves, polar trees adapted to the long growing season and the low incidence angle of the sun.

The special characteristics of polar forest require a new PFT in JSBACH. So far, JSBACH considers two kinds of extra-tropical trees: summergreen and evergreen trees. I recommend separating the extra-tropical trees into polar trees and temperate trees. Polar trees have a combined raingreen and 'lightgreen' phenology and large leaves (high leaf area index (LAI)). For temperate forest, a raingreen and evergreen phenology is considered. The leaves have the same size as present-day temperate forest. In the warm early Eocene climate, temperature remains mild during the whole year even in the high latitudes. Hence, trees with a summergreen phenology become superfluous.

Paratropical rainforest grew in large parts of the mid latitudes (Wolfe 1985). Paratropical forest was a mixture of tropical trees and extra-tropical trees. JSBACH clearly separates tropical trees and extra-tropical trees by distinct bioclimatic limits for each PFT. This separation makes the representation of paratropical forest impossible. Hence, a PFT that reflects paratropical trees is needed.

Table 5.3: Ideas for a new set PFTs

PFTs	Phenology	Characteristics
Polar trees	raingreen/lightgreen	large leaves
Temperate deciduous trees	raingreen	
Temperate evergreen trees	evergreen	
Paratropical trees	raingreen	tropical and temperate elements
Evergreen tropical trees	raingreen	
Deciduous tropical trees	raingreen	
Fern, forbs, herbs	raingreen	lower fuel content than grasses
Shrubs	raingreen	

I stated above that frequent fires in the early Eocene climate might have led to fire tolerant trees. JSBACH, however, does not distinguish between fire-intolerant and fire-tolerant trees. With an increasing fire frequency, however, I need to consider that the sensitivity of trees to fire might change.

The evaluation of the simulated vegetation cover reveals that the simulated extent of tropical forest is smaller than reconstructions suggest. I relate the limited poleward extent of tropical forest to a cold bias in the simulated mid latitudes. In turn, I assume that the representation of tropical trees in JSBACH fits the early Eocene tropical trees. Hence, I recommend staying with the PFTs for tropical trees.

Grasses

Grasses are redundant because they were rare during the early Eocene. Today, grasses grow beside trees and spread first after disturbances. To fill the ecological gap that evolves when excluding grasses, a PFT representing fern, herbs, and forbs could be implemented. Herbs and forbs have a mean diversity of 2.9 % in the flora fossil assemblages by Utescher and Mosbrugger (2007). Ferns have a considerable mean diversity of 7.2 %. The characteristic traits of herbs, forbs, and fern relative to grass need to be investigated in further detail. Concerning fire, herbs, forbs, and ferns could be less sensitive to fires or could have a lower fuel content than the present-day grasses. Based on this assumption, the fire frequency would be reduced and the simulated forest cover could be increased in the mid to high latitudes leading to a better agreement with vegetation reconstructions.

Physiology

The high atmospheric CO₂ concentration in the early Eocene simulation increases the NPP of plant and increases the water-use efficiency. The Eocene plant taxa, however, might have been adapted to the high atmospheric CO₂ environment. Hence, the physiology of early Eocene plants might have differed from the physiology of present-day plants. So far, I neglect differences in the plant's physiology. This issue should be addressed in future studies.

5.5 Conclusion

In this chapter, I evaluate the early Eocene vegetation cover simulated with MPI-ESM by comparing the simulated vegetation cover to vegetation reconstructions. The evaluation reveals that MPI-ESM neither reproduces the general vegetation distribution nor represent the plant taxa which prevailed during the early Eocene. I identify three reasons for the discrepancies. Firstly, a cold bias in the simulated early Eocene climate leads to a smaller poleward extent of tropical forest in my simulation than flora fossils suggest. Secondly, MPI-ESM fails to simulate the dense forest in the mid to high latitudes that vegetation reconstructions suggest. Frequent fires prohibit a dense forest in this region. Thirdly, the PFTs in MPI-ESM fail to represent the early Eocene plant taxa.

I assume that the discrepancy between the simulated and the reconstructed vegetation cover causes biases in the simulated early Eocene climate. Hence, we need to improve the representation of the early Eocene vegetation cover and plant species. I assume that the dense forest in the mid to high latitudes can be achieved by using a more complex fire model and excluding grasses. Further, I present ideas to develop PFTs that represent early Eocene plant taxa. In general, I recommend implementing more arboreal PFTs because trees dominated the early Eocene vegetation cover and had a high diversity. In this context, polar trees that shed their leaves due to polar night and dry winters should be considered. Further, paratropical trees that have tropical and temperate elements should be implemented. Other PFTs should be excluded such as summergreen extra-tropical trees, summergreen shrubs, and grasses.

Chapter 6

Summary and Conclusions

In this thesis, I compare the interaction of the vegetation and the atmosphere in the warm, nearly ice-free early Eocene climate and in the interglacial pre-industrial climate. The focus lies on three aspects: the impact of vegetation on climate, the stability of the vegetation-atmosphere system, and the representation of the early Eocene plant species in the MPI-ESM.

To estimate the impact of vegetation on the early Eocene climate and on the pre-industrial climate, I simulate both climates with a dense forest and with a bare soil on all continents. Presumably, the impact of vegetation on climate depends on the soil albedo. Hence, each of the simulations runs two times: All soils either have a similar albedo as vegetation or a much higher albedo than vegetation. With a low soil albedo, vegetation mainly affects the hydrological cycle. With a high soil albedo, vegetation affects the hydrological cycle and the surface radiation balance. In the second part of the thesis, the simulations continue with an interactive vegetation cover, i.e. the vegetation cover expands and shrinks depending on climate. For the early Eocene climate and the pre-industrial climate, I analyse whether starting the simulation from a forest world leads to a different vegetation-atmosphere state than starting the simulation from a desert world. Based on these simulations, I approach the three key questions raised in the introduction (Chapter 1). The following summary provides answers to the key questions.

Summary

1. Does the impact of vegetation on climate depend on the climate state?

I separate the impact of forest on climate into the radiative forcing by forest and the resulting climate feedbacks. The radiative forcing by forest depends on the assumed soil albedo. For each soil albedo, the radiative forcing is of similar strength in the early Eocene climate as in the pre-industrial climate. When the albedo of soil is similar to the albedo of forest, forest induces a negative radiative forcing by increasing the cloud cover. When the albedo of soil is higher than the albedo of forest, forest causes a positive radiative forcing by reducing the surface albedo.

The radiative forcing by forest induces climate feedbacks. Those are similar for both soil albedo values but they differ in the early Eocene climate and in the pre-industrial

climate. In the pre-industrial climate, the water-vapour/lapse-rate feedback amplifies the temperature change on a global scale. The ice-albedo feedback amplifies the temperature change by forest in the high latitudes. In the early Eocene climate, the water-vapour/lapse-rate feedback is stronger than in the pre-industrial climate. Consequently, the global temperature change by forest is stronger in the early Eocene climate. The ice-albedo feedback is weak in the nearly ice-free early Eocene climate leading to a zonally uniform temperature change by forest.

In the sum, the results illustrate that forest influences the early Eocene climate differently than the pre-industrial climate because forest induces different feedbacks in both climates. Climate-specific feedbacks lead to a different temperature change by forest in both climates in terms of spatial characteristics and global magnitude.

2. Does the stability of the vegetation-atmosphere system differ in the early Eocene climate and in the pre-industrial climate?

In both climates, multiple vegetation-atmosphere states exist when soil and vegetation have a similar albedo. In the pre-industrial climate, more vegetation remains in the Sahel when the simulation starts from a forest world instead of a desert world. At the beginning of the simulations, forest enhances water recycling and increases precipitation in the Sahel. Starting from a stronger precipitation, more vegetation remains in the Sahel in the simulation that starts from a forest world. The remaining vegetation, in turn, maintains a high precipitation rate.

In the early Eocene climate, a desert establishes in Central Asia. This Asian desert is smaller when the simulation starts from a forest world instead of a desert world. Like in the pre-industrial Sahel, the hydrological feedback between vegetation and precipitation causes the multiple vegetation states. Beside enhancing water recycling, vegetation in Central Asia increases the Asian monsoon. The resulting shift in the general atmospheric circulation leads to two different global climate states with a small Asian desert and with a large Asian desert. The two different climate states lead to further multiple vegetation states in subtropical semi-deserts on the American continents. The reasons for the global instability in the vegetation-atmosphere system are the specific distribution of the continents and the early Eocene climate state. Both lead to a desert in Central Asia which is bistable and has a steering role in the early Eocene climate.

3. What limitations arise in the simulated early Eocene vegetation cover from using present-day Plant Functional Types (PFTs)?

The PFTs in JSBACH fail to represent the plant taxa that characterised the early Eocene vegetation cover. For instance, none of the PFTs reflects polar trees or paratropical trees. Polar trees shed their leaves due to polar night and seasonal drought.

Such phenology is absent in JSBACH. Paratropical trees combined tropical as well as temperate elements. JSBACH clearly distinguishes between tropical trees and extra-tropical trees. In addition to missing PFTs, JSBACH includes superfluous PFTs such as grasses and tundra shrubs. The lacking representation of early Eocene plant taxa leads to discrepancies between the simulated and the reconstructed vegetation cover in the mid to high latitudes.

Further discrepancies arise from a cold bias in the simulated early Eocene climate. The cold bias leads to a smaller poleward extent of tropical forest than flora fossils indicate. Moreover, JSBACH simulates frequent fires in the mid to high latitudes leading to an open forest in these regions. Fossils, however, indicate a dense forest. This result indicates that either fires are overestimated by the model or the assumed vulnerability of trees to fires is too high.

Research perspective

Depending on the assumed soil albedo, vegetation either warms or cools the early Eocene climate. This result emphasises that a realistic soil albedo map is essential to accurately estimate the impact of vegetation on past climates. A soil albedo map for past periods can be reconstructed based on palaeosols and sedimentary records. Those reconstructions, however, are regionally limited. Alternatively, the soil albedo can be simulated by using a dynamic soil albedo module. Vamborg et al. (2011) developed such a module which derives the soil albedo from soil organic matter. In another approach, Stärz et al. (submitted) calculate the soil albedo from the vegetation cover. Future studies should utilise a combination of both, dynamic soil albedo modules and soil albedo reconstructions, to estimate the impact of vegetation on past climates.

Regarding the discrepancy between the PFTs in earth system models and early Eocene plant taxa, further research is needed. The physical appearance of early Eocene plants, their bioclimatic limits, their response to high atmospheric CO₂, and their vulnerability to disturbances need to be characterised and implemented in earth system models.

Conclusions and implications

This thesis underlines that the terrestrial biosphere is closely connected to the other components of the climate system via feedbacks. The strength of these feedbacks differs in the early Eocene climate and in the pre-industrial climate. On global and regional scale, climate-dependent feedbacks lead to a different impact of forest on the early Eocene climate than on the pre-industrial climate. I assume that this result is also valid for any other warm nearly ice-free climates of the past. Warm and ice-free climates dominated the last 570 Million years (Frakes 1979). Hence, vegetation likely affects present-day climate differently than it has affected most climates in the last 570 Million years.

Presumably, feedbacks are also climate-dependent for any other radiative forcing than forest. This result is important when extreme warming events of the past are investigated to learn about future climate change. For instance, the Paleocene-Eocene Thermal Maximum (PETM) is often seen an analogue for future climate change because temperature rose by 5°C to 6°C in 10.000 years. The PETM started from a warm climate which was almost as warm as the early Eocene climate. This study suggests that feedbacks were different in such a warm climate than today. One needs to consider climate-dependent feedbacks when learning from past climates for the future.

In addition to a different impact of forest on the early Eocene climate and on the pre-industrial climate, the stability of the vegetation-atmosphere system differs in both climates. While two vegetation-atmosphere states coexist in Northern Africa in the pre-industrial climate, the global vegetation-atmosphere system is bistable in the early Eocene climate. The spatial extent of the instability in the vegetation-atmosphere system differs because the distribution of continents and the atmospheric state are specific in the early Eocene climate and in the pre-industrial climate. The distribution of continents and the atmospheric state constantly change on geological time scales. Hence, the stability of the vegetation-atmosphere system is likely unique in each present, past, and future climate.

Acknowledgements

First and foremost, I thank my supervisor, Martin Claussen, for supporting me with his knowledge and experience. Further, I thank him for giving me the opportunity to conduct this thesis in the fascinating field of Palaeoclimatology.

The regular panel meetings provided me with new ideas and motivation. Therefore, I thank Victor Brovkin, Tajana Ilyina, and Björn Stevens for the fruitful discussions and the helpful comments.

The IMPRS allowed me to graduate in an interdisciplinary and international environment which I appreciated from the scientific and personal point of view. I like to thank Antje Weitz, Wiebke Böhm, and Cornelia Kampmann for running this school.

I further thank my colleges and friends at MPI. Veronika Gayler, Helmuth Haak, and Irina Fast helped me a lot with their technical support. By proofreading, David Bröhan, Gernot Geppert, Thomas Kleinen, and Thomas Raddatz contributed to improve this thesis. Jessica, Irina, Gernot, Mathias, Basti, Malte, Thomas, Thomas, and Lena gave me a pleasant time at MPI.

I thank Thomas Hickler and Volker Mosbrugger for sharing their knowledge about vegetation species in the past. Further, I acknowledge the GINKGO network which initiated a discussion about Palaeovegetation between the data community and the modelling community. This discussion was extremely interesting for me and help me to develop my thesis.

I thank Torsten Utescher for providing me with the data set of vegetation reconstructions. I also thank Matthew Huber for sending me the data of terrestrial temperature reconstructions.

Finally, I warmly thank my family for their backing in every situation. I thank David for being at my side.

Acronyms

- CLAMP** Climate-Leaf Analysis Multivariate Program
- CO₂** carbon dioxide
- DGVM** Dynamic Global Vegetation Model
- EECO** Early Eocene Climatic Optimum
- ENSO** El Niño-Southern Oscillation
- ESM** Earth System Model
- GCM** general circulation model
- GPP** gross primary production
- LAI** leaf area index
- LGM** Last Glacial Maximum
- LMA** Leaf Margin Analysis
- MPI-ESM** Max Planck Institute for Meteorology Earth System Model
- MPIOM** Max Planck Institute Ocean Model
- NLR** Nearest Living Relative
- NPP** net primary production
- PETM** Paleocene-Eocene Thermal Maximum
- PFT** Plant Functional Type
- SST** sea surface temperature
- SST** Sea Surface Temperature
- ToA** top of the atmosphere

List of Figures

1.1	Qualitative temperature evolution during the Eocene based on deep-sea temperature estimates adapted from Zachos et al. (2001). The x-axis shows the age since today in Million years (Ma). In this thesis, I consider the early Eocene (gray bar) which is the time between the end of the Paleocene-Eocene Thermal Maximum and the Early Eocene Climatic Optimum.	3
2.1	Orography map (a) and bathymetry map (b) prescribed in the early Eocene simulation. The maps are derived from the maps by Bice and Marotzke (2001).	13
2.2	Annual mean 2-m temperature in the early Eocene simulation in shaded colours. Stars show reconstructed annual mean Sea Surface Temperature (SST) derived from the marine proxy data compilation by Lunt et al. (2012). The data compilation includes temperature estimate based on $\delta^{18}O$, Mg/Ca, and TEX ₈₆ estimates. The numbers 1 and 2 mark SST reconstructions by Sluijs et al. (2006) and Bijl (2009), respectively. Cycles refer to terrestrial annual mean temperature estimates provided by Huber and Caballero (2011). Reconstructions are derived from macrofloral and palynoflora assemblage data and from teeth, hydrogen isotopes, and oxygen isotopes.	15
2.3	Zonal mean surface temperature averaged over 30 years in the early Eocene climate (red line) and in the pre-industrial climate (blue line).	17
2.4	Annual-mean 2-m temperature in the early Eocene climate (a) and in the pre-industrial climate (b). In hatched regions, snow cover and sea-ice cover exceeds 0.3 at the end of the respective hemispheric winter (March in the northern hemisphere and September in the southern hemisphere).	18
2.5	Annual mean precipitation in the early Eocene climate (a) and in the pre-industrial climate (b).	18
3.1	Vegetation cover in the forest world for pre-industrial (a) and early Eocene boundary conditions (b). Extra-tropical trees and tropical trees differ concerning their leaf area index and roughness length.	23
3.2	Evolution of radiative flux at the top of the atmosphere with temperature changes in the early Eocene bright desert world. At the beginning of the simulation, savannah-like vegetation is replaced by bare soil with an albedo of 0.4. Black points refer to the first 150 simulated years. Gray points reflect the remaining 250 years. The black line is the regression line fitted to the first 150 years.	24

3.3	The evolution of differences in the top of the atmosphere (ToA) radiative flux between the forest world and the bright desert worlds with corresponding differences in near-surface temperature. Global annual-mean values are considered. Red points relate to the early Eocene climate and blue points refer to the pre-industrial climate. The first 150 years are shown as dark large points. The last 250 years are displayed as bright small points. The regression and the correlation coefficient, r , consider the first 150 years. The shaded areas refer to the 95% confidence interval for the regression lines.	29
3.4	Net radiative forcing and its single components for the comparison of the forest world to the bright desert world (a) and for the comparison of the forest world to the dark desert world (b). The hatched and the plain bars show the radiative forcings for the pre-industrial climate and the early Eocene climate, respectively. The error bars refer to the 95% confidence interval.	29
3.5	Difference in cloud cover and planetary albedo between the forest and the bright desert world averaged over the first year of the simulations. a) and c) show the differences for the early Eocene climate and b) and d) for the pre-industrial climate.	30
3.6	Net feedback parameter and its single components for the comparison of the forest world to the bright desert world (a) and for the comparison of the forest world to the dark desert world (b). The lapse-rate and water-vapour feedback, λ_{WV+LR} , is derived by subtracting the Planck feedback parameter from the long-wave clear-sky feedback parameter. The hatched and the plain bars show the feedback factors for the pre-industrial climate and the early Eocene climate, respectively. The error bars refer to the 95% confidence interval.	31
3.7	Zonal mean temperature in the dark desert world (orange line), the forest world (green line), and the bright desert world (blue line). The graphs show the average over the last 30 years of each early Eocene simulation (a) and of each pre-industrial simulation (b).	31
3.8	Evolution of the difference in ToA short-wave cloud radiative flux, R_{SWcl} , with differences in near-surface temperature between the forest world and the bright desert world. The evolution of R_{SWcl} is separated in the evolution above the land (a) and above the ocean (b). Global annual-mean values are considered. Red points relate to the early Eocene climate. Blue points refer to the pre-industrial climate. The first 150 years are shown as dark large points, the last 250 years are shown as bright small points. The regression and the correlation coefficient, r , consider the first 150 years. The shaded areas refer to the 95% confidence interval for the regression lines.	32
3.9	The evolution of differences in the ToA radiative flux between the forest world and the dark desert worlds with corresponding temperature differences. Global annual mean values are considered. The red points relate to the early Eocene climate and the blue points to the pre-industrial climate. The first 150 years are shown as dark large points, the last 250 years are shown as bright small points. The regression and the correlation coefficient, r , consider the first 150 years. The shaded areas refer to the 95% confidence interval for the regression lines.	33

-
- 4.1 Feedback mechanisms that are suggested to cause multiple stable vegetation-atmosphere states in the Sahel (a), in the Amazon (b), and in the boreal region (c). Signs indicate the relationship between two variables connected with the respective arrow. Assuming the arrow connects X and Y, a positive sign indicates that an increase in X causes an increase in Y. A negative sign implies that an increase in X results in a decrease in Y. 40
- 4.2 Idealised development of the vegetation cover in the FB_E simulation and in the DB_E simulation. Starting from a forest world and from a desert world, vegetation cover evolves according to climate. I investigate whether the vegetation cover reaches the same state in both simulations. Therefore, I analyse the last 30 years for the simulations (final state) and the last 30 years for the forest world and desert world simulations (initial state). 42
- 4.3 Desert cover in the DD_E simulation. The average over the last 30 years of the simulation is shown. Green indicates a minimum desert cover. Bluish colours refer to open vegetation. Yellow colours mark desert regions. 43
- 4.4 Dark soil: Differences in vegetation cover between the simulations that start from a forest world and from a desert world. Shown are differences for the early Eocene climate ($FD_E - DD_E$) (a) and for the pre-industrial climate ($FD_P - DD_P$) (b). Mapped differences are significant on a 95% confidence interval. Woody types include all trees and shrubs. Grass types refer to C_4 grass and to C_3 grass. Green colours indicate a higher cover fraction in the FD than in the DD simulation. Purple colours refer to a smaller cover fraction in the FD simulation. Black contour lines mark regions which are analysed in more detail in Figure 4.5 and Figure 4.9. 44
- 4.5 Time series of desert cover and precipitation in selected regions in Central Asia (a), South America (b), North America (c), and Africa (d) in the FD_E simulation (green line) and in the DD_E simulation (orange line). The regions are marked in Figure 4.4. Both time series show five-year mean values. . . . 45
- 4.6 Annual cycle of precipitation in early Eocene Central Asia. The respective region is marked in Figure 4.4. Lines refer to the FD_E simulation (green) and the DD_E simulation (orange). The average over the last 30 years of each simulation is considered. 46
- 4.7 Velocity potential at 200 hPa in the FD_E simulation (a) and in the DD_E simulation (b). The 30-year average for the Asian monsoon season (July, August, and September) is shown. Brownish colours refer to a positive velocity potential. Air converges in regions of positive velocity potential and air subsides below. Greenish colours refer to a negative velocity potential. Air diverges in regions of negative velocity potential and air rises below. 47
- 4.8 Precipitation differences (a) and temperature differences (b) between the FD_E simulation and the DD_E simulation. The average over the last 30 years of the respective simulation is considered. Depicted differences are significant on a 95% confidence interval. 48
- 4.9 Time series of desert cover and precipitation in pre-industrial Sahel in the FD_P simulation (green line) and in the DD_P simulation (orange line). The Sahel region is marked in Figure 4.4. Both time series show five-year mean values. 49

4.10	Annual cycle of precipitation in the pre-industrial Sahel. The respective region is marked in Figure 4.4. The lines refer to the end of the FD_P simulation (green) and in the DD_P simulation (orange) simulation. 30-year average values are shown.	49
4.11	Precipitation differences (a) and temperature differences (b) between the end of the FD_P simulation and the end of the DD_P simulation. Depicted differences are significant on a 95% confidence interval.	50
4.12	Velocity potential at 200 hPa in the FD_P simulation (a) and in the DD_P simulation (b). The 30-year average for the African monsoon season (July, August, and September) is shown. Brownish colours refer to a positive velocity potential. Air converges in regions of positive velocity potential and air subsides below. Greenish colours refer to a negative velocity potential. Air diverges in regions of negative velocity potential and air rises below.	51
4.13	Time series of desert cover and precipitation in early Eocene Central Asia in the FB_E simulation (green line) and in the DB_E simulation (orange line). The early Eocene Central Asia is marked in Figure 4.4. Both time series show five-year mean values.	51
4.14	Bright soil: Differences in vegetation cover between the simulations that start from a forest world and from a desert world. Shown are differences in vegetation cover for the early Eocene climate ($FB_E - DB_E$) (a) and for the pre-industrial climate ($FB_P - DB_P$) (b). Mapped differences are significant on a 95% confidence interval. Woody types include all trees and shrubs. Grass types refer to C_4 grass and to C_3 grass. Green colours indicate a higher cover fraction in the FD simulation than in the DD simulation. Purple colours indicate a smaller cover fraction in the FD simulation. Black contour lines mark regions which are analysed in more detail in Figure 4.13 and Figure 4.18.	52
4.15	Net radiation at the top of the atmosphere in the initial state (a) and in the final state (b) of the FB_E simulation. The initial state refers to the average over the last 30 years of the early Eocene forest world simulation. The final state reflects the average over the last 30 years of the FB_E simulation. Yellow colours and reddish colours indicate a positive net radiation at the top of the atmosphere. The atmosphere gains energy in these regions. Bluish colours indicate a loss of energy. During the simulation, net radiation mainly changes in Central Asia.	53
4.16	Meridional circulation averaged from 58°E to 90°E in the initial state (a) and in the final state (b) of the FB_E simulation. Shown is the seasonal mean over July, August, and September. The initial state and the final state refer to the average over the last 30 years of the forest world simulation and of the FB_E simulation. The location of the Asian desert is marked by the grey bar at 1000 hPa.	54
4.17	Moisture convergence at the surface (shading) and wind at 10 meters above the surface (arrows) in the initial state (a) and in the final state (b) of the FB_E simulation. Shown is the seasonal mean for July, August, and September. The initial state and the final state refer to the average over the last 30 years of the forest world simulation and of the FB_E simulation.	55

4.18	Time series of desert cover and precipitation in pre-industrial Sahel (a) and time series of desert cover and temperature at 2 m above the surface in Siberia (b) in the FB_P simulation (green line) and in the DB_P simulation (orange line). The Sahel region is marked in Figure 4.14. All time series show five-year mean values.	56
4.19	Net radiation at the top of the atmosphere in the initial state (a) and in the final state (b) of the FB_P simulation. The initial state and the final state refer to the average over the last 30 years of the forest world simulation and of the FB_P simulation. Yellow colours and reddish colours refer to a positive net radiation at the top of the atmosphere. The atmosphere gains energy in these regions. Bluish colours indicate a loss of energy. During the FB_P simulation, net ToA radiation changes strongly above the Arabian desert and Northern Africa.	57
4.20	Meridional circulation averaged from $10^\circ W$ to $40^\circ E$ in the initial state (a) and in the final state (b) of the FB_P simulation. Shown is the seasonal mean over July, August, and September. The initial state and the final state refer to the average over the last 30 years of the forest world simulation and of the FB_P simulation. The location of the Asian desert is marked by a grey bar at the 1000 hPa level.	58
4.21	Moisture convergence at the surface (shading) and wind at 10 meters above the surface (arrows) in the initial state (a) and in the final state (b) of the FB_P simulation. Shown is the seasonal mean over July, August, and September. The initial state and the final state refer to the average over the last 30 years of the forest world simulation and of the FB_P simulation.	59
5.1	Simulated early Eocene vegetation cover in the FD_E simulation in shading. Dots indicate sites where the flora collection by Utescher and Mosbrugger (2007) suggests the existence of the respective PFTs. The allocation of reconstructed PFTs to simulated PFTs is listed in Table 5.2.	64
5.2	Frost criterion and lowest multi-year monthly mean temperature threshold. The simulated early Eocene climate allows tropical trees in the green shaded regions according to the respective criteria. The frost criteria means that the 6-hourly temperature never drops below $0^\circ C$. The lowest multi-year monthly mean temperature threshold is $15.5^\circ C$	65

List of Tables

2.1	List of Plant Functional Types (PFTs) defined in the land surface scheme JSBACH and their classification in the dynamic vegetation module DYNVEG.	11
2.2	Boundary conditions in the early Eocene climate simulation and in the pre-industrial climate simulation which is used for comparison. The soil flag expresses the heat capacity and diffusivity of soils.	14
2.3	Comparison of the simulated pre-industrial climate and the early Eocene climate in terms of the global annual mean values. For the snow cover, the average over land is considered. For the sea-ice cover, the average over the ocean is considered. The meridional temperature gradient is defined in Equation 2.1.	16
3.1	Simulations performed with boundary conditions for the early Eocene climate and the pre-industrial climate. The listed vegetation cover is prescribed on all ice-free continents. The values for the surface albedo refers to the land surface. In the desert world, the soil albedo equals the surface albedo. In the forest world, trees cover the soil completely and the albedo of the forest determines the surface albedo.	22
3.2	Mechanisms that cause the respective radiation forcings and feedbacks in the simulations.	26
3.3	Net radiative forcing by afforesting a bright desert world in the early Eocene climate and the pre-industrial climate. Further, the net feedback parameter and the equilibrium temperature change are listed. The values are derived from the comparison of the respective forest world with the respective bright desert world. The 95% confidence interval is given. The transient temperature change refers to the temperature difference at the end of both simulations.	28
3.4	Net radiative forcing by afforesting a dark desert world in the early Eocene climate and in the pre-industrial climate. Further, the net feedback parameter and the equilibrium temperature change are listed. The values are derived from the comparison of the respective forest world with the respective dark desert world. The 95% confidence interval is given. The transient temperature change refers to the temperature difference at the end of both simulations.	33
4.1	Simulations included in the experiment. The same set of simulations is performed for the early Eocene climate and for the pre-industrial climate. Detailed information about the different boundary conditions are given in Chapter 2. For both climates, the simulations differ concerning the initial vegetation-atmosphere state and the soil albedo. The initial vegetation-atmosphere states are the forest worlds and desert worlds introduced in Chapter 3. Soils are either bright or dark with a homogeneous soil albedo of 0.4 or 0.1, respectively.	41

4.2	Radiation at the top of the atmosphere, hydrology, surface albedo, and surface temperature in early Eocene Central Asia in the initial state and final state of the FB_E simulation and DB_E simulation. The considered region is marked in Figure 4.14. The initial state refers to the average over the last 30 years of the forest world and bright-desert world simulation (Figure 4.2). The final state refers to the average over the last 30 years of the respective simulation. . . .	53
4.3	Radiation at the top of the atmosphere, hydrology, surface albedo, and surface temperature in the pre-industrial Sahel in the initial state and final state of the FB_P simulation and DB_P simulation. The considered region is marked in Figure 4.14. The initial state refers to the average over the last 30 years of the forest world and bright-desert world simulation (Figure 4.2). The final state refers to the average over the last 30 years of the respective simulation. . . .	56
5.1	The bioclimatic limits and the phenology of the PFTs in JSBACH. The minimum and the maximum of the lowest multi-year monthly-mean temperature are reflected by TC_{\min} and TC_{\max} , respectively. TW_{\max} is the maximum of the highest multi-year monthly-mean temperature. GDD_{\min} is the minimum of growing degree days. All these parameters are given in $^{\circ}C$. If no value is given, no limit exists. JSBACH considers four types of phenology. Evergreen vegetation does not shed its leaves. Summergreen and raingreen PFTs shed their leaves when climate gets too cold and too dry, respectively. Grasses have their own phenology.	62
5.2	Arboreal PFTs in JSBACH and their allocation to the arboreal PFTs by Utescher and Mosbrugger (2007).	63
5.3	Ideas for a new set PFTs	68

References

- Andrews, T., Gregory, J., Webb, M., and Taylor, K. (2012). Forcing, feedbacks and climate sensitivity in CMIP5 coupled atmosphere-ocean climate models. *Geophysical research letters*, 39.
- Arakawa, A. and Lamb, V. R. (1977). Computational design of the basic dynamical processes of the UCLA general circulation model. *Methods Comput. Phys.*, 17:173–265.
- Bala, G., Caldeira, K., Wickett, M., Phillips, T. J., and Lobell, D. B. (2007). Combined climate and carbon-cycle effects of large-scale deforestation. *Proceedings of the National Academy of Sciences of the United States of America*, 104(23):6550–6555.
- Banacos, P. C. and Schultz, D. M. (2005). The use of moisture flux convergence in forecasting convective initiation: Historical and operational perspectives. *Forecaster’s Forum*.
- Barron, E. J. (1987). Eocene equator-to-pole surface ocean temperatures: A significant climate problem? *Paleoceanography*, 2:729–739.
- Bathiany, S., Claussen, M., Brovkin, V., Raddatz, T., and Gayler, V. (2010). Combined biogeophysical and biogeochemical effects of large-scale forest cover changes in the MPI Earth System Model. *Biogeoscience*, 7:1383–1399.
- Berling, D. and Royer, D. (2011). Convergent Cenozoic CO₂ history. *Nature geoscience*, 4(7):418–420.
- Berg, L. (2008). *Introductory Botany: Plants, People, and Environment*. Thomson Brooks/Cole.
- Betts, A. K. and Ball, J. H. (1997). Albedo over the boreal forest. *Journal of Geophysical Research: Atmospheres*, 102(D24):28901–28909.
- Bice, K. L. and Marotzke, J. (2001). Numerical evidence against reversed thermohaline circulation in the warm Paleocene/Eocene ocean. *Journal of geophysical research*, 106(C6):11529–11542.
- Bijl, P. K. (2009). Early palaeogene temperature evolution of the southwest pacific ocean. *Nature*, 461:776–779.
- Bonan, G. B. (1992). Effects of boreal forest vegetation on global climate. *Nature*, 359:716–718.
- Bonan, G. B. (2008). Forests and Climate Change: Forcings, Feedbacks, and the Climate Benefits of Forests. *Science*, 320:1444 – 1449.
- Bowman, V., Francis, J., and Riding, J. (2013). Late Cretaceous winter sea ice in Antarctica? *Geology*, 41(12):1227–1230.

- Brovkin, Ganopolski, A., Claussen, M., Kubatzki, C., and Petoukhov, V. (1999). Modelling climate response to historical land cover change. *Global ecology and biogeography letters*, 8(6):509–517.
- Brovkin, Levis, S., Loutre, M., Crucifix, M., and Claussen, M. (2003). Stability analysis of the climate-vegetation system in the northern high latitudes. *Climatic change*, 57(1-2):119–138.
- Brovkin, V., Claussen, M., Petoukhov, V., and Ganopolski, A. (1998). On the stability of the atmosphere-vegetation system in the sahara/sahel region. *Journal of Geophysical Research: Atmospheres*, 103(D24):31613–31624.
- Brovkin, V., Raddatz, T., and Reick, C. H. (2009). Global biogeophysical interactions between forest and climate. *Geophysical Research Letters*, 36.
- Cerling, T., Wang, Y., and Quade, J. (1993). Expansion of C4 ecosystems as an indicator of global ecological change in the late Miocene. *Nature*, 361(6410):344–345.
- Charney, J., Quirk, W., Chow, S., and Kornfield, J. (1977). Comparative-study of effects of albedo change on drought in semi-arid regions. *Journal of the Atmospheric Sciences*, 34(9):1366–1385.
- Charney, J. G. (1975). Dynamics of deserts and drought in Sahel. *Quarterly Journal of the Royal Meteorology Society*, 101:193–202.
- Claussen, M. (1997). Modeling bio-geophysical feedback in the african and indian monsoon region. *Climate dynamics*, 13(4):247–257.
- Claussen, M. (1998). On multiple solutions of the atmosphere-vegetation system in present-day climate. *Global change biology*, 4(5):549–559.
- Claussen, M., Brovkin, V., and Ganopolski, A. (2001). Biogeophysical versus biogeochemical feedbacks of large-scale land cover change. *Geophysical Research Letters*, 28:1011–1014.
- Dekker, S. C., de Boer, H. J., Brovkin, V., Fraedrich, K., and Wassen, M. J. (2010). Biogeophysical feedbacks trigger shifts in the modelled vegetation-atmosphere system at multiple scales. *Biogeosciences*, 7(4):1237–1245.
- Devaraju, N., Cao, L., Bala, G., Caldeira, K., and Nemani, R. (2011). A model investigation of vegetation-atmosphere interactions on a millennial timescale. *Biogeosciences*, 8(12):3677–3686.
- Donnadieu, Y., Godd eris, Y., and Bouttes, N. (2009). Exploring the climatic impact of the continental vegetation on the Mesozoic atmospheric CO₂ and climate history. *Climate of the Past*, 5(1):85–96.
- Foley, J. A., Levis, S., Prentice, I. C., Pollard, D., and Thompson, S. L. (1998). Coupling dynamic models of climate and vegetation. *Global Change Biology*, 4:561–579.
- Fouquart, Y. and Bonnel, B. (1980). Computations of solar heating of the earth’s atmosphere—a new parameterization. *Beitr. Phy. Atmos.*, 53:35–62.
- Fraedrich, K., Jansen, H., Kirk, E., and Lunkeit, F. (2005). The planet simulator: Green planet and desert world. *Meteorologische Zeitschrift*, 14(3):305–314.

- Fraedrich, K. and Kleidon, A. (1999). A green planet versus a desert world: Estimating the effect of vegetation extremes on the atmosphere. *American Meteorological Society*, 12:2156–3163.
- Frakes, L. A. (1979). *Climates Throughout Geologic Time*. Elsevier.
- Francois, L., Utescher, T., Favre, E., and Warnant, P. (2011). Modelling Late Miocene vegetation in Europe: Results of the CARAIB model and comparison with palaeovegetation data. *Palaeogeography, Palaeoclimatology, Palaeoecology*, 304(3-4):359–378.
- Gent, P. R., Willebrand, J., McDougall, T., and McWilliams, J. C. (1995). Parameterizing eddy-induced tracer transports in ocean circulation models. *J. Phys. Oceanogr.*, 25:463–474.
- Gersonde, R., Crosta, X., Abelman, A., and Armand, L. (2005). Sea-surface temperature and sea ice distribution of the southern ocean at the epilog last glacial maximum - a circum-antarctic view based on siliceous microfossil records. *Quaternary Science Reviews*, 24(7-9):869 – 896. Multiproxy Approach for the Reconstruction of the Glacial Ocean surface.
- Gregory, J., Ingram, W., Palmer, M., Jones, G., and Stott, P. (2004). A new method for diagnosing radiative forcing and climate sensitivity. *Geophysical research letters*, 31(3).
- Heinemann, M. (2009). *Warm and sensitive Early Eocene climate*. PhD thesis, IMPRS.
- Heinemann, M., Jungclaus, J. H., and Marotzke, J. (2009). Warm Paleocene/Eocene climate as simulated in ECHAM5/MPI-OM. *Climate of the Past*, 5:785–802.
- Hibler, W. D. (1979). A dynamic thermodynamic sea ice model. *J. Phys. Oceanogr.*, 9:815–846.
- Hönisch, B., Ridgwell, A., Schmidt, D. N., Thomas, E., Gibbs, S. J., Sluijs, A., Zeebe, R., Kump, L., Martindale, R. C., Greene, S. E., Kiessling, W., Ries, J., Zachos, J. C., Royer, D. L., Barker, S., Marchitto, T. M., Moyer, R., Pelejero, C., Ziveri, P., Foster, G. L., and Williams, B. (2012). The geological record of ocean acidification. *Science*, 335(6072):1058–1063.
- Huber, M. and Caballero, R. (2011). The early Eocene equable climate problem revisited. *Climate of the Past*, 7:603–633.
- Hutchison, J. (1982). Turtle, crocodylian, and champsosaur diversity changes in the cenozoic of the north-central region of western united states. *Palaeogeography, Palaeoclimatology, Palaeoecology*, 37(2?4):149 – 164.
- Iacono, M. J., Delamere, J. S., Mlawer, E. J., Shephard, M. W., Clough, S. A., and Collins, W. D. (2008). Radiative forcing by long-lived greenhouse gases: Calculations with the AER radiative transfer models. *J. Geophys. Res.*, 113:D13103.
- Ilyina, T., Six, K. D., Segschneider, J., Maier-Reimer, E., Li, H., and Nunez-Riboni, I. (2013). Global ocean biogeochemistry model HAMOCC: Model architecture and performance as component of the MPI-Earth System Model in different CMIP5 experimental realizations. *Journal of Advances in Modeling Earth Systems*, 5:287–315.
- Ivany, L., Lohmann, K. C., Hasiuk, F., Blake, D. B., Glass, A., Aronson, R. B., and Moody, R. M. (2008). Eocene climate record of a high southern latitude continental shelf: Seymour island, antarctica. *Geological Society of America Bulletin*, 5-6:659–678.

- Ivany, L., Simaey, S. V., Domack, E., and Samson, S. (2006). Evidence for an earliest oligocene ice sheet on the antarctic peninsula. *Geology*, 34(5):377–380.
- Janis, C. M. (1993). Tertiary mammal evolution in the context of changing climates, vegetation, and tectonic events. *Annual review of ecology and systematics*, 24:467–500.
- Jansen, E., Overpeck, J., Briffa, K., Duplessy, J.-C., Joos, F., Masson-Delmotte, V., Olago, D., Otto-Bliesner, B., Peltier, W., Rahmstorf, S., Ramesh, R., Raynaud, D., Rind, D., Solomina, O., Villalba, R., and Zhang, D. (2007). Palaeoclimate. In: *Climate Change 2007: The Physical Science Basis. Contribution of Working Group I to the Fourth Assessment Report of the Intergovernmental Panel on Climate Change. Cambridge University Press, Cambridge, United Kingdom and New York, NY, USA.*
- Jungclaus, J. (2006). Ocean circulation and tropical variability in the coupled model echam5/mpiom. *Journal of climate*, 19:3952–3972.
- Jungclaus, J. H., Fischer, N., Haak, H., Lohmann, K., Marotzke, J., Matei, D., Mikolajewicz, U., Notz, D., and von Storch, J. S. (2013). Characteristics of the ocean simulations in the Max Planck Institute Ocean Model (MPIOM) the ocean component of the MPI-Earth system model. *Journal of Advances in Modeling Earth Systems*, 5(2):422–446.
- Kubatzki, C. and Claussen, M. (1998). Simulation of the global bio-geophysical interactions during the last glacial maximum. *Climate dynamics*, 14(7-8):461–471.
- Laskar, J., Robutel, P., Joutel, F., Gastineau, M., and Correia, A. C. M. (2004). A long-term numerical solution for the insolation quantities of the earth. *Astronomy and astrophysics*, 428(1):261–285.
- Lasslop, G., Thonicke, K., and Kloster, S. (2014). SPITFIRE within the MPI Earth system model: Model development and evaluation. *J. Adv. Model. Earth Syst.*
- Lin, S.-J. and Rood, R. B. (1996). Multidimensional flux-form semi-lagrangian transport schemes. *Mon. Weather Rev.*, 124(9):2046–2070.
- Loftson, C. A., Lunt, D. J., and Francis, J. E. (2014). Investigating vegetation-climate feedbacks during the early eocene. *Climate of the past*, 10(2):419–436.
- Lorant, M., Berner, L., Goetz, S., Jin, Y., and Randerson, J. (2014). Vegetation controls on northern high latitude snow-albedo feedback: observations and CMIP5 model simulations. *Global change biology*, 20(2):594–606.
- Lorenz, E. (1968). Climatic determinism. *Meteor. Monogr.*, 8-30:1–3.
- Lunt, D., Valdes, P., Jones, T. D., Ridgwell, A., and Haywood, A. (2010). CO₂-driven ocean circulation changes as an amplifier of Paleocene-Eocene thermal maximum hydrate destabilization. *Geology*, 38(10):875–878.
- Lunt, D. J., Jones, T. D., Heinemann, M., Huber, M., LeGrande, A., Winguth, A., Loftson, C., Marotzke, J., Roberts, C. D., Tindall, J., Valdes, P., and Winguth, C. (2012). A model-data comparison for a multi-model ensemble of early Eocene atmosphere-ocean simulations: EoMIP. *Climate of the Past*, 8(5):1717–1736.
- Lüttge, U. (2008). *Physiological Ecology of Tropical Plants*. Springer.

- Markwick, P. (1994). Equability, continentality, and tertiary climate - the crocodylian perspective. *Geology*, 22(7):613–616.
- Marsland, S. J., Haak, H., Jungclaus, J. H., L. M., and Roeske, F. (2003). The max-planck-institute global ocean/sea ice model with orthogonal curvilinear coordinates. *Ocean Modelling*, 5:91–127.
- Meehl, G. (1994). Influence of the land-surface in the asian summer monsoon - external conditions versus internal feedbacks. *Journal of Climate*, 7(7):1033–1049.
- Meraner, K., Mauritsen, T., and Voigt, A. (2013). Robust increase in equilibrium climate sensitivity under global warming. *Geophysical Research Letters*, 40(22):5944–5948.
- Miller, K., Sugarman, P., Browning, J., Kominz, M., and Hernandez, J. (2003). Late Cretaceous chronology of large, rapid sea-level changes: Glacioeustasy during the greenhouse world. *Geology*, 31(7):585–588.
- Notz, D., Haumann, F. A., Haak, H., Jungclaus, J. H., and Marotzke, J. (2013). Arctic sea-ice evolution as modelled by mpi-esm. *J. Adv. Model. Earth Syst.*
- Otto-Bliesner, B. L. and Upchurch, G. R. (1997). Vegetation-induced warming of high-latitude regions during the late Cretaceous period. *Nature*, 385(6619):804–807.
- Oyama, M. and Nobre, C. (2003). A new climate-vegetation equilibrium state for tropical south america. *Geophysical research letters*, 30(23).
- Pacanowski, R. C. and Philander, S. G. H. (1981). Parameterization of vertical mixing in numerical models of tropical oceans. *J. Phys. Oceanogr.*, 11:1443–1451.
- Pearson, P., van Dongen, B., Nicholas, C., Pancost, R., and Schouten, S. (2007). Stable warm tropical climate through the eocene epoch. *Geology*, 35(3):211–214.
- Port, U., Brovkin, V., and Claussen, M. (2012). The influence of vegetation dynamics on anthropogenic climate change. *Earth System Dynamics*, 3:233–243.
- Quan, C., Liu, Y., and Utescher, T. (2012). Eocene monsoon prevalence over china: A paleobotanical perspective. *Palaeogeography, palaeoclimatology, palaeoecology*, 365:302–311.
- Reick, C. H., Raddatz, T., Brovkin, V., and Gayler, V. (2013). Representation of natural and anthropogenic land cover change in MPI-ESM. *Journal of Advances in Modeling Earth Systems*, 5(3):459–482.
- Roeckner, E., Mauritsen, T., Esch, M., and Brokopf, R. (2012). Impact of melt ponds on Arctic sea ice in past and future climate as simulated by MPI-ESM. *Journal of Advances in Modeling Earth Systems*, 4.
- Salati, E. and Vose, P. B. (1984). Amazon basin: a system in equilibrium. *Science*, 225(4658):129–38.
- Sarnthein, M., Pflaumann, U., and Weinelt, M. (2003). Past extent of sea ice in the northern north atlantic inferred from foraminiferal paleotemperature estimates. *Paleoceanography*, 18(2):1047.

- Senior, C. A. and Mitchell, J. F. B. (2000). The time-dependence of climate sensitivity. *Geophysical Research Letters*, 27(17):2685–2688.
- Sewall, J. O., Sloan, L. C., Huber, M., and Wing, S. (2000). Climate sensitivity to changes in land surface characteristics. *Global and planetary change*, 26(4):445–465.
- Sloan, L. C., Walker, J. C. G., and Moore, T. C. (1995). Possible role of oceanic heat-transport in early eocene climate. *Paleoceanography*, 10(2):347–356.
- Sluijs, A., Schouten, S., Pagani, M., Woltering, M., Brinkhuis, H., Sinninghe Damst, J. S., Dickens, G. R., Huber, M., Reichert, G., Stein, R., Matthiessen, J., Lourens, L. J., Pedenchouk, N., Backman, J., Moran, K., and the Expedition 302 Scientists (2006). Subtropical Arctic Ocean temperatures during the Palaeocene/Eocene thermal maximum. *Nature*, 441:610–613.
- Stevens, B., Giorgetta, M., Esch, M., Mauritsen, T., Crueger, T., Rast, S., Salzmann, M., Schmidt, H., Bader, J., Block, K., Brokopf, R., Fast, I., Kinne, S., Kornbluh, L., Lohmann, U., Pincus, R., Reichler, T., and Roeckner, E. (2013). Atmospheric component of the MPI-M Earth System Model: ECHAM6. *Journal of Advances in Modeling Earth Systems*, 5(2):146–172.
- Thonicke, K., Spessa, A., Prentice, I. C., Harrison, S. P., and Dong, L. (2010). The influence of vegetation, fire spread and fire behaviour on biomass burning and trace gas emissions: results from a process-based model. *Biogeosciences*, 7(6):1991–2011.
- Utescher, T. and Mosbrugger, V. (1990-2006). The palaeoflora database: <http://www.palaeoflora.de>.
- Utescher, T. and Mosbrugger, V. (2007). Eocene vegetation patterns reconstructed from plant diversity - A global perspective. *Palaeogeography Palaeoclimatology Palaeoecology*, 247(3-4):243–271.
- Valdes, P. (2012). Built for stability. *Nature*, 4:414–416.
- Vamborg, F. S. E., Brovkin, V., and Claussen, M. (2011). The effect of a dynamic background albedo scheme on Sahel/Sahara precipitation during the mid-Holocene. *Climate of the Past*.
- Wang, D., Lu, S., Han, S., Sun, X., and Quan, C. (2013). Eocene prevalence of monsoon-like climate over eastern china reflected by hydrological dynamics. *Journal of Asian earth sciences*, 62:776–787.
- Wang, G. and Eltahir, E. (2000). Biosphere-atmosphere interactions over West Africa. II: Multiple climate equilibria. *Quarterly journal of the Royal Meteorological Society*, 126(565):1261–1280.
- Warner, T. (2004). *Desert Meteorology*. Cambridge University Press.
- Webster, P. J. (1987). *Monsoons; Chapter: The elementary Monsoon*. John Wiley and Sons, Inc.
- Wilf, P. (1997). When are leaves good thermometers? A new case for leaf margin analysis. *Paleobiology*, 23(3):373–390.
- Willis, K. and McElwain, J. (2002). *The evolution of plants*. Oxford University Press.

- Wolfe, J. (1985). Distribution of major vegetation types during the Tertiary. *In: Sundquist E.T., Broecker W.S. (eds) The carbon cycle and atmospheric CO₂: natural variations Archean to present. American Geophysical Union, Washington/DC*, pages 357–375.
- Wolfe, J. (1995). Paleoclimatic estimates from tertiary leaf assemblages. *Annual Review Earth Planet Science*, 23:119–142.
- Zachos, J., Berza, J., and Wise, S. (1992). Early Oligocene ice-sheet expansion on Antarctica - Stable isotope and sedimentological evidence from Kerguelen Plateau southern Indian-Ocean. *Geology*, 20(6):569–573.
- Zachos, J., Pagani, M., Sloan, L., Thomas, E., and Billups, K. (2001). Trends, rhythms, and aberrations in global climate 65 Ma to present. *Science*, 292(5517):686–693.
- Zeng, N. and Neelin, D. J. (2000). The role of vegetation-climate interaction and interannual variability in shaping the african savanna. *Journal of Climate*, 13(15):2665–2670.
- Zeng, X. D., Shen, S. S. P., and Dickinson, R. E. (2004). Multiple equilibrium states and the abrupt transitions in a dynamical system of soil water interacting with vegetation. *Geophysical research letters*, 31(5).
- Zhang, Z., Flatoy, F., Wang, H., Bethke, I., Bentsen, M., and Guo, Z. (2012). Early eocene asian climate dominated by desert and steppe with limited monsoons. *Journal of Asian Earth Sciences*, 44(SI):24–35.

Erklärung

Hiermit erkläre ich an Eides statt, dass ich die vorliegende Dissertationsschrift selbst verfasst und keine anderen als die angegebenen Quellen und Hilfsmittel benutzt habe.

Hamburg, den 9. Dezember 2014

Hinweis / Reference

Die gesamten Veröffentlichungen in der Publikationsreihe des MPI-M
„Berichte zur Erdsystemforschung / Reports on Earth System Science“,
ISSN 1614-1199

sind über die Internetseiten des Max-Planck-Instituts für Meteorologie erhältlich:
<http://www.mpimet.mpg.de/wissenschaft/publikationen.html>

*All the publications in the series of the MPI -M
„Berichte zur Erdsystemforschung / Reports on Earth System Science“,
ISSN 1614-1199*

*are available on the website of the Max Planck Institute for Meteorology:
<http://www.mpimet.mpg.de/wissenschaft/publikationen.html>*

